Quantitative nondiagonal phase field modeling of phase transformations

Von der Fakultät für Georessourcen und Materialtechnik der
Rheinisch -Westfälischen Technischen Hochschule Aachen

zur Erlangung des akademischen Grades eines

Doktors der Ingenieurwissenschaften

genehmigte Dissertation

vorgelegt von

Kai Wang, Master of Engineering

Berichter: Herr Univ.-Prof. Dr. rer. nat. Robert Spatschek
Herr Univ.-Prof. Dr. rer. nat. Robert Svendsen

Tag der mündlichen Prüfung: 21. 10. 2021
Diese Dissertation ist auf den Internetseiten der Unversitätsbibliothek online verfügbar.

Abstract

The investigation of phase transformations is of great interest in various fields. For diffusional transitions, accurate descriptions of the diffusion processes in the parent, growing phases and at the interfaces are the prerequisite to predict the complex growth patterns. In the last decades, the phase field method has emerged as a powerful tool to investigate the moving interface problems. However, the elimination of the artificial enhanced interface effects is a long-standing unsolved problem in the phase field community. In the symmetric and the one-sided cases, the "thin-interface limit" and the anti-trapping current are proposed by Karma to reproduce the free boundary conditions. Only recently, the nondiagonal phase field model has been developed according to Onsager's relations in the two-sided case. In this work, we present the capabilities of the nondiagonal phase field model and extend the binary nondiagonal phase field model to complex alloys.

A four-fold surface energy anisotropy is incorporated in the binary nondiagonal phase field model to investigate the two-dimensional free dendrite growth of pure substances solidification. In the symmetric and the one-sided cases, the nondiagonal phase field simulation results are benchmarked with Green's function calculations. In the general two-sided case, the capabilities of nondiagonal phase field model are compared with the predictions of a generalized expression. Furthermore, the necessity of the Onsager cross-coupling term is also evidenced.

Based on Onsager's principles, the binary nondiagonal phase field model is extended to three-phase transformations by using the free energy functional. The two-dimensional nondiagonal phase field simulations are carried out not only for eutectic solidification in the one-sided case, but also for eutectoid transformation in the two-sided case. One the one hand, the obtained simulation results during eutectic solidification are benchmarked against boundary integral calculations in the one-sided case. On the other hand, simulations performed in the two-sided case during eutectoid transformations reveal that the dimensionless growth velocities of the lamellae is proportional to the ratio of diffusion coefficients. Furthermore, in both the one- and two-sided cases, the necessity of using the cross-coupling term in the nondiagonal phase field model is verified by quantitative simulations.

Since the free energy based nondiagonal model is limited for simple symmetric phase diagrams, we develop a grand potential based nondiagonal three-phase field model for complex alloy transformations. The corresponding two-dimensional phase field simulations are implemented to investigate the growth kinetics of the pearlite transformation with respect to different diffusion paths. In the one-sided case, the simulation results are compared with the Zener-Hillert model, while the simulation results in the two-sided case are proportional to the diffusivity ratios, which agrees well wit Ankit's model. Additionally, we also point out that diffusion in cementite has low influence on the growth kinetic of the pearlite transformation. When the

surface diffusion is considered, in the one-sided case, the growth velocities of the lamellae is proportional to the surface diffusion coefficient. Finally, we consider the diffusion in austenite, cementite as well as the surface diffusion and reproduce the pearlite growth for different undercoolings. The nondiagonal phase field simulation results have a convincing agreement with the experimental observations without adjustable parameters.

Kurzfassung

Die Untersuchung von Phasenumwandlungen ist auf verschiedenen Gebieten von großem Interesse. Für Diffusionsübergänge sind genaue Beschreibungen der Diffusionsprozesse in den Mutter-, Wachstumsphasen und an den Grenzflächen die Voraussetzung, um die komplexen Wachstumsmuster vorhersagen zu können. In den letzten Jahrzehnten hat sich die Phasenfeldmethode zu einem leistungsfähigen Werkzeug zur Untersuchung von Problemen mit bewegten Grenzflächen entwickelt. Die Eliminierung der künstlich verstärkten Grenzflächeneffekte ist jedoch ein seit langem ungelöstes Problem in der Phasenfeld-Community. Im symmetrischen und im einseitigen Fall werden "thin-interface limit" und Anti-Trapping-Current von Karma vorgeschlagen, um die freien Randbedingungen zu reproduzieren Erst kürzlich wurde für den zweiseitigen Fall ein nichtdiagonales Phasenfeldmodell unter Beachtung von Onsagersymmetrien entwickelt. In dieser Arbeit stellen wir die Möglichkeiten des nichtdiagonalen Phasenfeldmodells vor und erweitern das binäre nichtdiagonale Phasenfeldmodell für komplexe Legierungen.

In die binäre nichtdiagonale Phase wird eine vierfache Anisotropie der Oberflächenenergie eingebaut, um das zweidimensionale freie Dendritenwachstum der Erstarrung reiner Substanzen zu untersuchen. Im symmetrischen und einseitigen Fall werden die Ergebnisse der nichtdiagonalen Phasenfeldsimulation mit Berechnungen der Greenschen Funktion verglichen. Im allgemeinen zweiseitigen Fall werden die Fähigkeiten des nichtdiagonalen Phasenfeldmodells mit den Vorhersagen einer Generalisierung verglichen. Darüber hinaus wird auch die Notwendigkeit von Kreuzkopplungstermen nachgewiesen.

Basierend auf den Prinzipien von Onsager wird das binäre nichtdiagonale Phasenfeldmodell unter Verwendung des freien Energiefunktionals auf dreiphasige Transformationen erweitert. Die zweidimensionalen nichtdiagonalen Phasenfeldsimulationen werden nicht nur für die eutektische Erstarrung im einseitigen Fall, sondern auch für die eutektoide Umwandlung im zweiseitigen Fall durchgeführt. Einerseits werden die erhaltenen Simulationsergebnisse während der eutektischen Erstarrung mit Randintegralrechnungen im einseitigen Fall verglichen. Andererseits zeigen Simulationen im zweiseitigen Fall während eutektoider Transformationen, dass die dimensionslosen Wachstumsgeschwindigkeiten von Lamellen proportional zum Verhältnis der Diffusionskoeffizienten sind. Darüber hinaus wird sowohl im ein- als auch im zweiseitigen Fall die Notwendigkeit der Verwendung des Kreuzkopplungsterms im nichtdiagonalen Phasenfeldmodell für quantitative Simulationen verifiziert.

Da das auf freier Energie basierende Nichtdiagonalfeld für einfache symmetrische Phasendiagramme begrenzt ist, entwickeln wir ein auf dem grosskanonischen Potential basierendes nichtdiagonales Dreiphasenfeldmodell für komplexe Legierungsumwandlungen. Die entsprechenden zweidimensionalen Phasenfeldsimulationen werden durchgeführt, um die Wachstumskinetik der Perlitumwandlung in Bezug auf

verschiedene Diffusionspfade zu untersuchen. Im einseitigen Fall werden die Simulationsergebnisse mit dem Zener-Hillert-Modell verglichen, während die Simulationsergebnisse im zweiseitigen Fall einen linearen Zusammenhang zeigen. Darüber hinaus weisen wir auch darauf hin, dass die Diffusion in Zementit einen geringen Einfluss auf die Wachstumskinetik der Perlitumwandlung hat. Bei Betrachtung der Oberflächendiffusion sind im einseitigen Fall die Wachstumsgeschwindigkeiten der Lamellen proportional zum Oberflächendiffusionskoeffizienten. Schließlich betrachten wir die Diffusion in Austenit, Zementit sowie die Oberflächendiffusion und geben das Perlitwachstum für verschiedene Unterkühlungen wieder. Die Ergebnisse der nichtdiagonalen Phasenfeldsimulation stimmen mit den experimentellen Beobachtungen überzeugend überein.

Contents

List of Figures

List of Tables

Chapter 1

Introduction

The investigation of phase transformations is of great interest in materials science, chemistry and physics. Phase transformations are regarded as the physical processes, which happen in different states of matter: solid, liquid and gas as well as plasma in rare cases. They occur when the temperature, composition or structure is changed. The phase transformations can be classified in several ways. In 1933, Ehrenfest proposed a classification to distinguish the order of phase transformations by the lowest derivative with discontinuity at the transformation point. First order of phase transformations are featured by discontinuous changes in entropy, enthalpy and specific volume. Second order transitions are characterized by the absence of a latent heat of transformation and a high specific heat at the transition temperature. In 1951, Buerger introduced a classification according to the mechanism, i.e., reconstructive (diffusional) and displacive transformations. In the former transformations, the atom is transported from the parent to the product by diffusional jumps. In contrast, the atom movements in the displacive transformation are achieved by a homogeneous distortion, shuffling of lattice planes, static displacement waves or a combination of these. For diffusional transformations, such as solidification, accurate descriptions of the diffusion processes in the parent, growing phases and at the interfaces are the prerequisite to understand the complex growth patterns. Experiments are the most general method to observe the microstructure of materials and establish the mechanisms, which is often time-consuming, expensive and even poisonous. To overcome these disadvantages, the phase field method emerged as a powerful simulation method to reproduce the microstructure evolution during various materials preparation processes.

The phase-field method is established based on Ginzburg and Landau theory. Compared with the conventional front tracking method, the advantage of the phase field method is to avoid the explicit tracking of the phase boundaries. The characteristic feature of the phase field method is the diffuse interface. The thickness of the interface is usually chosen several orders of magnitude larger than the physical interface width to save computational time. However, the artificial enlargement of the interface thickness enhances the interface effects, which leads to non-quantitative results. The pioneering work of the construction of a quantitative phase field model was done by Karma and Rappel in the symmetric case by using a "thin-interface limit", where the diffusivity of the parent phase equals to the growing phase. Later, the anti-trapping current was proposed and added into the phase field model in the one-sided case, where the diffusivity of the growing phase is negligible. For the

general situation, where a finite diffusion contrast exists between the parent and growing phases, it has been a long-standing unsolved problem in the phase field community.

Recently, this problem has been solved by Boussinot and Brener by introducing a kinetic cross-coupling term between the nonconserved phase field and the conserved diffusion field based on the Onsager's relation, known as non-diagonal phase field model. This new cross-coupling term provides an additional degree of freedom to reproduce equilibrium boundary conditions for unequal diffusivities in the different bulk phases. However, the nondiagonal phase field model is restricted to binary phase transformations and the capabilities of the nondiagonal phase field for phase transformation are still unknown.

It is the aim of this thesis to present the capabilities of the nondiagonal phase field model and extend the nondiagonal phase field model for complex alloys. In **chapter 2**, the basics of thermodynamic is introduced at the beginning, including the equilibrium conditions, nonequilibrium thermodynamics (Onsager's relations) and the Gibbs-Thomson effect. Subsequently, the phase field concepts, thin-interface limit, grand potential based phase field model as well as the nondiagonal phase field model are presented. Then, some well-known phase transformations, such as dendrite growth, eutectic/eutectic transformations and pearlite transformation are explained. In the last section, the GPU acceleration technology utilized in this thesis is described.

In **chapter 3**, the nondiagonal phase field model is developed for two dimensional free dendrite growth of pure substances solidification. The dimensionless growth velocities obtained from simulations are compared with the calculations of a sharp interface method to present the capabilities of nondiagonal phase field model. Furthermore, the phase field simulation are also carried out when the cross-coupling term or the surface diffusion are turned off. We compare them with nondiagonal phase field results to evidence the necessity of using the nondiagonal phase field model.

According to Onsager's principles, the nondiagonal phase field model is extended to three phase transformations in **chapter 4**, such as eutectic solidification and eutectoid transformations. In the one-sided case, we compare the nondiagonal phase field results with boundary integral method calculations and the predictions of the Jackson-Hunt theory during eutectic solidification. In the two-sided case, the extended Jackson-Hunt theory is used to benchmark the nondiagonal phase field results during eutectoid and off-eutectoid transformations. The comparison results indicate the capabilities of the nondiagonal three-phase field model and the importance of the cross-coupling term.

The nondiagonal three-phase field model is derived based on a free energy functional in chapter 4, which is limited for simple symmetric phase diagrams. Therefore, in **chapter 5**, we develop a grand potential based nondiagonal three-phase field model for complex alloy transformations. The corresponding two-dimensional phase field simulations are implemented to investigate the growth kinetics of the pearlite transformation with respect to different diffusion paths. When the surface diffusion is eliminated, the simulation results are compared with the Zener-Hillert model in the one-sided case and Ankit's model in the two-sided case. Additionally, the influence of diffusion in cementite is also investigated. When the surface diffusion is considered, in the one-sided case, the growth velocities of the lamellae

is benchmarked with the predictions of Pandit's model. Subsequently, we take the diffusion in austenite and ferrite as well as the surface diffusion into account. The reproduced kinetics of pearlite growth are compared with experimental observations for different undercoolings.

In **chapter 6**, we summarize the results of this thesis.

Chapter 2

Theoretical background

2.1 Thermodynamic basics

2.1.1 Phase equilibrium

A binary alloy, consisting of two phases, i.e., phase 1 and phase 2, and two elements, i.e., A and B, is assumed at here. As shown in Fig. 2.1, the total number of atoms is defined as N in the system. The total number of atoms of type A in phase 1 is defined as $N_{A,1}$, and the total number of A atoms in the system is defined as N_A. Similarly, we define $N_{A,2}$, $N_{B,1}$ and $N_{B,2}$. Therefore, the numbers of atoms N, N_A and N_B are expressed as

$$N = N_A + N_B, \tag{2.1}$$

$$N_A = N_{A,1} + N_{A,2}, \tag{2.2}$$

$$N_B = N_{B,1} + N_{B,2}. \tag{2.3}$$

Additionally, the total number of atoms in phase i is

$$N_i = N_{A,1} + N_{B,1}. \tag{2.4}$$

Thus, the concentrations of A and B atoms in phase i are defined as

$$c_i^A = \frac{N_{A,i}}{N_i}, \tag{2.5}$$

$$c_i^B = \frac{N_{B,i}}{N_i}. \tag{2.6}$$

The Gibbs energy per particle in phase i is denoted as $g_i(c_i^A)$. For a constant temperature, the total Gibbs energy in the system is

$$G = N_1 g_i(c_1^B) + N_2 g_i(c_2^B). \tag{2.7}$$

Here, we have two choices for the independent variables in the expression of total Gibbs free energy. On the one hand, N_1 and $N_{B,1}$ are chosen as the independent variables, the expression of G can be written as

$$G(N_1, N_{B,1}) = N_1 g_1\left(\frac{N_{B,1}}{N_1}\right) + (N - N_1) g_2\left(\frac{N_B - N_{B,1}}{N - N_1}\right). \tag{2.8}$$

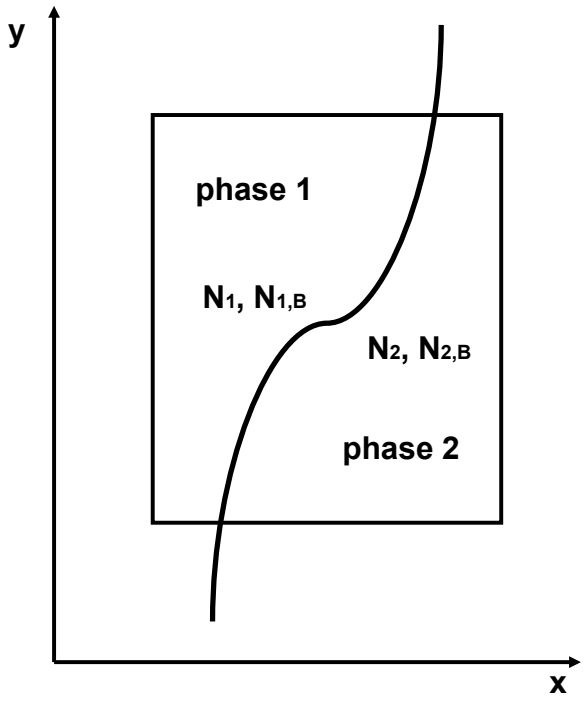

Figure 2.1: Sketch of a two-phase situation, where the interface contour $y(x)$ separates the two phases.

Afterwards, the difference of chemical potential and grand potential between phase 1 and 2 are

$$\delta\mu = \left(\frac{\partial G}{\partial N_{B,1}}\right)_{N_1} = g_1'(c_1^B) - g_2'(c_2^B), \tag{2.9}$$

$$\delta\omega = \left(\frac{\partial G}{\partial N_1}\right)_{N_{B,1}} = g_1(c_1^B) - c_1^B g_1'(c_1^B) - [g_2(c_2^B) - c_2^B g_2'(c_2^B)]. \tag{2.10}$$

On the other hand, $N_{A,1}$ and $N_{B,1}$ are able to be the independent variables, which yields the Gibbs free energy

$$\begin{aligned} G(N_{A,1}, N_{B,1}) =& (N_{A,1} + N_{B,1}) g_1 \left(\frac{N_{B,1}}{N_{A,1} + N_{B,1}}\right) + \\ & (N - N_{A,1} - N_{B,1}) g_2 \left(\frac{N_B - N_{B,1}}{N - N_{A,1} - N_{B,1}}\right). \end{aligned} \tag{2.11}$$

Then, variation with respect to $N_{A,1}$ gives

$$\delta\mu_A = \frac{\partial G}{\partial N_{A,1}} = g_1(c_1^B) - c_1^B g_1'(c_1^B) - [g_2(c_2^B) - c_2^B g_2'(c_2^B)], \tag{2.12}$$

which corresponds to the chemical potential difference between phase 1 and phase 2 for atom A. We should note that $\delta\mu_A$ is equivalent to the grand potential difference $\delta\omega$ in Eq. (2.10). In addition, another variation gives the chemical potential difference between phase 1 and phase 2 for atom type B

$$\delta\mu_B = \frac{\partial G}{\partial N_{B,1}} = g_1(c_1^B) - (1 - c_1^B) g_1'(c_1^B) - [g_2(c_2^B) - (1 - c_2^B) g_2'(c_2^B)]. \tag{2.13}$$

Notably, $\delta\mu_B = \delta\mu + \delta\omega$. At equilibrium, we have

$$\delta\mu = \delta\omega = 0, \tag{2.14}$$

$$\delta\mu_A = \delta\mu_B = 0, \tag{2.15}$$

which are equivalent and consistent.

2.1.2 Non-equilibrium thermodynamics

In 1931, Onsager proposed the reciprocal relations to describe the transport phenomena in electrolytes [1, 2], which provide a new insight into the transport and rate processes in the field of nonequilibrium thermodynamics. Non-equilibrium thermodynamics establishes the phenomenological equations with the conjugated flows and forces from the rate of entropy production or from the dissipation function. When the phenomenological equations linearly relate the conjugated flows and forces, the phenomenological coefficients obey the Onsager reciprocal relations. Therefore, the cross-coupled phenomenological coefficients are identical and the unknown coefficients are reduced. In addition, the phenomenological coefficients are of great importance in the definition of the coupled phenomena. For instance, the Soret effect (the mass diffusion due to heat transfer) and the Dufour effect (heat transport due to mass diffusion) can arise during the coupled processes of heat and mass transport. Thus, for separate disciplines, the linear nonequilibrium thermodynamics provides a unified approach to link different processes. For the discovery of reciprocal relations, Lars Onsager was awarded the Nobel Prize in Chemistry in 1968. Onsager's relations is also described as the "Fourth law of thermodynamics" [3].

Furthermore, the linear nonequilibrium thermodynamics is constructed based on four assumptions [4]: (i) The system is in a weak out of equilibrium state, where the gradients or the thermodynamic driving forces are not strong (quasi-equilibrium state). (ii) All the driving forces are linearly related to the fluxes and the proportionality constants are the phenomenological coefficients. (iii) The matrix of phenomenological coefficients is symmetric provided that the conjugate flows and forces are identified by the entropy production equation or the dissipation function. (iv) The coupling is restricted by a general symmetry principle according to the Curie-Prigogine principle. In the following, the Onsager linear relation is shortly explained for the conjugated forces ($\delta\omega$, $\delta\mu$) and fluxes ($\dot{N}_1$, $\dot{N}_{B,1}$).

On the one hand, for the first representation of $G(N_1, N_{B,1})$, the conjugate thermodynamic variable to N_1 is $\partial G/\partial N_1 = \delta\omega$. Similarly, the conjugate variable to $N_{B,1}$ is $\partial G/\partial N_{B,1} = \delta\mu$. Then, in the spirit of Onsager relations, we can write

$$\delta\omega = \bar{\mathcal{A}}_1\dot{N}_1 + \bar{\mathcal{B}}_1\dot{N}_{B,1}, \tag{2.16}$$

$$\delta\mu = \bar{\mathcal{B}}_1\dot{N}_1 + \bar{\mathcal{C}}_1\dot{N}_{B,1}. \tag{2.17}$$

The dissipation can be expressed as

$$\begin{aligned}\frac{\mathrm{d}G}{\mathrm{d}t} &= \left(\frac{\partial G}{\partial N_1}\right)_{N_{B,1}}\dot{N}_1 + \left(\frac{\partial G}{\partial N_{B,1}}\right)_{N_1}\dot{N}_{B,1} \\ &= \delta\omega\dot{N}_1 + \delta\mu\dot{N}_{B,1} \\ &= \bar{\mathcal{A}}_1\dot{N}_1^2 + 2\bar{\mathcal{B}}_1\dot{N}_1\dot{N}_{B,1} + \bar{\mathcal{C}}_1\dot{N}_{B,1}^2.\end{aligned} \tag{2.18}$$

On the other hand, for the second representation of $G(N_{A,1}, N_{B,1})$, we can write

$$\delta\mu_A = \bar{\mathcal{A}}_2\dot{N}_{A,1} + \bar{\mathcal{B}}_2\dot{N}_{B,1}, \tag{2.19}$$

$$\delta\mu_B = \bar{\mathcal{B}}_2\dot{N}_{A,1} + \bar{\mathcal{C}}_2\dot{N}_{B,1}, \tag{2.20}$$

with the dissipation

$$\begin{aligned}\frac{\mathrm{d}G}{\mathrm{d}t} &= \left(\frac{\partial G}{\partial N_{A,1}}\right)_{N_{B,1}}\dot{N}_{A,1} + \left(\frac{\partial G}{\partial N_{B,1}}\right)_{N_{A,1}}\dot{N}_{B,1} \\ &= \delta\mu_A\dot{N}_{A,1} + \delta\mu_B\dot{N}_{B,1} \\ &= \bar{\mathcal{A}}_2\dot{N}_{A,1}^2 + 2\bar{\mathcal{B}}_2\dot{N}_{A,1}\dot{N}_{B,1} + \bar{\mathcal{C}}_2\dot{N}_{B,1}^2.\end{aligned} \tag{2.21}$$

One can identify that

$$\bar{\mathcal{A}}_2 = \bar{\mathcal{A}}_1; \bar{\mathcal{B}}_2 = \bar{\mathcal{A}}_1 + \bar{\mathcal{B}}_1; \bar{\mathcal{C}}_2 = \bar{\mathcal{A}}_1 + 2\bar{\mathcal{B}}_1 + \bar{\mathcal{C}}_1, \tag{2.22}$$

which implies that both representations of total free energy consistently have symmetrical Onsager matrices.

2.1.3 Gibbs-Thomson effect

The Gibbs energy aforementioned is able to be extended by considering a continuum description of interfacial energy between the two phases (see Fig. 2.1)

$$G_{tot} = G + G_s \tag{2.23}$$

with

$$G_s = \int \gamma \mathrm{d}S = \gamma \int \sqrt{1 + y'(x)^2}\mathrm{d}x, \tag{2.24}$$

where $y(x)$ is the two-dimensional interface contour between the phases. To be explicit, we say that phase is located below this contour, $y < y(x)$. Standard variational calculus yields

$$\frac{\delta G_s}{\delta y(x)} = -\gamma\frac{\mathrm{d}}{\mathrm{d}x}\frac{\partial}{\partial y'}\sqrt{1+y'^2} = -\gamma\frac{y''}{(1+y'^2)^{1.5}} = \gamma\kappa, \tag{2.25}$$

where the curvature κ is defined to be positive for a convex solid.

For an equilibrium situation, the Gibbs energy is minimized with consideration of the interfacial energy. Here, it is important that the interface contour is related to the number of atoms in the solid phase via the relation

$$N_1 = \frac{1}{v}\int y(x)\mathrm{d}x, \tag{2.26}$$

with v being the atomic volume. Therefore, we write the Gibbs energy as functional, $G_{tot} = G(y, N_1)$, and obtain for the functional variation

$$\frac{\delta G_{tot}}{\delta y} = \frac{\delta G_s}{\delta y} + \frac{\partial G}{\partial N_1}\frac{\delta N_1}{\delta y}. \tag{2.27}$$

From the above expressions we therefore get the first equilibrium condition (generalized grand potential balance)

$$\frac{\delta G_{tot}}{\delta y} = \gamma\kappa + \frac{1}{v}\delta\omega = 0, \tag{2.28}$$

which is the Gibbs-Thomson effect. The other equilibrium condition remains the same,

$$\frac{\partial G_{tot}}{\partial N_{B,1}} = \delta\mu = 0. \tag{2.29}$$

For deviations from equilibrium situation, we can write again the linear Onsager relations

$$v\gamma\kappa + \delta\omega = \bar{\mathcal{A}}_1\dot{N}_1 + \bar{\mathcal{B}}_1\dot{N}_{B,1}, \tag{2.30}$$

$$\delta\mu = \bar{\mathcal{B}}_1\dot{N}_1 + \bar{\mathcal{C}}_1\dot{N}_{B,1}. \tag{2.31}$$

From this, we get the dissipation

$$\begin{aligned}
\frac{\mathrm{d}G}{\mathrm{d}t} &= \int \frac{\delta G_{tot}}{\delta y}\dot{y} + \frac{\partial G_{tot}}{\partial N_{B,1}}\dot{N}_{B,1} \\
&= \int (\gamma\kappa + \frac{1}{v}\delta\omega)\dot{y}\mathrm{d}x + \delta\mu\dot{N}_{1,B} \\
&= (A\dot{N}_1 + B\dot{N}_{B,1})\int \frac{1}{v}\dot{y}\mathrm{d}x + \bar{\mathcal{B}}_1\dot{N}_1 + \bar{\mathcal{C}}_1\dot{N}_{B,1}\dot{N}_{B,1} \\
&= \bar{\mathcal{A}}\dot{N}_1^2 + 2\bar{\mathcal{B}}\dot{N}_1\dot{N}_{B,1} + \bar{\mathcal{C}}_1\dot{N}_{B,1}^2,
\end{aligned} \tag{2.32}$$

which has the identical formation as Eq. (2.21).

2.2 The phase field method

Nowadays, the phase field method has been rapidly evolved as a powerful tool to simulate complex microstructure evolution, various growth patterns and other phenomena during materials preparation processes in many fields of research. The history of the phase field method can be traced to the model of van de Waals for a liquid-gas system by using a continuous density function at the liquid-gas interface more than a century ago [5] being reviewed in Refs. [6–11]. 50 years ago, Ginzburg and Landau proposed an order parameter to model the surperconductivity [12]. Almost 40 years ago, Cahn and Hillert proposed the coupled diffuse interface between two coexisting phases whose thickness depends on the temperature, and it turns out that the interfacial energy is consistent with the experimental observations [13]. In the review of Hohenberg and Halperin, model C is very similar to the current phase field method [14]. About 20 years ago, the diffuse interface has been introduced to the phase field method, which has become the characteristic feature. Moreover, according to the application of phase field models, they can be classified into two approaches in this community.

The first type of phase field model is developed by Chen [15] and Wang [16] according to the microscopic theory of Khachaturyan [17, 18]. The phase field variables present the local composition or long-range atomic order parameters, symmetry and orientation relations between coexisting phases. The application of this

kind of phase field method focuses on diffusive transformations [19–36], displacive transformations [37–51], coarsening mechanisms [52–62], deformation mechanisms [63–68] as well as ferroelectric and magnetic domain evolution [69–78].

The second type of phase field model is applied for reproducing the microstructure evolution during solidification, such as the famous dendrite growth, eutectic solidification and other commercial alloys solidification processes. Langer and Collins [79, 80] introduced the phase field method to model the pattern selection during solidification of a pure melt. Later, Kobayashi achieved the earliest application of the phase field method to dendrite growth during solidification [81]. Karma and Rappel proposed the thin interface limit to link the phase field model with free boundary conditions for equal thermal diffusivity in the solid and liquid phase during solidification (symmetric model) [82–84], namely quantitative phase field model. This pioneering work made it possible to remove abnormal interface effects and achieve local equilibrium boundary conditions by choosing the appropriate phase field kinetic parameters. Afterwards, the quantitative phase field model was extended to binary alloys with negligible solid diffusivity during solidification (one-sided model) [85]. A correction term called anti-trapping current that is proportional to the interface velocity is introduced to remove the interface effects originating from the discontinuity of the chemical potential in the interface. For eutectic solidification, Folch and Plapp developed a quantitative PF model with anti-trapping current to reproduce the free boundary conditions in the one-sided model [86]. The advantage of this model is to ensure the disappearance of spurious third phases in the two-phase interface by proposing a fifth order interpolation function and linking the PF model to free boundary descriptions. For the two-sided case, Ohno and Matsuura extended the anti-trapping current by using an additional prefactor during three phase solidification [87–89]. To describe the complex microstructure evolution for multi-phase and multi-component alloys, Steinbach developed the multi-phase field model coupled with CALPHAD databases [7, 90–94]. Though assigning different phase field order parameters, each phase/grain distinguishes from others by its orientation or phase. Moreover, for the real physical systems, phase-field models for solidification coupled to fluid flow are also developed and help us understand the influence of flow on the microstructure evolution [95–98].

2.2.1 Phase field concepts

The phase field method consists of a pair of famous continuum equations, i.e., the Allen-Cahn equation and the Cahn-Hilliard diffusion equation. Compared with the sharp interface method, its characteristic feature is the diffuse interface. The most attractive advantage of phase field approach is to avoid tracking the explicit interface position by introducing a non-conserved phase field variable ϕ, which exhibits smooth spatial variations inside the diffuse interface on the scale of interface thickness (W), as shown in Fig. 2.2. Generally, the phase field is constant in the bulk phases, for instance, $\phi_\alpha = 1$ presents the α phase and $\phi_\beta = 1$ presents the β phase. $0 < \phi < 1$ indicates the interface zone. The interface between two different bulk phases is located at $\phi = 1/2$. The interface thickness defined in the phase field method has no physical meaning but is typically chosen orders of magnitude larger than the atomistic scale to improve the computational efficient for large scale simulations.

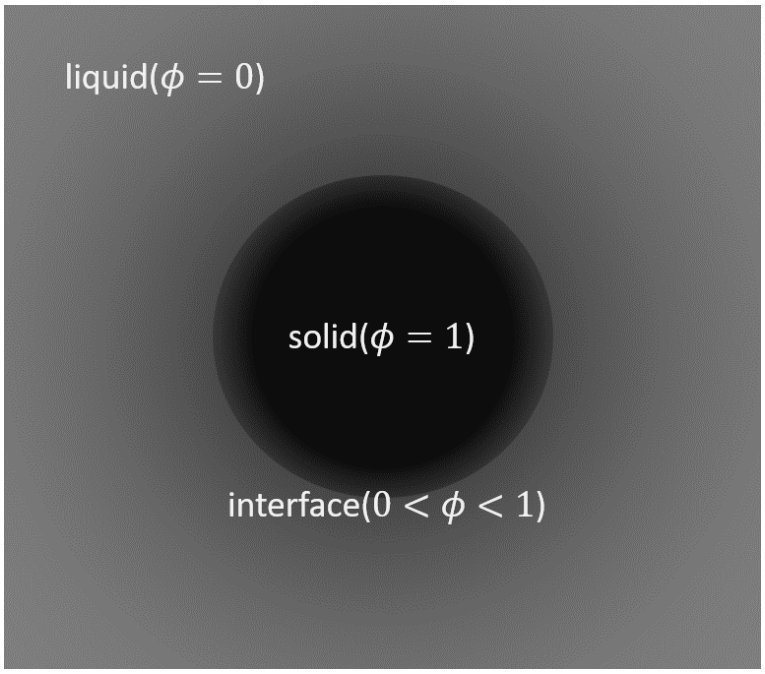

Figure 2.2: Demonstration of the phase field concepts.

The microstructure evolution of the parent phase to the growing phase is described by a free energy functional which contains the free energy of the bulk phases and the interfacial gradient energy. When the phase field order parameter is defined as ϕ, the free energy functional has the structure

$$F = \int_V [\kappa_\phi (\nabla\phi)^2 + f_w(\phi) + f_c(\phi, c)] \mathrm{d}V, \tag{2.33}$$

where the first term in the functional is the interfacial gradient energy contribution. κ_ϕ is the gradient energy coefficient, which is associated to the interface thickness. The second term is the well potential, while the last term indicates the chemical free energy density of the bulk phases.

For variational phase field models, the evolutional equation for phase field model is derivated from the free energy functional F. For the phase field parameter ϕ, according to the Allen-Cahn equation, we have

$$\frac{\partial\phi}{\partial t} = -M(\phi)\frac{\delta F}{\delta\phi}, \tag{2.34}$$

with $M(\phi)$ being the interface kinetic parameter. For a conserved field, like the concentration field, the overall amount of composition remains identical constant during the solidification. According to the Cahn-Hilliard equation, the evolution of concentration field is given by

$$\frac{\partial c}{\partial t} = \nabla \cdot \left(M_c \nabla \frac{\delta F}{\delta c} \right), \tag{2.35}$$

with M_c being the atomic mobility parameter. M_ϕ and M_c are determined based on the thermodynamic and physical properties of different alloys.

2.2.2 Thin interface limit

As mentioned in Section 2.2.1, the order parameters in the bulk phase are defined as constants, for instance, $\phi = 0$ indicates the liquid phase, while $\phi = 1$ is the solid phase. Two different bulk phases are smoothly separated by a diffuse interface with certain thickness W. To save simulation time and bridge the gap between the thickness of physical interface and the scale of microstructure observed in the experiments, the interface thickness (W) of diffuse interface is chosen several orders of magnitude larger than the physical interface width. However, the artificial enlargement of the interface thickness brings abnormal interface effects and the equilibrium boundary conditions violate. Therefore, all these anomalous interface effects have to be controlled in order to guarantee the precise phase field simulations. The pioneering work was done by Karma and Rappel in the symmetric model (identical diffusivity in the liquid and solid phases) during pure substances solidification for free dendrite growth, which is named "thin-interface limit". The spirit of thin-interface limit is that (i) the phase field and concentration field equations are expanded and analysed under the assumption that the interface thickness is much smaller than the diffusion length, (ii) the asymptotic procedure matches the solutions of inner and outer interface regions, which yields the equilibrium boundary conditions for finite interface thickness. The asymptotic procedure is shortly described in Appendix A.

Based on the developed thin-interface limit, Karma and Rappel carried out simulations in 1D, 2D and 3D for dendrite growth [84]. The 1D and 2D simulation results benchmarked with the predictions of the sharp interface theory. For small undercoolings, the convergence of the growth velocity of the dendrite tip was achieved by decreasing W/d_0, and the relative error of the growth velocity and tip radii between phase field simulations and solvability theory is smaller than 5%. Furthermore, in 3D simulations, the parameters of the phase field model was firstly calculated after determining the grid-induced anisotropy. Without the effects of grid anisotropy, the phase field simulations showed the error between simulations results and solvability theory predictions to be less than 10%.

However, it is impossible to eliminate all the abnormal interface effects simply by choosing the appropriate interpolation functions and parameters in the phase field equations in the one-sided (the solid diffusivity is negligible) and the two-sided (the solid diffusivity neither vanishes nor equals to liquid phase) cases [85, 99, 100]. Therefore, the anti-trapping current is proposed in Refs. [85, 100] in the one-sided case (the solid diffusivity is negligible), which can be written as

$$\mathbf{j}_{\mathbf{at}}^{\mathbf{one}} = a(\phi) W \dot{\phi} \mathbf{n}, \tag{2.36}$$

where $a(\phi)$ is an interpolation function (for one-sided case, $a(\phi) = 1/(2\sqrt{2})$), $\mathbf{n} = -\boldsymbol{\nabla}\phi/|\boldsymbol{\nabla}\phi|$ is the normal vector to the interface. This term contains a current which is proportional to the interface velocity to correct the flux in the interface region. For the two-sided case, the anti-trapping current with an additional prefactor is proposed in Ref. [87], which is given by

$$\mathbf{j}_{\mathbf{at}}^{\mathbf{two}} = a(1 - \frac{D_s}{D_l}) W \dot{\phi} \mathbf{n}. \tag{2.37}$$

Plapp pointed out the temperature jump can be eliminated by carrying out the asymptotic analysis after modifying the anti-trapping current. However, it is not

the only interface effect appearing in the two-sided case. The surface thermal resistance, named Kapitza resistance, is another nature interface effect [101–103]. It is proportional to the interface thickness and can not be fully eliminated by the velocity determined anti-trapping current [104]. Thus, to eliminate all the abnormal interface effects in the two-sided case, the thermodynamic fully consistent nondiagonal model is developed according to Onsager's relations, which is explained in Section 2.3.

2.2.3 Grand-potential based phase field model

The quantitative phase field models for the solidification of pure substances is achieved with the development of the "thin interface limit" as is detailed in Section 2.2.2. Through appropriately chosing the phase field parameters, the free boundary conditions are reproduced. However, the chemical free energy function in the free energy functional, such as Eq. (2.33), is unsuitable to reproduce all phase diagrams of complex binary alloys. Thus, for complex binary alloy solidification, the free-energy based phase field model is extended to the grand-potential based phase field model [105]. In analogy to the free energy functional, the grand-potential functional is

$$\begin{aligned}\Omega[\phi,\mu] &= \int_V \omega(\phi,\nabla\phi,\mu) \\ &= \int_V \omega_{int}(\phi,\nabla\phi) + g_s(\phi)\omega_s(\mu) + [1-g_s(\phi)]\omega_l(\mu),\end{aligned} \tag{2.38}$$

where $\omega_v(\mu)$ is the grand potential density of the bulk phases, which is given by

$$\omega_v(\mu) = f_v(c) - \mu\rho, \tag{2.39}$$

where $f_v(c)$ is the free energy density. μ is the chemical potential, which is defined as $\mu = V_a\delta F/\delta c$, with V_a being the atomic volume, ρ is the number density of the solute atoms, which is given by

$$\rho = \frac{c}{V_a}. \tag{2.40}$$

Then, for a given temperature, the variation of the grand potential density with respect to ϕ and μ are

$$\frac{\delta\Omega}{\delta\phi} = -\sigma\nabla^2\phi + Hf'_{dw}(\phi) + g'_s(\phi)[\omega_s(\mu) - \omega_l(\mu)], \tag{2.41}$$

$$\begin{aligned}\frac{\delta\Omega}{\delta\mu} &= -\rho(\phi,\mu) \\ &= g_s(\phi)\frac{\partial\omega_s(\mu)}{\partial\mu} + [1-g_s(\phi)]\frac{\partial\omega_l(\mu)}{\partial\mu} \\ &= g_s(\phi)\rho_s + [1-g_s(\phi)]\rho_l.\end{aligned} \tag{2.42}$$

Therefore, the grand-potential based phase field and chemical potential evolution equations are

$$\dot{\phi} = -M_\phi\frac{\delta\Omega}{\delta\phi} = M_\phi\left\{\sigma\nabla^2\phi - Hf'_{dw}(\phi) - g'_s(\phi)[\omega_s(\mu) - \omega_l(\mu)]\right\}, \tag{2.43}$$

$$\dot{\mu} = \frac{1}{\chi(\phi,\mu)} \left\{ \nabla[D(\phi,\mu)\chi(\phi,\mu)\nabla\mu] - g_s'(\phi)\left[\rho_s - \rho_l\right]\dot{\phi} \right\}, \tag{2.44}$$

with $\chi(\phi,\mu)$ being the susceptibility, which is defined as

$$\chi(\phi,\mu) = \frac{\partial\rho(\phi,\mu)}{\partial\mu} = g_s(\phi)\frac{\partial\rho_s(\mu)}{\partial\mu} + [1-g_s(\phi)]\frac{\partial\rho_l(\mu)}{\partial\mu}. \tag{2.45}$$

For given temperature and equilibrium concentration, the simplest approximation for free energy functions are parabolas, using the following formulation

$$f_v(c) = \frac{1}{2}\epsilon_v(c - c_v^{eq})^2, \tag{2.46}$$

where ϵ_v are constants to describe the curvatures of the parabolas. The chemical potential in each phase is

$$\mu = \frac{\partial f_v}{\partial\rho} = V_a\epsilon_v(c - c_v^{eq}), \tag{2.47}$$

The concentration c can be written as a function of μ,

$$c = \frac{\mu}{V_a\epsilon_v} + c_v^{eq}. \tag{2.48}$$

Therefore, based on Eq. (2.39), the grand potential density is

$$\omega_v(\mu) = -\frac{1}{2}\frac{\mu^2}{V_a^2\epsilon_v} - \frac{\mu}{V_a}c_v^{eq}. \tag{2.49}$$

Inserting the grand-potential density in Eq. (2.45) yields the expression of χ,

$$\chi(\phi,\mu) = \frac{1}{V_a^2\epsilon_s}g_s(\phi) + \frac{1}{V_a^2\epsilon_l}[1-g_s(\phi)]. \tag{2.50}$$

In this thesis, a grand potential based phase field model is presented in a variational framework, in analogy to Ref. [105]. The principal difference between the grand potential based and free energy based phase models is that the relation between the composition and chemical potential is nonlinear in the grand potential based phase field model rather than linear in the free energy based phase field model. Based on this advantage, the introduction of parameters ϵ_v in Eq. (2.46) provides more degrees of freedom to define the curvature of parabolic free energy, and the local equilibrium conditions (common tangent theory) can be satisfied in the phase field simulations. To benchmark this model, Plapp performed two-dimensional dendrite growth with different interface thickness for Ni-Cu alloy during solidification [105]. The convergent growth velocities of the dendrite tip indicate that the model can be applied to alloys with arbitary phase diagrams. Based on the advantages of grand potential phase field model, it is used in Chapter 5 to reproduce the free energy of stoichiometric cementite and find local equilibrium between austenite, ferrite and cementite phases during the pearlite transformation.

2.3 Non-diagonal phase field model

The phase field model solves moving patterns with the use of phase field variables ϕ which are continuous across the interface. The interface width is usually chosen significantly larger than the actual width of physical interface in order to save computational time. However, this causes an artificial enhancement of the interfacial kinetic effects, such as solute trapping, the interface stretching effect and surface diffusion which alters the conservation laws at the interface [99]. To eliminate the abnormal interface effects arised by the enlarged interface width W, a thin-interface limit calculation is carried out in the symmetric case, while the anti-trapping current is added into the conserved evolution equation in the one-sided case. For the general case, when a finite diffusion contrast exists between the parent phase and growing phase, the reproduction of the free boundary condition has been a long-standing unsolved problem in the phase field community.

Recently, this problem has been solved by introducing a kinetic cross-coupling term between the nonconserved phase field and the conserved diffusion field based on the Onsager relation, known as non-diagonal phase field model [106, 107]. This new cross-coupling term provides an additional degree of freedom to reproduce equilibrium boundary conditions for unequal diffusivities in the different bulk phases. Boussinot and Brener presented the non-diagonal phase field model with the kinetic cross-coupling term for isothermal transformations in binary alloys and steps dynamics in molecular-beam-epitaxy [108]. Later, they achieved a realistic description of interface kinetics with a diffusional contrast for pure substances during isothermal solidification [109], which is explained in Section 2.3.1. In addition, they also pointed out this new term allows to obtain the desired interface kinetics [110]. In this section, the nondiagonal phase field model for pure substances during isothermal solidification is shortly explained. Since the two models are similar, the nondiagonal phase field model for binary alloys during isothermal solidification is explicated in Appendix B.

2.3.1 Nondiagonal phase field model for pure substances during isothermal solidification

For crystallization of a solid from a pure melt, the local temperature is the driving force for the phase transformation and one must determine temperature fields in both solid and liquid phases subject to the free boundary conditions. In this section, the non-diagonal phase field model for pure materials during solidification is introduced.

Evolution equations

The total entropy functional S of the system is

$$S = \int_V \mathrm{d}V \left\{ s[e(T,\phi),\phi] - H\left[\frac{(1-\phi^2)^2}{4} + \frac{(W\nabla\phi)^2}{2}\right]\right\}, \tag{2.51}$$

where e is the dimensionless internal energy density, which depends on temperature T and phase field ϕ and obeys the continuity equation

$$\dot{e} = -\nabla \cdot J, \tag{2.52}$$

with J being the flux of the dimensionless energy. The entropy production of the system is

$$\dot{S} = \int_V \mathrm{d}V \left[\frac{\delta S}{\delta \phi} \dot{\phi} + \frac{\delta S}{\delta e} \dot{e} \right] = \int_V \mathrm{d}V \left[\frac{\delta S}{\delta \phi} \dot{\phi} + \nabla \frac{\delta S}{\delta e} \cdot J \right]. \tag{2.53}$$

The driving force conjugated to $\dot{\phi}$ is $\delta S/\delta \phi$, while the driving force conjugated to J is $\nabla(\delta S/\delta e)$. Hence, the variational equations of nondiagonal phase field model with nondiagonal term which obeys Onsager symmetry during pure substance solidification are

$$\frac{c_p T_M^2}{L^2} \frac{\delta S}{\delta \phi} = \tau(\phi)\dot{\phi} + M(\phi) W \nabla \phi \cdot J, \tag{2.54}$$

$$\frac{c_p T_M^2}{L^2} \nabla \frac{\delta S}{\delta e} = M(\phi) W \nabla \phi \dot{\phi} + \frac{J}{D(\phi)}, \tag{2.55}$$

where c_p is the specific heat at the melting temperature T_M. L is the latent heat of the transformation. $\tau(\phi)$ and $M(\phi)$ are relaxation time and cross-coupling term, respectively, which are considered as constants for two phase transformations. $D(\phi)$ is the thermal diffusivity. The positive entropy production $\dot{S} > 0$ demands

$$\tau(\phi) > 0, D(\phi) > 0, \Delta = 1 - [M(\phi) W \nabla \phi]^2 D(\phi)/\tau(\phi) > 0. \tag{2.56}$$

Then, the evolution equations of phase field and temperature are

$$\Delta \tau \dot{\phi} = \tilde{H} \left[\phi(1-\phi^2) + W^2 \nabla^2 \phi \right] - \frac{p'(\phi)}{2} u + MW D(\phi) \nabla \phi \cdot \nabla u, \tag{2.57}$$

$$\dot{u} = \nabla \left\{ D(\phi) [\nabla u + MW \dot{\phi} \nabla \phi] \right\} + \frac{p'(\phi)}{2} \dot{\phi}, \tag{2.58}$$

where $p(\phi) = 15(\phi - 2\phi^3/3 + \phi^5/5)/8$. u is the dimensionless temperature, which is $u = c_p(T - T_M)/L$. The phase field at equilibrium is

$$\phi_{eq}(x) = -\tanh\left(\frac{x}{W\sqrt{2}} \right). \tag{2.59}$$

The equilibrium dimensionless entropy is

$$\sigma_{eq}(\phi) = \frac{\sigma_S + \sigma_L}{2} - \frac{\sigma_L - \sigma_S}{2} p(\phi_{eq}). \tag{2.60}$$

Link between boundary conditions and phase field parameters

In the macroscopic description, the energy conservation equation at the interface can be written as

$$D_S \nabla u|_S \cdot \mathbf{n} + V\sigma_S = D_L \nabla u|_L \cdot \mathbf{n} + V\sigma_L, \tag{2.61}$$

where D_S and D_L are the thermal diffusivities in the solid and liquid phases. $\mathbf{n}$ is the vector normal to the interface. $\nabla u|_S$ and $\nabla u|_L$ indicate the gradient of dimensionless temperature on the solid and liquid side of the interface. V is the normal velocity of interface motion and J_E denotes the normal flux of dimensionless energy through the interface. The relation between driving forces and fluxes becomes

$$\frac{c_p T_M}{L} \delta f = \sigma_S u_S - \sigma_L u_L = \bar{\mathcal{A}} V + \bar{\mathcal{B}} J_E + d_0 \kappa, \tag{2.62}$$

$$\delta u = u_L - u_S = \bar{\mathcal{B}} V + \bar{\mathcal{C}} J_E. \tag{2.63}$$

In analogy to Eqs. (B.33) to (B.35), the Onsager kinetic parameters of pure materials solidification are

$$\begin{aligned}\bar{\mathcal{A}} = &\int_{-\infty}^{\infty} dx \left\{\tau(\phi_{eq})[\phi'_{eq}(x)]^2\right\} - 2\int_{-\infty}^{\infty} dx M(\phi_{eq}) W [\phi'_{eq}(x)]^2 [\sigma_{eq}(x)] \\ &+ \int_{-\infty}^{\infty} dx \frac{\sigma_{eq}^2(x)}{D(\phi_{eq})} - \frac{(\sigma_S^{eq})^2}{2D_S} - \frac{(\sigma_L^{eq})^2}{2D_L},\end{aligned} \tag{2.64}$$

$$\bar{\mathcal{B}} = \int_{-\infty}^{\infty} \mathrm{d}x \left\{ M(\phi_{eq}) W [\phi'_{eq}(x)]^2 - \left[\frac{\sigma_{eq}(x)}{D(\phi_{eq})} - \frac{\sigma_S^{eq}}{2D_S} - \frac{\sigma_L^{eq}}{2D_L} \right] \right\}, \tag{2.65}$$

$$\bar{\mathcal{C}} = \int_{-\infty}^{\infty} \mathrm{d}x \left[\frac{1}{D(\phi_{eq})} - \frac{1}{2D_S} - \frac{1}{2D_L} \right]. \tag{2.66}$$

Determination of the non-diagonal phase field parameters in two-sided cases

Equilibrium boundary conditions require the elimination of a temperature and energy jump, which leads to $\delta f = f = \delta u = 0$. Then the Onsager kinetic parameters become $\bar{\mathcal{A}} = \bar{\mathcal{B}} = \bar{\mathcal{C}} = 0$. Firstly, the diffusivity function $D(\phi)$ is chosen as

$$\frac{1}{D(\phi)} = \left(\frac{1}{2D_S} + \frac{1}{2D_L} \right) + g(\phi) \left(\frac{1}{2D_S} - \frac{1}{2D_L} \right), \tag{2.67}$$

to ensure $\bar{\mathcal{C}} = 0$, with $g(\phi)$ being an odd function, which is defined as

$$g(\phi) = \phi[1 + a(1 - \phi^2)], \tag{2.68}$$

where a is a tuning parameter to adjust the surface diffusion along the interface. Generally, the surface diffusion along solid/liquid interface is neglected during a solidification process, i.e. $D_{surf} = \int_{-\infty}^{\infty} \mathrm{d}x[D(\phi) - 1/2D_S - 1/2D_L] = 0$. Moreover, with the choice of the diffusivity expression and an odd function $g(\phi)$, the Onsager kinetic parameter $\bar{\mathcal{C}}$ automatically vanishes. Then, $\bar{\mathcal{B}} = 0$ yields

$$M = \frac{\gamma W}{2\alpha} \left(\frac{1}{2D_S} - \frac{1}{2D_L} \right), \tag{2.69}$$

where

$$\alpha = W \int_{-\infty}^{\infty} \mathrm{d}x [\phi'_{eq}(x)]^2 = 2\sqrt{2}/3, \tag{2.70}$$

$$\gamma = \int_{-\infty}^{\infty} \frac{\mathrm{d}x}{W} \{1 - p[\phi_{eq}(x)] g[\phi_{eq}(x)]\}. \tag{2.71}$$

It is noteworthy that α is different for different $\phi_{eq}(x)$ and γ is dependent on the parameter a in Eq. (2.68). Subsequently, with the choice of $D(\phi)$ and M, the parameter τ is

$$\tau = \frac{\beta W^2}{4\alpha} \left(\frac{1}{2D_S} + \frac{1}{2D_L} \right), \tag{2.72}$$

where

$$\beta = \int_{-\infty}^{\infty} \frac{\mathrm{d}x}{W}\{1 - p[\phi_{eq}(x)]^2\} \approx 1.40748. \tag{2.73}$$

Then, Inserting Eqs. (2.69) and (2.72) to Eq. (2.56) with relation $(W\phi'_{eq})^2 = (1 - \phi_{eq}^2)^2/2$ yields the stability constraint

$$1 < \frac{2\beta\alpha}{\gamma^2\mu_{diff}^2} \min \frac{1 + \mu_{diff} g(\phi_{eq})}{(1 - \phi_{eq}^2)^2}, \tag{2.74}$$

where $\mu_{diff} = (D_L - D_S)/(D_L + D_S)$. We should note that the positive determinant $\Delta > 0$ sets an upper and lower bound for the diffusion ratio ($1/17 < D_S/D_L < 17$). If the diffusion contrast is out of this range, i.e., $D_S/D_L < 1/17$ or $D_S/D_L > 17$, the one-sided model can be ultilized for the simulations. The nondiagonal phase-field simulations were performed by Boussinot et. al to investigate the relaxation of an interface with a periodic perturbation towards the equilibrium flat shape with and without the influence of surface diffusion in two-dimension [110]. They pointed out that not only the surface diffusion increases the dimensionless velocity but also the temperature difference at the interface ($\phi = 0$) is significantly decreased by introducing the cross-coupling term M, which indicates the equilibrium boundary conditions are achieved in two-sided case.

In summary, the nondiagonal phase field model for pure substances solidification developed in Ref. [109] is presented in this section. Comparing with quantitative phase field model in Refs. [84, 85], a cross-coupling term between conserved and nonconserved fields is introduced in nondiagonal phase field model according to Onsager's relation. Through linking nondiagonal phase field model with free boundary conditions, the relaxation time (τ) and cross-coupling coefficient (M) is determined after eliminating the grand potential and diffusion potential jumps. In turn, one also can obtain the desired $\delta\Omega$ and $\delta\mu$ through tuning τ and M. Furthermore, the constraints mentioned in Ref. [99] is also fulfilled in the nondaigonal phase field model. On the one hand, with the switching function $p(\phi)$, the interface stretching effect that indicates the interface adsorption and modifies the conservation law is eliminated due to $\int_{-\infty}^{\infty} \mathrm{d}x[\sigma_{eq}(x) - \sigma_S/2 - \sigma_L/2] = 0$. On the other hand, the tangent surface diffusion along the interface is vanished to correct the conservation law with the appropriate a in Eq. (2.68). Although the nondiagonal phase field is a thermodynamic consistent model, in which an extra degree of freedom is provided to reproduce the free boundary conditions case and the anti-trapping current term also naturally appears in the two-sided case, the numerical benchmarks have not been performed yet to demonstrate the capabilities of this model. Furthermore, the aforementioned nondiagonal phase field model is only suitable for two phase transformation and its application is constrained for pure substance and binary alloy solidifications. Therefore, in this thesis, the nondiagonal phase field model is extended to the dendrite growth with the consideration of anisotropy in Chapter 3 and to three phase transformations in spirit of Onsager's relations, such as eutectic and eutectoid transformations in Chapters 4 and 5.

2.4 Dendritic solidification

In metallurgy, a dendrite is the tree-like structure of crystals growing from an undercooled melt phase. At the beginning, a spherical solid nucleus forms in the

undercooled melt. Due to perturbations, the spherical shape becomes unstable, and the preferred growth directions have a higher growth velocity according to the anisotropic properties of the crystal, as shown in Fig. 2.3. Theoretical models of dendrite growth are shortly explained in the following.

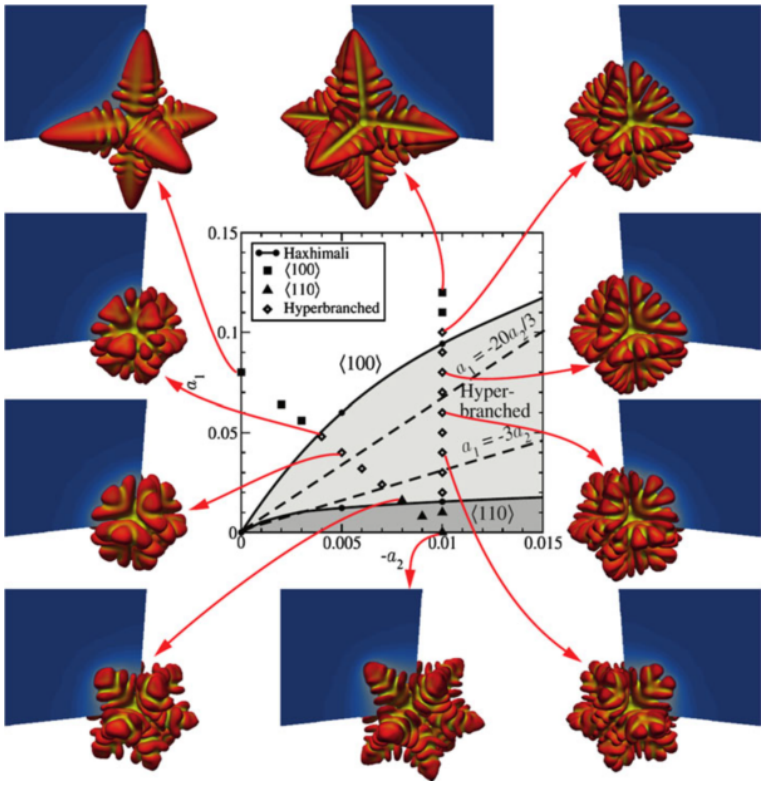

Figure 2.3: Phase field results for equiaxed growth of Al-0.1 Zn alloy with different anisotropic parameters when the dimensionless undercooling is 0.4. The picture is taken from Ref. [111]

2.4.1 Mullins-Sekerka Stability

Starting from a protrusion, a flat interface can transform into various morphologies, such as celluar, dendritic or fractal patterns. The stability of the initial planar interface is governed by the concentration or temperature field ahead of the protrusion. To analyze the stability transition from planar to cellular growth, Mullins and Sekerka have estabilished the theory [112]. With the consideration of the free boundary conditions at the interface, the Mullins-Sekerka theory presents the expression of the change of the protrusion's amplitude for different perturbation wavelengths.

The Mullins-Sekerka theory assumes a flat solidification front with a small sinusoidal shaped perturbation growing into z-direction with the velocity v, as depicted in Fig. 2.4. The wave number of the perturbation is defined as ω_{MS} and the corresponding wavelength λ_{MS} is $1/\omega_{MS}$. Then, the perturbed interface position z can be written as function of time t and x-coordinate

$$z(x,t) = \delta(t)\sin(\omega_{MS}x), \tag{2.75}$$

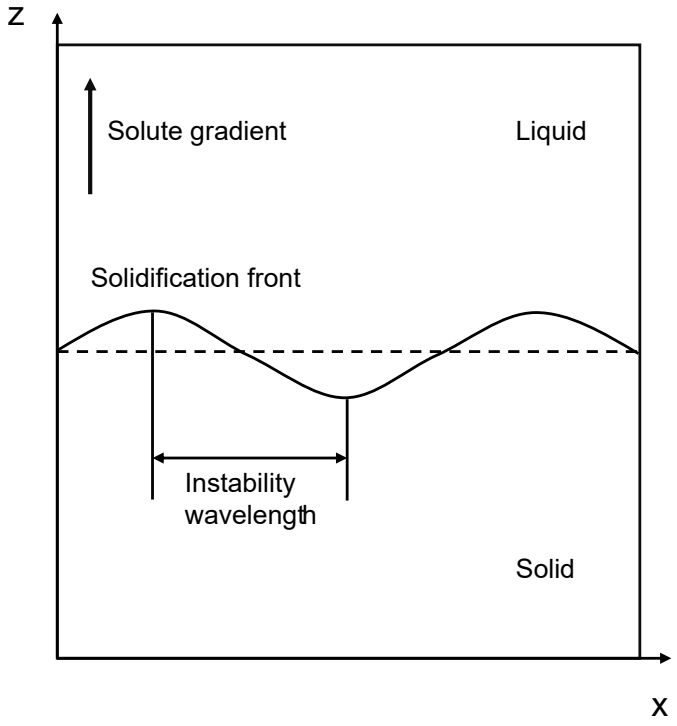

Figure 2.4: Illustration of the Mullins-Sekeraka instability.

where δ is the amplitude of the perturbation, which is the function of t. The spatial concentration $c(x, z)$ is

$$c(x, z) = c_0(x, z) + \delta_c \sin(\omega_{MS} x) e^{-k_\omega z}, \tag{2.76}$$

where $c_0(x, z)$ is the concentration of the flat front at steady state, δ_c is the amplitude decaying in z-direction, k_ω is the decay rate. For perturbations with different wavelengths, frequency and decay rate, the solidification front may either decay to the planar growth pattern or amplify the perturbation. The rate of change of the amplitude predicted by Mullins and Sekerka is given by

$$\frac{\dot{\delta}}{\delta} = \left[k_\omega - \frac{vp}{D_l}\right]\left(-\frac{D_l G}{m c_0 p} - \frac{D_l \Gamma \omega_{MS}^2}{m c_0 p} + v g(\omega)\right), \tag{2.77}$$

where D_l is the diffusivity of the liquid phase, Γ is the Gibbs-Thomson coefficient, G is the thermal gradients in the directional solidification, m is the liquidus slope, p is the partition coefficient. The decay rate of the wave number k_ω is

$$k_\omega = \frac{v}{2D_l} + \sqrt{\left(\frac{v}{2D_l}\right)^2 + \omega_{MS}^2}, \tag{2.78}$$

and $g_(\omega)$ is given by

$$g_(\omega) = 1 - \frac{2 - 2p}{\sqrt{1 + \left(\frac{2D_l \omega_{MS}}{v}\right)^2} + 1 - 2p}. \tag{2.79}$$

For isothermal solidification, i.e. $G = 0$, Eq. (2.77) becomes

$$\frac{\dot{\delta}}{\delta} = \left[k_\omega - \frac{vp}{D_l}\right]\left(-\frac{D_l\Gamma\omega_{MS}^2}{mc_0p} + vg(\omega)\right). \tag{2.80}$$

$\dot{\delta}$ is an important parameter to control the evolution of the perturbation and the stability of the solidification front. The figure of $\dot{\delta}$ versus λ_{MS} is plotted in Fig. 2.5. In Fig. 2.5, on the one hand, for negative $\dot{\delta}$, the perturbation decays with time and finally vanishes. On the other hand, for positive $\dot{\delta}$, the perturbation is amplified and the flat solidification front is unstable. For $\dot{\delta} = 0$, a critical wavelength λ_{cri} is determined, which indicates the limit of stabilization.

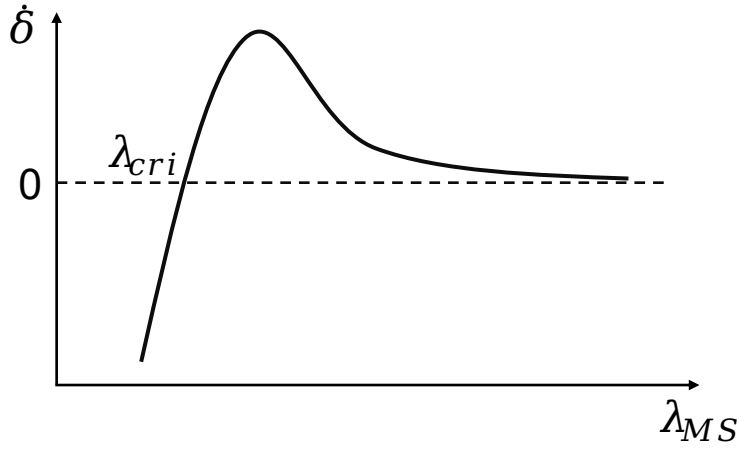

Figure 2.5: Illustration of change rate of the amplitude $\dot{\delta}$ according to Mullins and Sekeraka predictions. When $\lambda_{MS} = \lambda_{cri}$, the amplitude of the perturbation is stable. When $\lambda_{MS} < \lambda_{cri}$, the perturbation is reduced to the flat interface. When $\lambda_{MS} > \lambda_{cri}$, the perturbation is amplified to form dendrites.

2.4.2 Dendrite growth in the symmetric model

In the symmetric case, where the liquid and solid phases have identical thermal diffusivity, two analytical models were developed for small undercooling. The first one is named BA-P model [113] based on the mathematical method developed by Kruskal and Segur [114]. The second one is developed by Barbieri et al. [115], who adopted Shraiman's point [116] on the Saffman-Taylor problem to derive and evaluate a solvability condition for the existence of steady-state dendrite growth solution. These theories predict the degeneracy of the Ivantsov parabola in the presence of a weakly anisotropic surface energy. Moreover, for finite Peclet number p, Caroli et al. concluded that the selected velocity scales as p^2 for all undercooling [117].

Assuming crystal growth from an undercooled melt, the temperature in the melt $T(x, y, t)$ is governed by the

$$\frac{\partial T}{\partial t} = D\nabla^2 T, \tag{2.81}$$

the boundary condition at the solidification front is

$$c_p D[\mathbf{n}\nabla T_1 - \mathbf{n}\nabla T_c] = -Lv_n, \tag{2.82}$$

where c_p is the specific heat, D is the thermal diffusivity, L is the latent heat, v_n is the normal velocity, $\mathbf{n}$ is the normal vector of the interface. According to the Gibbs-Thomson effect, the temperature along the growth front deviates from the melting temperature due to the front curvature without considering kinetic effects,

$$T(x,y,t) = T_m + \frac{T_m \gamma(\theta)}{L}\kappa(x,t), \tag{2.83}$$

where T_m is the melt temperature, $\gamma(\theta)$ is the surface energy, which is dependent on the angle between the normal vector and the y-axis, κ is the curvature of the solidification front,

$$\kappa(x,t) = \frac{d^2y(x)}{\mathrm{d}x^2}\left[1+\left(\frac{\mathrm{d}y}{\mathrm{d}x}\right)^2\right]^{-1.5}. \tag{2.84}$$

Therefore, Eqs. (2.81) to (2.83) yield an integro-differential equation to depict the solidification front in the symmetric model [118],

$$\begin{aligned}\Delta + \frac{d_0\kappa(x,t)}{\rho} = \frac{p}{2\pi}\int_0^\infty \frac{d\tau}{\tau}\int_{-\infty}^{\infty}\mathrm{d}x'\dot{y}(x,t-\tau) \\ \times \exp\left\{-\frac{p}{2\tau}\left[(x-x')^2+[y(x,t)-y(x',t-\tau)]\right]^2\right\},\end{aligned} \tag{2.85}$$

where ρ is the radius of parabola, which is the unit of all measured length. $p = v\rho/2D$ is the Peclet number, $\Delta = (T_m - T_\infty)/(L/c)$ is the dimensionless undercooling. At zero surface energy, the steady-state solution of Eq. (2.85) is the Ivantsov parabola

$$y = t - \frac{1}{2}x^2, \tag{2.86}$$

and the relation between Δ and p is

$$\Delta(p) = 2p^{1/2}\exp p\int_{p^{1/2}}^{\infty}\exp(-x^2)\mathrm{d}x. \tag{2.87}$$

For nonzero surface energy case, this solution is modified by a shape correction term $\zeta(x)$, and the modified steady state solution is [119]

$$y(x,t) = t - \frac{1}{2}x^2 + \zeta(x), \tag{2.88}$$

where $\zeta(x)$ satisfies

$$\begin{aligned}A_d(\theta)\sigma_d[\zeta''-1][1+(\zeta'-x)^2]^{-3/2} = \frac{p}{\pi}\int_{-\infty}^{\infty}\mathrm{d}x'[\zeta(x')-\zeta(x)]\exp[\frac{1}{2}p(x^2-x'^2)] \\ \times\left[K_0(pR) - K_1(pR)\frac{x^2-x'^2}{2R}\right],\end{aligned} \tag{2.89}$$

where

$$R = [(x-x')^2 + (x^2-x'^2)^2/4]^{1/2}. \tag{2.90}$$

$$A_d(\theta) = 1 - \alpha_d\cos 4(\theta-\theta_d), \tag{2.91}$$

with α_d being the anisotropy parameters ($\alpha_d \ll 1$). σ_d is a constant, which is given by

$$\sigma_d = \frac{d_0}{p\rho}. \tag{2.92}$$

2.4.3 Dendrite growth in the one-sided model

In the one-sided case, where the diffusivity in the solid phase is negligible compared to that in the liquid phase, Saito et al. studied the two-dimensional dendrite growth by using Green's functions. It is found that anisotropy in the surface energy is necessary for dendrite growth, and the selected velocity and tip radius is a function of undercooling and anisotropy [120, 121]. The calculated dendrite shapes for various anisotropic coefficient are presented in Fig. 2.6. Misbah predicted that the tip velocity of the dendrite is twice larger than that in the symmetric model for small and finite undercooling [122].

Firstly, we write down the equations of free boundary condition in one-sided case [120]

$$\partial u(x,z,t)/\partial t = \nabla^2 u + (v/D)\partial u/\partial z, \tag{2.93}$$

$$u_s = \Delta - d_0[1 + a_m \cos(m\theta)]\kappa, \tag{2.94}$$

$$-D\mathbf{n}\nabla u_s \approx v\mathbf{n_z}, \tag{2.95}$$

where $u(x,y,t)$ is the dimensionless diffusion field, Δ is the dimensionless undercooling, D is the thermal diffusivity, d_0 is the capillary length, a_m is the m-fold anisotropic coefficient , and κ is the curvature of the solidification front. Using the Green's function techniques, Caroli et al. [123] and Misbah [122] have presented the integro-differential equation for one-sided model,

$$\begin{aligned}\frac{\Delta}{p} - \frac{\sigma}{2}A(x)\kappa(x) = \frac{1}{\pi}\int_{-\infty}^{\infty} \mathrm{d}x' e^{-p(\zeta(x)-\zeta(x'))} \\ \times K_0(p\beta) + \frac{p\sigma}{2\pi}\int_{-\infty}^{\infty}\mathrm{d}x' A(x')\kappa(x')\Bigg[K_0(p\beta) \\ + \frac{(x-x')\zeta(x') + \zeta(x') - \zeta(x)}{\beta}K_1(p\beta)\Bigg] \times e^{-p(\zeta(x)-\zeta(x'))},\end{aligned} \tag{2.96}$$

where

$$\beta = [(x-x')^2 + (\zeta(x) - \zeta(x'))^2]^{1/2}, \tag{2.97}$$

σ is a dimensionless parameter, which is given by

$$\sigma = \frac{d_0}{2p^2}v. \tag{2.98}$$

2.4.4 Dendrite growth in the two-sided model

In the more general two-sided case, where $\mu = D_S c_S/D_L c_L$ is not equal to 1 nor negligible, Barbieri and Langer derived two integro-differential equations from the equilibrium boundary conditions for general values of p and μ [124], named Barbieri-Langer theory. With the limit $p \to 0$, two integro-differential equations are combined into a new form. However, the new integro-differential equation in the two-sided model is more sophisticated to carry out than in the symmetric model. Only the relation between the dimensionless velocity $\sigma^*(\mu)$ with $\sigma^*(\mu = 1)$ is

$$\sigma^*(\mu) \simeq \frac{2}{1+\mu}\sigma^*(\mu = 1). \tag{2.99}$$

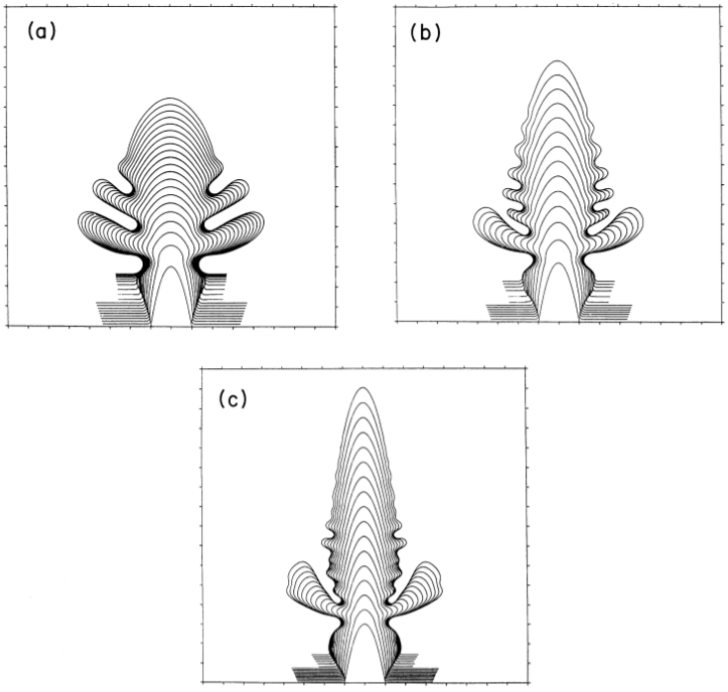

Figure 2.6: Different dendrites grow from a flat interface at $\Delta = 0.5$ and $\epsilon_4 =$ (a) 0.048, (b) 0.091, (c) 0.167. (adopted from Ref. [121])

2.4.5 Conclusions

In this section, we have described the Mullins-Sekeraka stability to explore the evolution of a planar interface with small perturbation. The main conclusion of the Mullins-Sekerka is that the positive change rate of pertubation amplitude, i.e. $\dot{\delta} > 0$, amplifies the pertubation of the planar interface, which leads to the dendrite formation, while the negative $\dot{\delta}$ weakens the the perturbation. The dendrite shapes can be calculated by using sharp interface methods in symmetric and one-sided cases, as described in Eqs. (2.85) and (2.96). For given undercooling and anisotropy, these integro-differential equations are implemented in Chapter 3 as Green's function calculations to predict the dendrite growth rates in symmetric and one-sided cases and the nondiagoanl phase field results are benchmarked with these predecitions. Furthermore, in the two-sided case, Barbieri-Langer theory gives an approximated relation to predict the dimensionless growth veolcities, which is used to benchmark the nondiagonal phase field simulation restuls in the two-sided case. We should note that the predictions of Barbieri-Langer theory in one-sided case is twice larger than that in the symmetric case, i.e., $\sigma^*(\mu = 0) = 2\sigma^*(\mu = 1)$, which agrees with the conclusions of Misbah [122].

2.5 Eutectic solidification

Eutectic growth patterns during solidification have been widely investigated in materials processing for a long time. During eutectic solidification of a binary alloy, two solid phases (α and β) cooperatively grow from the parent phase with a wide variety of geometrical arrangements. In general, regular eutectic microstructures, such as rod and lamellar structures, form for low entropy of fusion of α and β phase, while

the irregular eutectic microstructures form for high entropy of fusion of β phase. Regular and irregular eutectic microstructures are shown in Fig. 2.7.

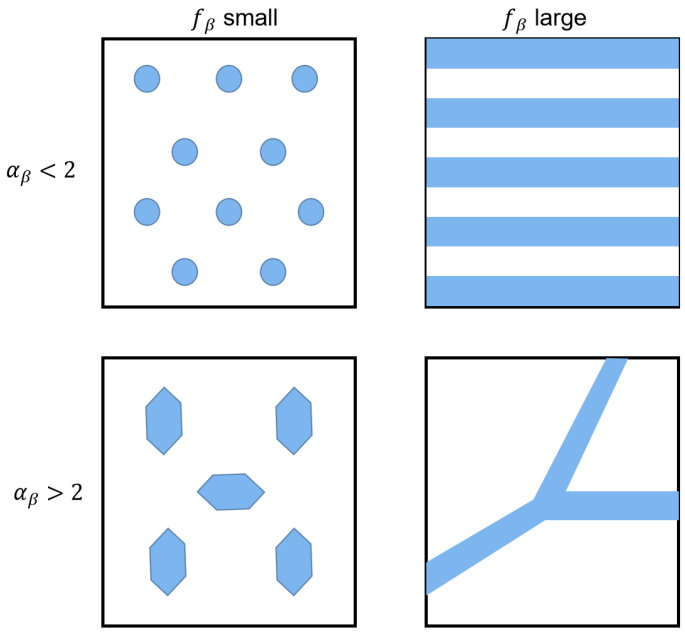

Figure 2.7: Demonstration of the regular and irregular eutectic microstructure for different fraction f_β and entropy of fusion α_β of β phase. (adopted from Ref. [125])

2.5.1 Jackson-Hunt theory

An assumed eutectic phase diagram is presented in Fig. 2.8. For two solid phases with isotropic and non-faceted solid-liquid interfaces, the free boundary problem include: (1) the bulk diffusion in the liquid phase and the mass conservation at solid-liquid interface (Stefan condition); (2) the local equilibrium at the interfaces (Gibbs-Thomson equation); (3) mechanical balance at the triple-junction (Young's law). The pioneering theory was presented by Zener [126] and Brandt [127] to predict lamellar growth. The predicted growth rate (v) at a specific undercooling (ΔT) is dependent on the lamellar spacing (λ), more precisely, the product of growth rate and the square of the lamellar spacing is constant, i.e. $v\lambda^2 = const.$ Based on Zener's work, Hillert took into account the surface energy and found a solution to the diffusion equation by assuming the solidification front to be flat [128]. Analogously, Jackson and Hunt solved the diffusion equation and for a given lamellar spacing, the relation between growth rate and undercooling is [129]

$$\frac{\Delta T}{m} = v\lambda Q^L + \frac{a^L}{\lambda}, \tag{2.100}$$

where m, Q^L and a^L are

$$\frac{1}{m} = \frac{1}{m_\alpha^L} + \frac{1}{m_\beta^L} \tag{2.101}$$

$$Q^L = \frac{P(1+\eta)^2 \Delta C}{\eta D}, \tag{2.102}$$

$$a^L = 2(1+\eta)\left(\frac{a_\alpha^L}{m_\alpha} + \frac{a_\beta^L}{m_\beta}\right), \tag{2.103}$$

where m_α^L and m_β^L are the slopes of liquidus and solidus. P depends on the ratio of lamellar spacings $\eta = \lambda_\alpha/\lambda_\beta$, which is defined as $P = \sum_{n=1}^{\infty}(\frac{1}{n\pi})^3 \sin^2(\frac{n\pi\lambda_\alpha}{\lambda_\alpha+\lambda_\beta})$. ΔC is the difference of concentrations between C_α and C_β, i.e. $\Delta C = C_\beta - C_\alpha$. D is the diffusivity in the liquid phase. a_α^L and a_β^L are determined by interface energy and contact angle, which read as $a_\alpha^L = (T_E/L_\alpha)\sigma_\alpha^L \sin\theta_\alpha^L$ and $a_\beta^L = (T_E/L_\beta)\sigma_\beta^L \sin\theta_\beta^L$, with T_E being the eutectic temperature, $L_{(\alpha/\beta)}$, $\sigma_{(\alpha/\beta)}^L$ and $\theta_{(\alpha/\beta)}^L$ being the latent heat, interface energy and contact angle of α or β phase, respectively. According to the Jackson-Hunt theory, the undercooling of the solidification front exhibits a minimum in directional solidification, whereas the growth velocity of the solidification front has a maximum in isothermal solidification.

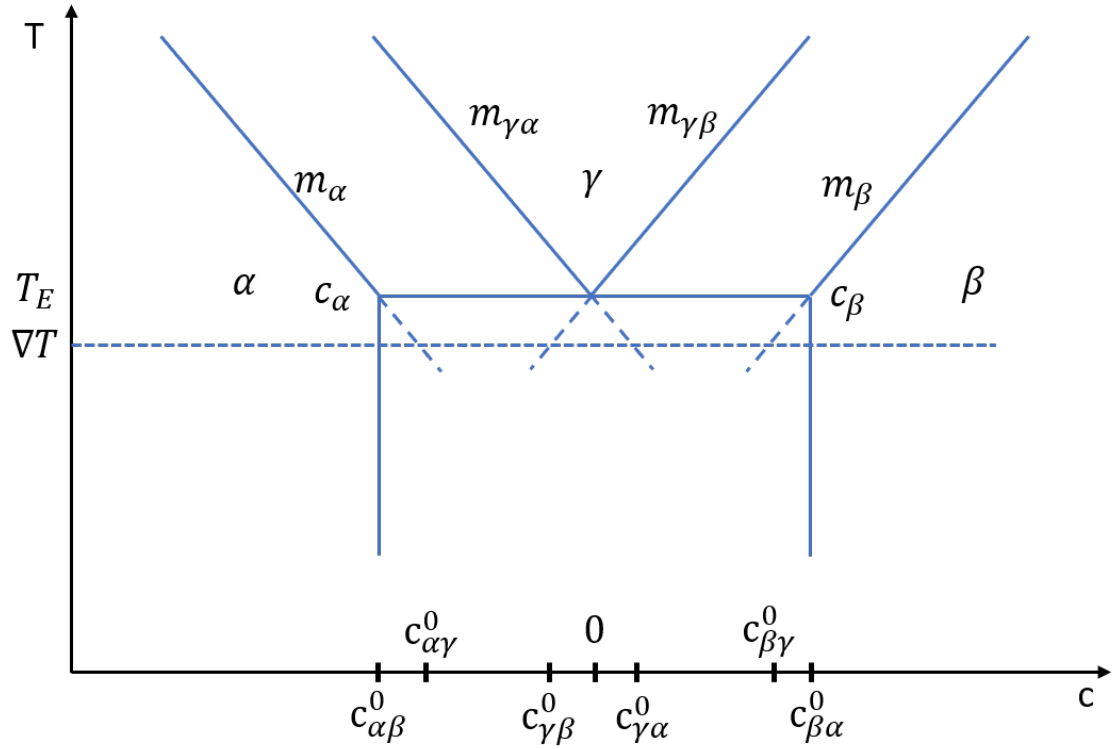

Figure 2.8: Illustration of a symmetric eutectic phase diagram.

Moreover, α/liquid , β/liquid and α/β interfaces are connected by a point, which is known as triple-junction. At local equilibrium, the balance of the interface energy at the triple-junction obeys Young's law, which reads

$$\sigma_\alpha^L \cos\theta_\alpha^L = \sigma_\beta^L \cos\theta_\beta^L, \tag{2.104}$$

$$\sigma_\alpha^\beta = \sin\theta_\alpha^L + \sigma_\beta^L \sin\theta_\beta^L, \tag{2.105}$$

Therefore, the Jackson-Hunt theory expresses the relation between growth velocity and undercooling during eutectic solidification. In spirit of the flat interface assumption in the Jackson-Hunt theory, the nondiagonal three-phase field simulation results are compared with the theoretical predictions during isothermal solidification and directional solidification in Chapter 4.

2.5.2 Phase-field simulations of eutectic solidification

In recent years, the phase field method has been widely used for investigating different eutectic growth patterns. For stable lamellar growth, Karma [130] presented a phase field model to describe the lamellar growth during binary alloy solidification. In the frame of the shape interface limit, the lamellar spacing needs to be much larger than the interface width. The steady state of the lamellar structure agrees well with the sharp interface calculations. Wheeler et. al. [131] proposed two kinds of phase field models. The first model is constructed based on a regular solution model with a chemical miscibility gap in absence of a solid-solid interface energy. The second one is thermodynamically consistent by using two order parameters to represent the different phases. The sharp interface asymptotic analysis is considered and the mechanical balance of the interface tensions is demonstrated. Drolet et. al [132] developed a phase field model to recover the characteristic features of the eutectic phase diagram and to reduce to the standard sharp interface formulation of non-equilibrium growth during direction solidification and isothermal solidification. Kim et al. [133] extended the interface field method and presented a phase field model with anisotropy under the condition of equal chemical potential difference. The phase field mobility and interface kinetices are derived based on the thin interface analysis. In the simulation results of $CBr_4 - C_2Cl_6$ organic alloy solidification, different lamellar growth patterns are reproduced, which is in good agreement with experimental observations. Apel et al. [134] performed 2D and 3D simulations to study a binary eutectic microstructures during directional solidification with an asymmetric phase diagram by ultilizing the multi-phase field model. The 2D simulation results demonstrate the stability of lamellar growth depending on the initialization of the nuclei, whereas the 3D simulations show the growth of fibrous structures, which are usually observed in experiments. Nestler et al. [135] developed a flexible phase field model and investigated competitive lamellar growth, which is consistent with the predictions of the Jackson-Hunt theory. Folch and Plapp [86] developed a quantitative phase field model with anti-trapping current in terms of a smooth free energy functional to eliminate additional third phases at a two phase interface. By applying the thin interface asymptotics, the free boundary conditions are fully reproduced. The simulation results of stable lamellar growth during directional solidification are consistent with the calculations of the boundary integral method and the Jackson-Hunt theory.

Except stable eutectic growth, the unstable eutectic structures are also studied by numerous investigations. Plapp and Karma [136] developed a phase field model of a binary eutectic with a dilute ternary impurity and investigated the nonlinear evolution of the interface of a eutectic colony, such as cell elimination and tip-splitting. Parisi and Plapp [137] investigated the morphological stability of lamellar eutectic growth by ultilizing a quantitative phase field model. The three dimensional simulation results show a zigzag instability appearing as the first instability, which is a transition from straight to chevron or wavy lamellar. Lahiri et al. [138] presented eutectic colonies with anisotropy as functions of pulling speed and imposed temperature gradient. In 2D simulations, the lamellar growth becomes more stable when the magnitude of anisotropy is increased, whereas, in 3D simulations, eutectic spirals appear and become tilted according to the orientations of the equilibrium interfaces. Hötzer et al. [139] produced helical eutectic spiral growth in 3D during directional solidification of ternary eutectics, which consists two rods rotating

around a second phase embedded in the matrix phase, and the non-equal interface energies are able to enhance the spiral growth. Choudhury et al. [140] extended the Jackson-Hunt theory to ternary eutectic alloys and derived the undercooling of the solidification front as a function of velocity and spacing. Phase field simulations demonstrate different instabilities for different lamellar spacings, which agree well with the analytical calculations.

2.6 Mechanisms of the pearlite transformation

In carbon steels, pearlite grains primarily nuclear on austenite grain boundaries and cooperatively grow into the parent austenite phase. During the transformation of pearlite, carbon must be transported from the ferrite phase to the neighbouring cemenite phase. In the literature, three possible diffusion paths for carbon transportation are investigated to explain the transformation kinetics of pearlite. The first diffusion path is the bulk diffusion, which is the diffusion in the austenite phase. The second one is the interface diffusion, while the last one is the volume diffusion, which indicates the diffusion in the ferritic phase.

2.6.1 Bulk diffusion

The Zener-Hillert theory explains the growth kinetics of the pearlite transformation under two assumptions [126, 141]. The first assumption is that the transportation of carbon only occurs in the parent austenite phase. The second one is that the interfaces of ferrite-austenite and cementite-austenite are flat. Therefore, for a given undercooling, lamellar spacing, the growth velocity of pearlite growth can be written as

$$v = \frac{2D_\gamma}{f^\alpha f^\theta}\left(\frac{c_e^{\gamma\alpha} - c_e^{\gamma\theta}}{c^{\theta\gamma} - c^{\alpha\gamma}}\right) \times \left(\frac{1}{\lambda}\right)\left(1 - \frac{\lambda_0}{\lambda}\right), \tag{2.106}$$

where D_γ is the diffusivity of carbon in γ phase. f^α and f^θ represent the volume fraction of ferrite and cementite phases. $c_e^{\gamma\alpha}$ and $c_e^{\gamma\theta}$ are the carbon concentrations in the austenite phase in front of the ferrite and cementite phases. $c^{\theta\gamma}$ and $c^{\alpha\gamma}$ represent the carbon concentration in austenite phase and in cementite at the eutectoid transformation interface. λ_0 indicates the lamellar spacing where all free energy is consumed to create the interface, i.e. $\lambda_0 = 2\sigma V_m/\Delta G$. Here, σ, V_m and ΔG are the interfacial energy, molar volume and change of total free energy, respectively. According to Eq. (2.106), the Zener-Hillert theory predicts that there is a manximum growth velocity during the pearlite growth, which is given by

$$\lambda_m^{Zener} = 2\lambda_0 = \frac{4\sigma V_m}{\Delta G}. \tag{2.107}$$

Kirkaldy proposed a criterion based on the maximum rate of entropy production [142], which reads

$$\lambda_m^{Kirkaldy} = 3\lambda_0 = \frac{6\sigma V_m}{\Delta G}. \tag{2.108}$$

However, there is still a discrepancy between the Zener-Hillert theory predicted kinetics of pearlite growth, defined as a bulk diffusion controlled mechanism, and experimentally observed pearlite growth velocities. Although Kirkaldy [142] and Ridley [143] re-evaluated the diffusivity of carbon in austenite and the discrepancy was

reduced by a factor 2-3, still a large discrepancy exists, which indicates the volume diffusion controlled mechanism are unable to fully explain the growth mechanism of the pearlite transformation.

2.6.2 Interface diffusion

To decrease the large discrepancy between the predicted growth velocities by using the Zener-Hillert model with the experimental observations, many researchers believe that alternate mechanisms exist to describe the carbon transfer during the pearlite transformation. Thus, interface diffusion becomes the most promising explanation, since the interfacial diffusivity is much larger than that in the bulk phase during solid-solid transformations. Earliest approximation to predict the growth velocity is by replacing the bulk diffusivity D_γ by interface diffusivity D_b with a ratio δ/λ, with δ being the interface width [144], which reads

$$v \approx \frac{2D_b\delta}{f^\alpha f^\theta \lambda}\left(\frac{c_e^{\gamma\alpha}-c_e^{\gamma\theta}}{c^{\theta\gamma}-c^{\alpha\gamma}}\right)\times\left(\frac{1}{\lambda}\right)\left(1-\frac{\lambda_0}{\lambda}\right). \tag{2.109}$$

Sunquist assumed that the interface diffusion is the dominant diffusion path of carbon transport and investigated the edgewise growth rate of pearlite with the consideration of capillary effects and imperfect carbon segregation [145]. Shapiro and Kirkaldy obtained an expression for the growth velocity of pearlite by assuming the free energy versus composition curves to be represented by parabolic expressions, which reads [142],

$$v = \frac{24\delta D_b}{\lambda^2}\frac{X_0^{\gamma\alpha-X_0^{\gamma\theta}}}{0.5-a}\left(1+\frac{2\sigma^{\alpha\theta}V}{\Delta F_0\lambda}\right), \tag{2.110}$$

where δ is the width of the boundary layer, $X_0^{\gamma\alpha}$, $X_0^{\gamma\theta}$ and a are equilibrium composition variables, $\sigma^{\alpha\theta}$ is the α/θ interface energy, ΔF_0 is the total free energy for the pearlite transformation. Then, the critical lamellar spacing S_c at which the growth velocity vanishes is

$$S_c = -\frac{2\sigma^{\alpha\theta}V}{\Delta F_0}. \tag{2.111}$$

Hillert pointed out the diffusion takes place through the cross section of the boundary rather than the edge and added a factor 2 in front of the interface diffusion contribution, which yields the expression of the growth velocity of pearlite [146]

$$v = \frac{8KD_b\delta}{f^\alpha f^\theta \lambda}\left(\frac{c_e^{\gamma\alpha}-c_e^{\gamma\theta}}{c^{\theta\gamma}-c^{\alpha\gamma}}\right)\times\left(\frac{1}{\lambda}\right)\left(1-\frac{\lambda_0}{\lambda}\right), \tag{2.112}$$

with K being the distribution coefficient for the alloy element between the boundary material and the parent phases.

Pandit et al. presented a model by combining the fluxes through the austenite phase and interface region [147], which leads to

$$v = \left(\frac{12D_b\delta}{\lambda}+2D_\gamma\right)\frac{1}{f^\alpha f^\theta}\left(\frac{c_e^{\gamma\alpha}-c_e^{\gamma\theta}}{c^{\theta\gamma}-c^{\alpha\gamma}}\right)\times\left(\frac{1}{\lambda}\right)\left(1-\frac{\lambda_0}{\lambda}\right). \tag{2.113}$$

Since D_γ is well estabilished, the only unknown is the interface diffusivity in Eq. (2.113), which is chosen as

$$D_b = 8.51\times10^{-5}\exp\left(-\frac{96851}{RT}\right)\mathrm{m^2s^{-1}}. \tag{2.114}$$

The activiation energy for the interface diffusion of carbon is less than that for bulk diffusion in austenite but larger than that for volume diffusion in ferrite.

Yamannaka et al. investigated the influence of interface diffusion of carbon on the growth kinetics during the pearlite transformation by using multi-phase-field simulations [148]. In their simulations, the interface diffusivities is chosen k ($k = 1, 2, 3, 4$) times larger than that of the γ phase. The simulation results indicate that the interface diffusion is able to significantly enhance the carbon diffusion from ferrite to cementite.

Yan et al. considered the formation of ferrite-cementite interfaces, bulk diffusion, interface diffusion and the solute drag effect and model the pearlite growth. This model predicts the growth rate, lamellar spacing and the partitioning of elements between ferrtie and cementite of pearlite [149].

2.6.3 Volume diffusion

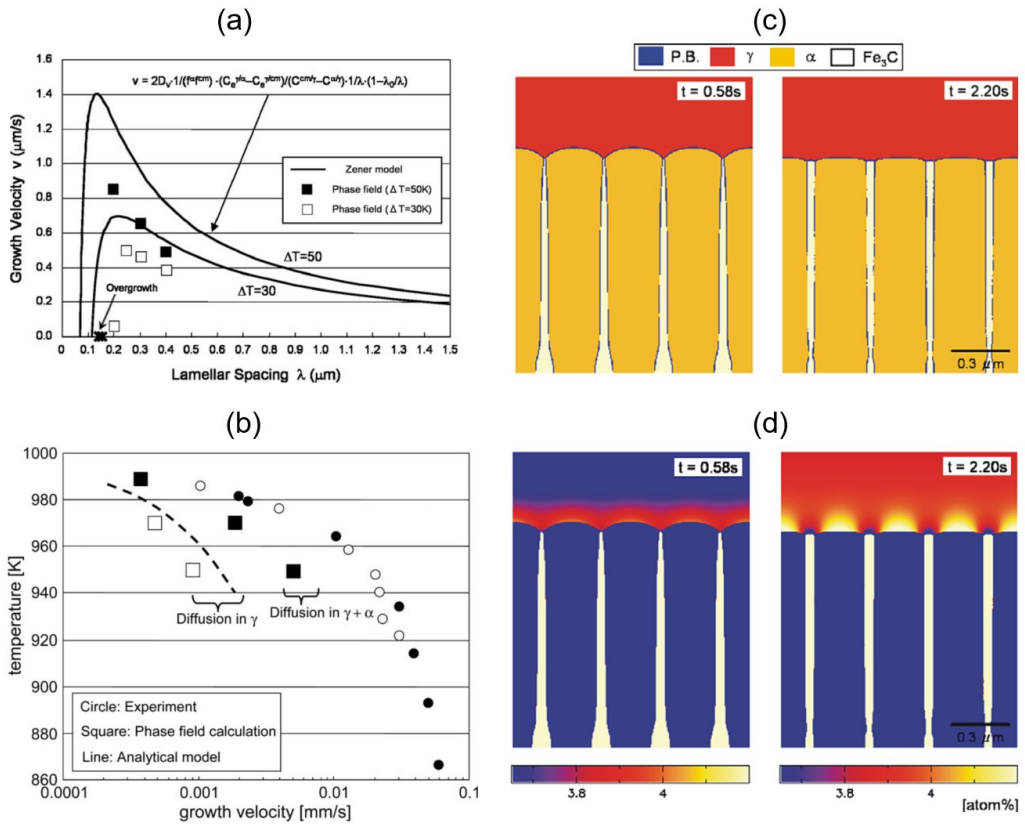

Figure 2.9: Demonstration of the multi-phase field simulation results during pearlite growth, which is taken from Ref. [150]. (a) The comparison between the simulation results and the Zener-Hillert predictions in one-sided case. (b) The comparison between simulation results and experimental observations with the consideration of diffusion in ferrite. (c-d) Morphology of pearlite at steady state, where (c) is the phase field and (d) is the concentration field. The left figures of (c) and (d) consider the diffusion in austenite and ferrite, while the right indicates the diffusion only exists in austenite.

Since the diffusivity ratio of D_α/D_γ is larger than 100, the carbon diffusion in the ferrite phase is not negligible. Nakajima et al. considered the carbon diffusion in the austenite and ferrite phase and obtained the growth velocities at different temperature by using the multi-phase-field method [150]. In their simulations, the α/γ and θ/γ interface mobilities are chosen much larger to reproduce the diffusion controlled manner. Their simulation results not only indicated the growth velocities of pearlite to be 4 times larger than the predictions of Zener-Hillert theory, but also showed the thickening of cemenite behind the transformation front, as shown in Fig. 2.9. Steinbach and Apel investigated the pearlite growth with the consideration of combining the influence of transformation strains present due to the concentration gradients in austenite and the diffusion in ferrite by using the multi-phase-field method [151]. According to their simulation results, the transformation strain restrains the cooperative growth mode of cementite and ferrite, which provokes the salient growth of cementite needles ahead of the ferrite front. Ankit et al. extended the Jackson-Hunt theory to eutectoid transformation by considering the diffusion in the parent and growing phases and the expression reads [152]

$$v = \rho v_{JH}, \tag{2.115}$$

with

$$\rho = 1 + t_\alpha \mu_\alpha \eta_\alpha + t_\theta \mu_\theta \eta_\theta, \tag{2.116}$$

where $\mu_\alpha = D_\alpha/D_\gamma$ and $\mu_\beta = D_\beta/D_\gamma$. η_α and η_θ are the equilibrium volume fractions of phases α and θ, respectively. t_α and t_θ are constants depending on the ratio of the liquidus slopes to the solidus slopes of α and θ phases. Phase field simulations were performed to compare with the predictions of the extended Jackson-Hunt theory. Moreover, the tapered cementite was also found in the simulation results.

In summary, we have introduced different diffusion paths to predict the kinetics of pearlite growth, including bulk diffusion, interface diffusion and volume diffusion. The pioneering work of bulk diffusion mechanism was the Zener-Hillert theory, however, whose predictions lead to a large discrepancy with the experimental observations. To narrow the difference, an interface diffusion mechanism is proposed since the diffusivity along the interface is several orders of magnitude larger than that in the austenite phase. Through evaluating the interface energy, interface diffusivity and the interface width, the calculated growth velocities agree well with the experimental results [147]. For phase field simulations, the bulk and volume diffusion are considered as the dominant mechanisms while the interface diffusion was not quantitatively integrated in these investigations [148, 150–152]. Therefore, in Chapter 5, we investigate the pearlite growth through considering the diffusion along the interface by using the developed grand potential based nondiagonal phase field model and compare with the corresponding analytic theories and the experimental results.

2.7 GPU programming

Nowadays, GPU (Graphics Processing Unit) programming is widely used to accelerate video, digital image, audio signal processing, statistical physics, scientific computing, medical imaging, neural networks, deep learning and intrusion detection. The general purpose of computing on GPUs is trying to accelerate the computational efficiency through integrating the GPU and CPU together. The attractive

advantages of GPUs are hiding latencies, maximising throughput, exploiting parallelism and saving energy. In addition, there are a few programming languages and standards used to program GPUs, such as CUDA (Compute Unified Device Architecture) and OpenCL (Open Computing Language).

CUDA was created by Nvidia in 2007 as parallel computing platform and application programming interface model to provide access for users to the GPU's virtual instruction set and parallel computational elements, which is used for GPU programming in this thesis. Compared with traditional GPGPUs (general-purpose computation on GPUs), CUDA has following advantages [153–155]:

- Unified memory (in CUDA 6.0 or later) and unified virtual memory (in CUDA 4.0 or later).
- Shared memory—provides a faster area of shared memory for CUDA threads. It can be used as a caching mechanism, and provides more bandwidth than texture lookups.
- Scattered reads: code can be read from any address in memory.
- Improved performance on downloads and reads, which works well from the GPU and to the GPU.
- Full support for integer and bitwise operations, including integer texture lookups.

2.7.1 GPU implementation

The presented phase field simulation results in this thesis have been accelerated by GPUs. The GPU implementation is a flexible tool to solve the forward Euler-type finite difference method and able to significantly accelerate the calculation for partial differential equations with low costs even on a single GPU. Initially, the simulation domain of dimensions $nx \times ny \times nz$ is divided into $L \times M \times N$ three dimensional blocks of equal size. Each block contains $MX \times MY \times MZ = (nx/L) \times (ny/M) \times (nz/N)$ threads, which is demonstrated in Fig. 2.10. By adjusting the best values of MX, MY and MZ, the simulation runtime can be optimized. Moreover, during GPU accelerated phase field simulations, the key point for improving the acceleration performance is that the phase field and chemical potential field evolution codes have to be incorporated entirely on the GPU to avoid unnecessary data transfer between GPU and CPU. In addition, the entire integration step in time is split into different kernels to ensure synchronisation of the parallel executions and to avoid race conditions. For instance, the correct calculation sequence is to complete the phase field evolution before updating the chemical potential evolution in a separate kernels, and afterwards, the boundary conditions should be implemented in another kernel.

2.7.2 Application of GPU acceleration in phase field simulations

Due to the aforementioned advantages of GPU programming, phase field simulations accelerated by GPUs are able to simulate real-time, quantitative and large scaled three-dimensional microstructure evolution processes.

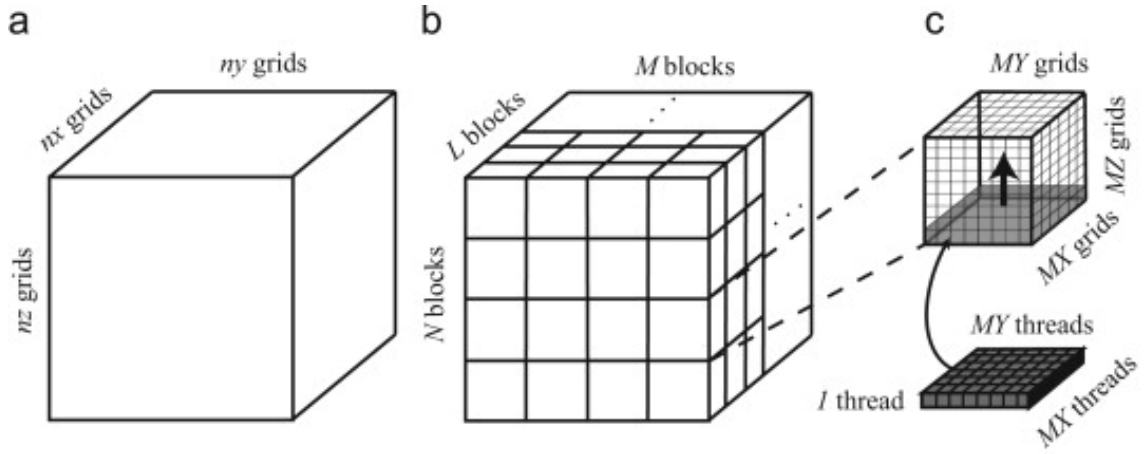

Figure 2.10: Demonstration of blocks and threads. (a) The simulation domain contains $nx \times ny \times nz$ grids. (b) The simulation domain is subdivided into $M \times N \times L$ blocks. (c) Each block contains $MX \times MY \times MZ$ threads. (This figure is taken from Ref. [156].)

In 2011, Yamanaka et al. developed a GPU acceleration code and presented GPU accelerated phase field simulations for dendrite growth during isothermal solidification. The performance test demonstrated the feasibility of the GPU acceleration method and the GPU calculations with shared memory reach 170 GFLOPS [156]. Aoki et al. developed multi-GPU codes for the dendritic solidification process, which demonstrates that the multi-GPU computing has a large communication overhead [157]. In 2012, Yamanaka et al. performed GPU accelerated multi-phase field simulations to investigate the austenite to ferrite transformation in a steel and compared the computing time between GPU and CPU. The comparison indicates the GPU acceleration is able to speed up the computing time by 5 - 15 times [158]. In 2013, Takaki et al. investigated dendrite growth patterns during directional solidification by using GPU accelerated very-large-scale phase field simulations. It was found that relatively larger amount of dendrites with unfavorable orientation can survive unexpectedly [159]. In 2013, Schlüter et al. developed a GPU-accelerated finite element implementation of a phase field model for dynamic brittle fracture [160]. In 2014, Takaki et al. investigated the competitive growth of dendrites with favorable and unfavorable orientation during directional solidification by using multi-GPU acceleration [161]. In 2015, Takaki et al. developed a GPU acceleration code for a phase field lattice Boltzmann method by using a single NIVDIA Tesla K20X, which is capable to carry out the simulations for dendritic growth with translation and rotation [162]. Sakane et al. developed a multi-GPUs acceleration code for three-dimensional phase field simulations during directional solidification with a moving frame method. The simulation results demonstrated the competitive behavior during the dendritic growth within a reasonable computational time [163]. Tourret and Karma developed a multi-GPUs accelerated quantitative phase field model for directional solidification. The computing time accelerated by multi-GPUs is about 150 times faster than the phase field calculation on a single core CPU [164]. Rojas et al. presented GPU accelerated phase field simulations combined with lattice Boltzmann methods to investigate the effects of melt convection and solid motion

on dendrite growth [165]. Shibuta et al. revealed the evolution of the homogeneous nucleation behavior in an undercooled melt by using million-atom molecular dynamics and subsequent dendrite growth in a large scale simulation domain with dimensions of $3.072 \times 3.072 \times 3.072$ mm^3 accelerated by 768 GPUs [166]. Up to now, the parallel architecture of GPUs becomes a more and more straightforward, flexible and efficient acceleration technology to speed up phase field simulations.

Chapter 3

Dendritic growth

The content of this chapter is published in Ref. [167].

The phase field (PF) method has emerged in the last thirty years as one of the most powerful tool to tackle free boundary problems in various fields. While in free boundary problems, different bulk domains where transport equations hold are separated by interfaces with boundary conditions, the PF models describe continuous fields obeying the same evolution equations everywhere in space, with the spatial variations of the so-called phase field (nothing but an order parameter) representing the interfaces. The latter thus possesses a certain width which is a numerical parameter that has no physical meaning. In order to simulate extended systems, the interface width needs to be chosen orders of magnitude larger than the physical width of the interface (of the order of the atomic distance). Since, of course, the fields dynamics are influenced by the interface width, special care thus has to be taken in order for the PF model to reproduce a desired free boundary problem.

In Ref. [84], an asymptotic analysis linking the classical PF model (model C in the Hohenberg-Halperin nomenclature [14]) and the free boundary problem was introduced and named *thin-interface limit*. On the one hand, the thin-interface analysis provides the influence of the parameters of the PF model on the conservation equation at the moving interface (Stefan condition). On the other hand, it provides the link with the kinetic coefficients describing the deviation from local equilibrium at the interface. In particular, the thin-interface analysis allows one to choose the PF model parameters so as to reproduce local equilibrium boundary conditions that are relevant to usual solidification experiments as well as industrial processes such as casting.

While designed for a transformation driven by heat diffusion in a pure material with equal diffusivity in both phases (symmetric model), the thin-interface limit was later on performed in the case of alloys with a vanishing diffusivity in the growing solid phase (one-sided model) [85]. Equilibrium boundary conditions were then shown to require the addition of a so-called *anti-trapping current* in the equation for the alloy concentration. However, in the general case where the diffusivity of the growing phase D_S neither equals the one of the disappearing phase D_L nor vanishes, the thin-interface analysis of the classical PF model shows that equilibrium boundary conditions may not be achieved without altering the thermodynamics of the interface with some unphysical adsorption [99]. Only recently, this problem has been solved by the introduction of the kinetic cross-coupling between the phase field and the diffusion field [107, 109]. In the constitutive force-flux relations of

the PF model, cross terms are then present, and are parametrized by the same new parameter according to Onsager's symmetry. This new parameter provides the additional degree of freedom to achieve equilibrium boundary conditions at the interface. We note that this cross terms have been shown to be also responsible for the Ehrlich-Schwoebel effect in the non-diagonal PF model for molecular-beam-epitaxy [108].

3.1 Non-diagonal phase field model

In this section, we present the nondiagonal phase field model with the consideration of anisotropy for dendrite growth. In two dimensions, the normal direction $\mathbf{n}$ to the interface is a function of the space coordinates x and y, and only one parameter describes the anisotropy of interface energy. In terms of the PF model, this anisotropy enters the interface width through the partial derivatives of the phase field $\phi(x, y)$ [84]:

$$W(\mathbf{n}) = W_0(1-3\epsilon)\left[1 + \frac{4\epsilon}{1-3\epsilon}\frac{(\partial_x\phi)^4 + (\partial_y\phi)^4}{|\boldsymbol{\nabla}\phi|^4}\right].$$

ϵ represents the strength of the four-fold anisotropy and W_0 indicates the average value of the interface width.

Then, the nondiagonal phase field evolution equations in Ref. [109] is rewritten as

$$\begin{aligned}\mathcal{D}\mathrm{et}(\mathbf{n})\tau(\mathbf{n})\dot{\phi} = H\Big\{&\phi(1-\phi^2) + \boldsymbol{\nabla}\cdot\left[W^2(\mathbf{n})\boldsymbol{\nabla}\phi\right] \\ &+\partial_x\left(|\boldsymbol{\nabla}\phi|^2 W(\mathbf{n})\frac{\partial W(\mathbf{n})}{\partial(\partial_x\phi)}\right) \\ &+\partial_y\left(|\boldsymbol{\nabla}\phi|^2 W(\mathbf{n})\frac{\partial W(\mathbf{n})}{\partial(\partial_y\phi)}\right)\Big\} \\ &-\frac{p'(\phi)}{2}u + M(\mathbf{n})W(\mathbf{n})D(\phi)\boldsymbol{\nabla}\phi\cdot\boldsymbol{\nabla}u \end{aligned} \tag{3.1}$$

and the second equation for the diffusion field u reads

$$\dot{u} = \boldsymbol{\nabla}\cdot\left\{D(\phi)[\boldsymbol{\nabla}u + M(\mathbf{n})W(\mathbf{n})\dot{\phi}\boldsymbol{\nabla}\phi]\right\} + \frac{p'(\phi)}{2}\dot{\phi}. \tag{3.2}$$

For a pure material, $u = (T - T_M)c_P/L$ measures the deviation of the temperature T from the melting temperature T_M, with c_P and L being the specific heat and latent heat, respectively. Similarly, for the solidification of a binary alloy at a given temperature, $u = (C - C_L)/(C_S - C_L)$ measures the deviation of the concentration C from the liquidus concentration C_L, with C_S being the solidus concentration. On the right hand side of Eq. (3.1), the term parametrized by the dimensionless parameter H comes from the ϕ-dependence of the thermodynamics of the system. The first term is inherited from the double well potential, with minima at $\phi = \pm 1$ and a maximum at $\phi = 0$, while the second, third and fourth terms represent the $\mathbf{n}$-dependent penalization of ϕ variations. Here, in comparison to Refs. [109, 110], the relaxation time τ, the cross-coupling parameter M and, as a consequence, the determinant (that has to be positive) $\mathcal{D}\mathrm{et} = 1-(MW\boldsymbol{\nabla}\phi)^2 D(\phi)/\tau$, have an explicit

dependence on the orientation of the interface. This dependence is related to the choice of interface conditions that we aim to reproduce with the PF model, whose dynamics is highly influenced by W as mentioned in the introduction. Our model is called non-diagonal owing to the existence of the terms parametrized by M. In opposition, for a diagonal model, one has $M = 0$. These additional contributions appear as a consequence of non-diagonal terms in the force-flux Onsager relations describing the dynamics of the system. They yield a kinetic cross-coupling between the non-conserved field ϕ and the conserved field u. The Onsager relations give the proportionality between two fluxes (flux of heat and flux of matter across the interface for the thermal model, diffusion flux and interface velocity for the alloy model) and two driving forces (temperature gradient and jump of free energy at the interface for the thermal model, gradient of diffusion chemical potential and jump of grand potential for the alloy model) [108]. Only one of the two fluxes exists in the bulk, but both exist at the interface, leading to a 2×2 matrix of interface kinetic coefficients. As will be shown explicitly later, a finite value of M is necessary to reproduce equilibrium conditions at the interface when the diffusion coefficients are finite in both phases and different. One should note that, when the diffusion flux vanishes in the bulk solid (one-sided case with $D_S/D_L = 0$), the Onsager symmetry may not be invoked because the two fluxes at the interface are not linearly independent. This gives the possibility to introduce the term parametrized by M only in Eq. (3.2), presented as an anti-trapping term by Karma [85].

At equilibrium ($u = 0$), the one-dimensional phase field profile reads $\phi_{\rm eq}(x) = -\phi_{\rm eq}(-x) = \tanh(x/\sqrt{2}W)$. In the following, we assign the equilibrium value $\phi = 1$ to the growing phase (solid phase) and $\phi = -1$ to the disappearing phase (liquid phase). Within this frame the orientation dependent capillary length, reflecting the orientation dependence of interface energy, is $d(\mathbf{n}) = \alpha H W(\mathbf{n})$ where $\alpha = W\int_{-\infty}^{\infty} {\rm d}x[\phi'_{\rm eq}(x)]^2 = 2\sqrt{2}/3$ is independent of $\mathbf{n}$. For a pure material, the function $p(\phi)$ interpolates between the values at the melting temperature of the solid and liquid entropies [109]. For a binary alloy, $p(\phi)$ interpolates between the equilibrium values of the concentration field [108]. We choose an odd function $p(\phi) = -p(-\phi) = 15(\phi - 2\phi^3/3 + \phi^5/5)/8$ for which $p(\phi = \pm 1) = \pm 1$. The oddness of $p(\phi)$ ensures the absence of undesired adsorption effects at the interface.

The diffusivity is phase-dependent (D_S in solid and D_L in liquid) through its ϕ-dependence. It has been shown [109] that in order to reproduce equilibrium boundary conditions at the interface, one may use a diffusivity that reads

$$\frac{1}{D(\phi)} = \left(\frac{1}{2D_S} + \frac{1}{2D_L}\right) + g(\phi)\left(\frac{1}{2D_S} - \frac{1}{2D_L}\right) \tag{3.3}$$

where the odd function $g(\phi) = -g(-\phi)$ also obeys $g(\pm 1) = \pm 1$. In addition, in order not to alter the heat/mass conservation equation at the moving interface with a surface diffusion flux, $g(\phi)$ should incorporate some contribution parametrized by a coefficient a that depends on $\mu = D_S/D_L$, and chosen such that $\int_{-\infty}^{\infty} {\rm d}x\{D[\phi_{\rm eq}(x)] - D_S/2 - D_L/2\} = 0$ [99]. As in Ref. [110], we choose a function g of the form $g(\phi) = \phi[1 + a(1 - \phi^2)]$. Then for each μ, one should find the coefficient a^* such that the above-mentioned integral vanishes.

In order to achieve equilibrium boundary conditions, the relaxation time and the

cross-coupling coefficient read

$$\tau(\mathbf{n}) = \frac{\beta W^2(\mathbf{n})}{4\alpha}\left(\frac{1}{2D_S} + \frac{1}{2D_L}\right), \tag{3.4}$$

$$M(\mathbf{n}) = \frac{\chi W(\mathbf{n})}{2\alpha}\left(\frac{1}{2D_S} - \frac{1}{2D_L}\right), \tag{3.5}$$

where $\beta = \int_{-\infty}^{\infty}(\mathrm{d}x/W)\{1 - p^2[\phi_{\mathrm{eq}}(x)]\} \simeq 1.40748$ and $\chi = \int_{-\infty}^{\infty}(\mathrm{d}x/W)\{1 - p[\phi_{\mathrm{eq}}(x)]g[\phi_{\mathrm{eq}}(x)]\}$. Here, we note the necessity of introducing a non-diagonal model in order to simulate $D_S \neq D_L$ with D_S and D_L being finite, while a diagonal model with $M = 0$ is sufficient when $D_S = D_L$. Since $g(\phi)$ varies with μ through the variation of a^*, the value of χ also depends on μ. In Fig. 3.1, we present a^* and χ in the range of μ that the present model allows to investigate. Indeed, due to the condition of positiveness of the determinant $\mathcal{D}\mathrm{et}$, we have an upper bound for the absolute value of M, that in turns sets lower bound to the ratio μ (here close to 0.06) for which we are able to achieve equilibrium boundary condition and elimination of surface diffusion [109, 110]. It is also important to notice that a^* and χ obey $a^*(\mu) = a^*(1/\mu)$ and $\chi(\mu) = \chi(1/\mu)$.

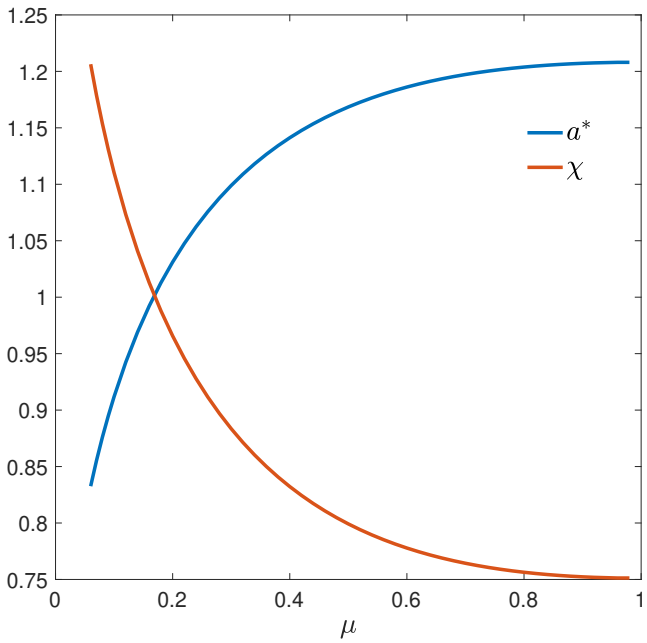

Figure 3.1: Selected value a^* of the parameter a in the function $g(\phi)$ such that surface diffusion is eliminated, and corresponding value of χ.

As mentioned in the introduction, we are also interested in the one-sided case where $\mu = 0$. Then, one has to use another definition of the diffusivity than Eq. (3.3). Instead, we write

$$D(\phi) = D_{\mathrm{os}}(\phi) = D_L(1 - \phi)/2. \tag{3.6}$$

In Ref. [108], the equilibrium boundary conditions have been reproduced when (please pay attention to the fact that in Ref. [108], a double well potential is used

to yield equilibrium values for the phase field $\phi = 1$ and $\phi = 0$)

$$M(\mathbf{n}) = M_{os}(\mathbf{n}) = \frac{\zeta W(\mathbf{n})}{2\alpha D_L}, \tag{3.7}$$

$$\tau(\mathbf{n}) = \tau_{os}(\mathbf{n}) = \frac{\lambda W^2(\mathbf{n})}{4\alpha D_L}, \tag{3.8}$$

where $\zeta = \int_{-\infty}^{\infty}(\mathrm{d}x/W)\{1 + \phi_{eq}(x) - 2p[\phi_{eq}(x)]\}/[1 - \phi_{eq}(x)] \simeq 2.12132$ and $\lambda = 2\int_{-\infty}^{\infty}(\mathrm{d}x/W)\{1 - p^2[\phi_{eq}(x)]\}/[1 - \phi_{eq}(x)] \simeq 3.42778$. Here, we note that surface diffusion is suppressed with the choice in Eq. (3.6) since $\int_{-\infty}^{\infty}\mathrm{d}x\{D_{os}[\phi_{eq}(x)] - D_L/2\} = 0$.

3.2 Boundary integral equations

As mentioned in the introduction, we also have performed boundary integral calculations for benchmarking. The boundary integral technique consists of writing an integro-differential equation for the steady state of interface shape $y_{\mathrm{int}}(x)$. While for an arbitrary shape of the interface, the diffusion field is obtained through an integral over the interface of a kernel involving the Green's function of the diffusion equation, the solution $y_{\mathrm{int}}(x)$ is determined by imposing the value u_{int} of the diffusion field u at the interface, here with the Gibbs-Thomson local equilibrium condition,

$$u_{\mathrm{int}} = \Delta - d_0(1 - 15\epsilon\cos 4\theta)\kappa. \tag{3.9}$$

Δ represents the value of the dimensionless diffusion field at infinity ahead of the growing dendrite, d_0 represents the average value of the capillary length (related to the parameters of the phase field model through $d_0 = \alpha H W_0$), ϵ is the anisotropy parameter in Eq. (3.1), and $\kappa = -y''_{\mathrm{int}}/(1 + y'^2_{\mathrm{int}})^{3/2}$ is the curvature of the interface. Here, the factor 15 comes from the definition of the interface stiffness for a cubic crystal [119] where θ is the angle between the normal to the interface and the direction along which the growth is favored, i.e. the direction of minimum stiffness.

The detailed boundary integral methods can be referred to [121, 168] and references therein for additional information. We mention that, apart from the shape of the interface, the steady-state velocity V is found, using the Ivantsov relation $\Delta = \sqrt{\pi P}\exp(P)\mathrm{erfc}\sqrt{P}$ where $P = \rho V/(2D_L)$ with ρ being the radius of the Ivantsov parabola [169]. The boundary integral technique has, up to now, only been used for the symmetric model ($\mu = 1$) and for the one-sided model ($\mu = 0$). This is probably due to the fact that for other values of μ, the number of unknowns that have to be found is doubled. Indeed, in addition to the shape of the interface, the normal gradient of the diffusion field at the interface should be also found self-consistently. However, the boundary integral equation was analyzed by Barbieri and Langer in Ref. [124], and it was shown that, in the limit of small anisotropy (in addition to being in the limit of small driving force Δ as usual in theoretical descriptions of weakly out-of-equilibrium dendritic growth), i.e. when the correcting term to the capillary length parametrized by 15ϵ in Eq. (3.9) is small, the steady-state velocity depends on μ in the following way:

$$\frac{V(\mu = 1)}{V(\mu)} = \frac{1 + \mu}{2}. \tag{3.10}$$

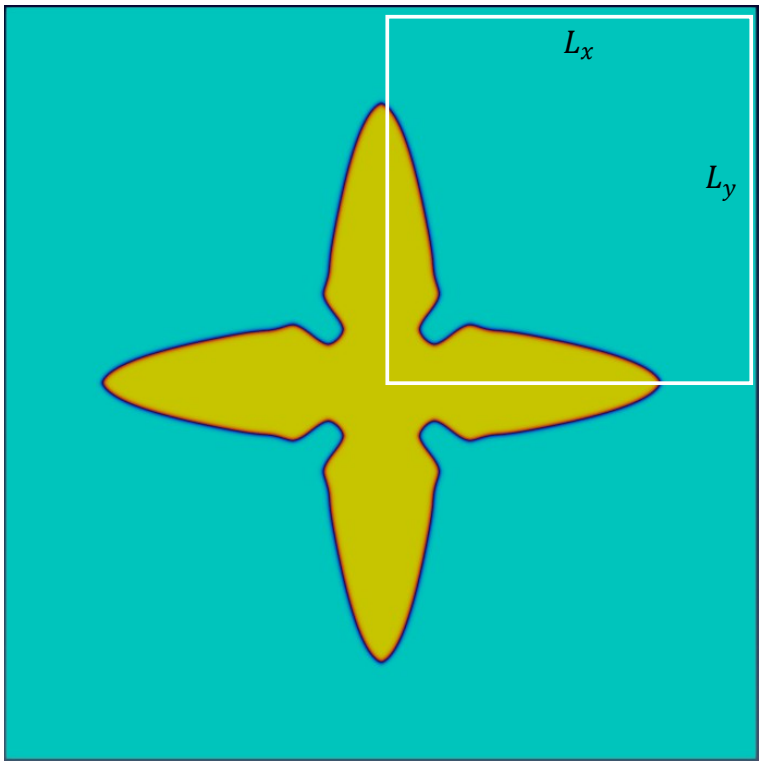

Figure 3.2: Demonstration of the simulation domain with the size $L_x \times L_y$ used for dendrite growth. 1/4 dendrite is simulated to save the computational time in the simulation domain.

3.3 Results and discussion

In this section, we present our results for an anisotropy strength $\epsilon = 0.04$. We benchmarked our non-diagonal PF model with Green's function (GF) calculations within the symmetric and one-sided models, for different values of the driving force Δ. The non-diagonal PF and chemical potential evolution equations presented in Eq. (3.1) and (3.2) were iteratively solved in a two-dimensional simulation domain with a uniform grid spacing $\Delta x = \Delta y = 0.4W_0$ by using an explicit finite-difference method. The sizes of the simulation domain were set to $L_x \times L_y = 768\Delta x \times 768\Delta y$ to $2048\Delta x \times 2048\Delta y$, as shown in Fig. 3.2. To save simulation time, only 1/4 dendrite was predefined at the left corner of the simulation domain with the far-field boundary condition $u \to \Delta$, and also a moving-frame method and GPU acceleration were employed in the present work. Furthermore, we note that for the symmetric model where $D_S/D_L = 1$, the diffusivity is a constant, the cross-coupling parameter M vanishes and the classical PF model is recovered. For the one-sided case where $D_S/D_L = 0$, the diffusivity is given by Eq. (3.6), and the phase field parameters are given by Eqs. (3.8) and (3.7).

In Table 3.1, we gather our PF and GF results. We see that the PF model reproduces the GF results within 5% error, which is quite satisfactory, and no particular trend arises concerning the dependence of the error on Δ. On the other hand, we may state that the deviation shows a tendency to be larger for $\mu = 0$ than for $\mu = 1$.

In the case $\epsilon = 0.04$, the correction to the capillary length in Eq. (3.9) is not much smaller than unity, and we see that the relation between the steady-state

Table 3.1: Dimensionless steady-state velocity from the phase fields simulations (V_{PF}) and from the Green's function calculations (V_{GF}). Here $\epsilon = 0.04$.

Δ	μ	$\frac{V_{\mathrm{PF}} d_0}{D_L}$	$\frac{V_{\mathrm{GF}} d_0}{D_L}$	Error(%)
0.65	1	0.0393	0.0399	1.5
	0	0.0573	0.0543	5.5
0.60	1	0.0238	0.0237	0.4
	0	0.0360	0.0344	4.7
0.55	1	0.0141	0.0139	1.4
	0	0.0219	0.0212	3.3
0.50	1	0.00817	0.00800	2.1
	0	0.0132	0.0126	4.8
0.45	1	0.00457	0.00443	3.2
	0	0.00744	0.00722	3.0

velocities for $\mu = 0$ and $\mu = 1$ does not follow Eq. (3.10). In Fig. 3.3, we present

$$\Omega = \frac{V(1)}{V(\mu)} \frac{2}{1+\mu} \tag{3.11}$$

as a function of μ for our phase field simulations (crosses), and for the analytical theory in Ref. [124] (horizontal black dashed line). The interface width for the phase field simulations is chosen such that the velocity has converged with respect to the increasing ratio d_0/W_0, and the latter ranges from $d_0/W_0 = 0.139$ for the smallest velocities to $d_0/W_0 = 0.554$ for the largest ones.

We see that, although our phase field simulations get closer to the analytical theory when Δ decreases, a large deviation remains, illustrating the breakdown of the assumptions made in Ref. [124]. Let us note that a relatively good agreement was found with the analytical theory for $\epsilon = 0.02$ and $\Delta = 0.55$ in Ref. [87]. However, the phase field model developed in this work, that was designed to account for diffusion in the growing phase, imposes an unjustified linear relationship between the fluxes at the interface and the interface velocity in addition to the conservation equation, and this model is therefore not consistent on the thermodynamic level.

Beyond reporting our phase field results for the μ-dependence of the dendrite tip steady-state velocity, we propose now a generalization of the relation (3.10). This generalization aims at expressing the μ-dependence of velocity for strengths of anisotropy for which the correction to the capillary length due to anisotropy in Eq. (3.9) is not small compared to unity, i.e. when $15\epsilon \simeq 1$. In view of the linear dependence of the ratio $V(\mu = 1)/V(\mu)$ in Eq. (3.10), we write:

$$\frac{V(1)}{V(\mu)} = \frac{V(1)}{V(0)} + \mu \left[1 - \frac{V(1)}{V(0)} \right]. \tag{3.12}$$

This expression depends, apart from μ, on the ratio $V(1)/V(0)$. This ratio, that equals $1/2$ when Eq. (3.10) is recovered at small enough ϵ, is estimated for $\epsilon = 0.04$ using the velocities $V_{\mathrm{GF}}(\mu = 1)$ and $V_{\mathrm{GF}}(\mu = 0)$ obtained with the Green's function

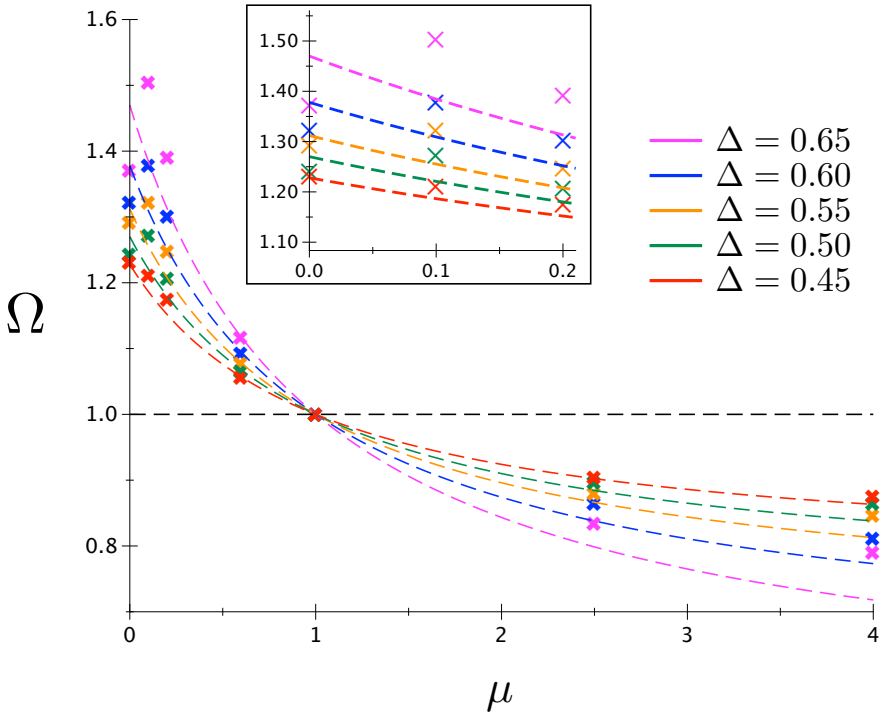

Figure 3.3: Crosses: rescaled ratio of velocities Ω (see Eq. (3.11) for definition) obtained from PF simulations as a function of μ, for different values of Δ; dashed colored lines: representation of Eq. (3.12) based on GF results for $\mu = 0$ and $\mu = 1$; black horizontal dashed line: Barbieri-Langer theory [124], i.e. Eq. (3.10).

calculations for the symmetric and the one-sided model reported in Table 3.1. In Fig. 3.3, Eq. (3.12) is then represented by the dashed colored lines, with each color corresponding to a different value of Δ. We clearly see that our phase field calculations converge to Eq. (3.12) when Δ decreases.

For $\Delta = 0.45$, the deviation between the PF results and Eq. (3.12) does not exceed 2%. When one additionally looks at the details of the curve in the neighborhood of $\mu = 0$ (in the inset), we observe that our PF results for $\Delta > 0.45$ exhibit an unexpected behavior. For $\mu = 0.1$ and 0.2, our PF results lie above Eq. (3.12), but they lie below for $\mu = 0$. We suspect that the form of the diffusivity function in Eq. (3.3), that involves the parameter a chosen such that surface diffusion is eliminated (let us note that other strategies have been used for such a purpose [170]), plays a role. Indeed, this function is non-monotonous and the magnitude of its variations, that are restricted to region of width W, increases when the deviation of μ from unity increases. In comparison, for $\mu = 0$, the diffusivity in Eq. (3.6) provides the elimination of surface diffusion while being monotonous. Anyway, the PF results for the smallest value of Δ suggest that this unexpected behavior disappears when Δ is small enough.

The quality and robustness of the PF results presented above are supported by two other sets of simulations. For that, we have investigated the behavior of the PF model in the range $0 < \mu < 1$ when: 1) the kinetic cross-coupling is turned off, i.e. when $M = 0$; 2) the procedure to eliminate surface diffusion is turned off, i.e. when $a = 0$. We present in Fig. 3.4 the results for $\Delta = 0.55$ and $\Delta = 0.45$, together with the corresponding results already shown in Fig. 3.3. Let us note that

the reference velocity $V(\mu = 1)$ is the same for case 1 ($M = 0$) and for case 2 ($a = 0$) because the diffusivity is a constant, i.e. $1/(2D_S) - 1/(2D_L) = 0$ in Eqs. (3.3) and (3.5). In both cases, we see that the results deviate from the PF results presented in Fig. 3.3. This deviation systematically increases when the deviation of μ from unity increases and when Δ increases. For example, for $\Delta = 0.45, \mu = 0.2$, this deviation approaches 20% when $M = 0$ and is larger than 10% when $a = 0$. These results therefore emphasize the necessity of using the non-diagonal PF model with elimination of surface diffusion. The usage of a non-diagonal Onsager matrix of forces-fluxes relations to eliminate of surface diffusion is, here, necessary in order to achieve a quantitative agreement with the GF calculations in which surface diffusion is not included. In general however, surface diffusion, in the sense of a tangential flux driven by variations of chemical potentials along the interface and leading to a normal motion of the latter (see Ref. [110] for more details), is allowed and takes place. Nevertheless, in the limit of small undercooling where the interface radius of curvature is large compared to the capillary length, the effect of surface diffusion is expected to be weak owing to the high order of the spatial derivatives that are involved in its description. The elimination of surface diffusion in the phase field model, through the choice of a vanishing surface diffusion coefficient, is thus mainly designed so as to suppress effects that are enhanced due to the diffuseness of the interface.

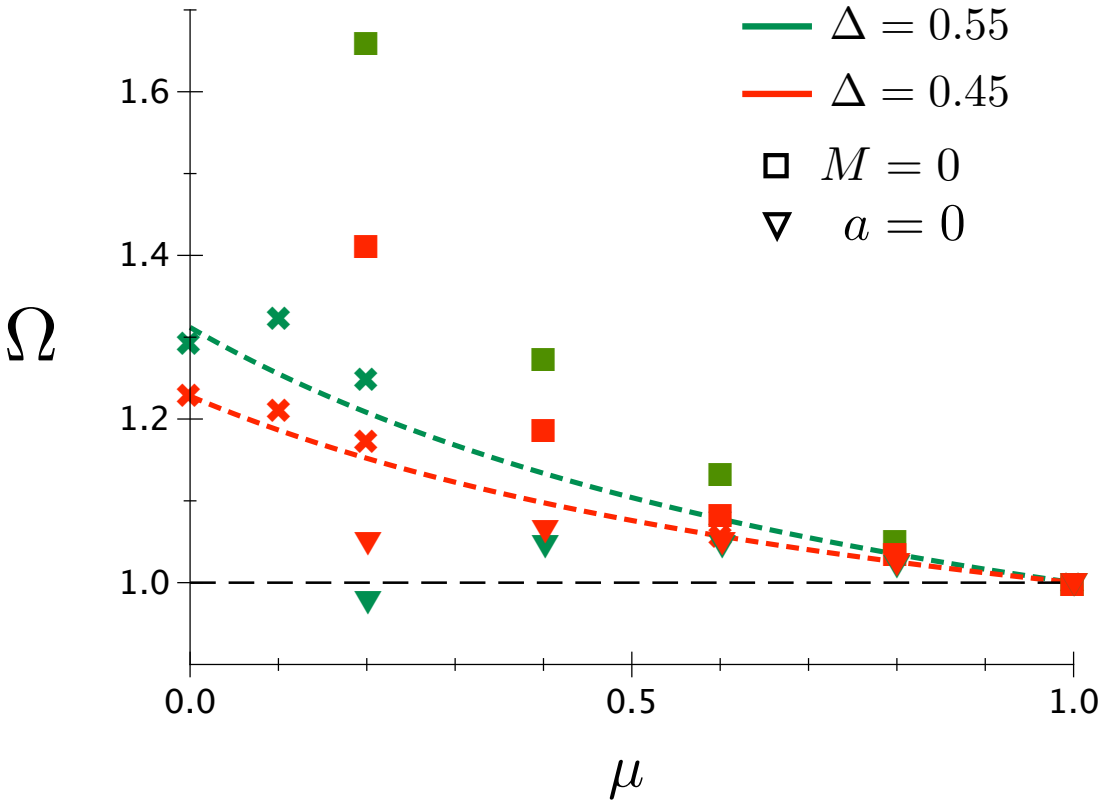

Figure 3.4: Comparison between the non-diagonal PF results presented in Fig. 3.3 (crosses) and PF simulations with: 1) squares: $M = 0$; 2) triangles: $a = 0$. We evidence here the importance of the kinetic cross-coupling and the elimination of surface diffusion.

We have also analyzed the dendrite tip region for $\Delta = 0.45, \epsilon = 0.04$. In Fig.

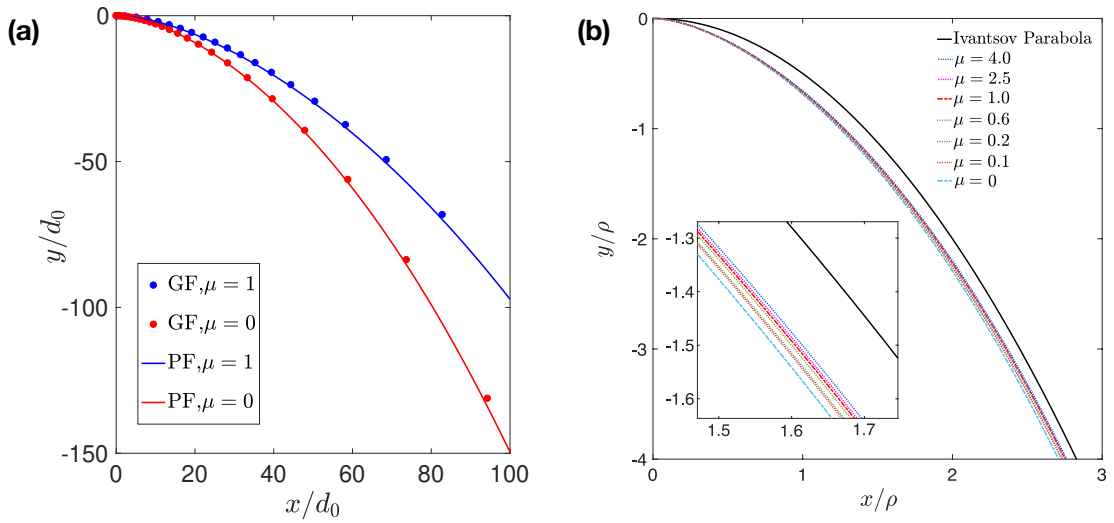

Figure 3.5: (a) Comparison of the steady-state dendritic shapes obtained from PF simulations and the GF results for $\Delta = 0.45$ and $\epsilon = 0.04$ in symmetric and one-sided cases. (b) Interface position in the dendrite tip ($x = 0$) region scaled by the Ivantsov radius ρ for different values of μ and at $\Delta = 0.45$ and $\epsilon = 0.04$. The tip radius is weakly depending on μ when expressed in units of ρ.

3.5a, we present the steady-state dendritic shape obtained from PF simulations and from GF calculations for the symmetric and the one-sided cases. As expected from the small deviations reported in Table 1, the dendrite shapes calculated by PF simulations in symmetric and one-sided cases agree perfectly with GF results. In Fig. 3.5b, we present the dendritic shape close to the tip together with the Ivantsov parabola, for the simulation data presented in Fig. 3.3. For each μ, we rescale the dendrite shape by ρ, the radius of the Ivantsov parabola. The latter is obtained by plugging the growth velocity V obtained from simulation into the inverse Ivantsov relation giving $P = \rho V/(2D_L)$ as a function of Δ. When we focus on a small region at a distance of approximately 1.5ρ behind the tip, we see that the scatter of the position of the interface is rather small compared to the distance to the Ivantsov parabola. In comparison, in a simulation with $\epsilon = 0.01$, the position of the interface is much closer to the Ivantsov parabola, which is in line with the classical dendritic theory for which the tip converges to the Ivantsov parabola when the anisotropy of interface energy decreases. We may thus conclude from our study that the tip radius depends only weakly on μ when expressed in units of ρ.

Let us finally give a short remark on the case of large deviations from equilibrium. The one-sided phase field model was recently investigated in the perspective of fast solidification [171], for which the boundary conditions for the chemical potentials jumps across the interface deviate from linear kinetics. Such an investigation would be valuable for the present model with diffusion in both phases. However, one should have in mind that our problem here is more complex that in the one-sided case. Indeed, in the latter, the absence of diffusion flux in the growing solid phase provides a constraint that is not present here (see the introduction in Ref. [109] for a more detailed discussion).

3.4 Summary

In this chapter, we have studied the capabilities of the non-diagonal phase field model for the simulation of two-dimensional dendritic growth in the case where the diffusivity in the growing phase D_S neither vanishes nor equals the one of the disappearing phase D_L. While we have benchmarked our PF results with Green's function calculations (sharp-interface model) for $\mu = D_S/D_L = 0$ and $\mu = 1$, our calculations for other values of μ show significant deviations from the theory by Barbieri and Langer [124], in accordance with the expected breakdown of their assumptions for the strength of interface energy anisotropy that we have used in our simulations. In view of our results we then propose a generalization of the prediction. We also have shown that an agreement between the PF model and GF method requires the kinetic cross-coupling and the elimination of surface diffusion. Our work opens up the way for quantitative phase field simulations of phase transformations where diffusion in the growing phases plays an important role in the pattern and velocity selections.

Especially, assuming $D_S \neq 0$ and $D_S \neq D_L$ is adapted to the solidification and melting in pure materials, but also in interstitial alloys. The most obvious illustration for the latter case is given by the dendritic solidification of the δ-ferrite in steels (see for example the recent reference [172]), for which the diffusion coefficient of interstitial carbon is comparable to the diffusion coefficient of carbon in the liquid phase. At lower temperature, the diffusion of carbon in the δ-ferrite drives the peritectic transformation, for which the austenite grows at the expense of the δ-ferrite. For such a transformation, a phase field model with a finite contrast of diffusion coefficient such as the one studied in this article should be used. More generally, at temperatures well below the melting temperature, alloys usually present regions in their phase diagram where several solid phases coexist, and solid-state transformations such as eutectoid ones involve diffusion in all phases. In particular, it was shown that diffusion in the growing phases may have a significant influence on the eutectoid transformation velocity in the case where all diffusion coefficients are equal [152]. Our model thus provides the possibility to study such dependence in general cases with generically different non-vanishing diffusion coefficients.

Chapter 4

Eutectic and Eutectoid transformations

The content of this chapter is published in Ref. [173].

The main purpose of this chapter is to extend the non-diagonal PF model to eutectic/eutectoid transformations in binary A-B alloys when the diffusivities in the growing phases are neither equal to the one in the mother phase nor negligible, to benchmark the quantitative capabilities of the extended non-diagonal PF model, and to better understand the role and effect of diffusion in the growing phases. Therefore, we first introduce the formulation of a non-diagonal three phase field model. Subsequently, we present the elimination of the abnormal effects at the α/γ, β/γ and α/β interfaces and the link to equilibrium boundary conditions. Following this, non-diagonal PF simulations are performed in the one-sided case to compare with boundary integral method calculations and Jackson-Hunt theory for a model alloy that is directionally solidified. Additionally, in the two-sided case, isothermal transformations at eutectoid and off-eutectoid composition are carried out and the growth velocities at steady state are compared to the extended Jackson-Hunt theory by Ankit *et al.* [152]. PF simulations without cross-coupling terms are also performed in order to evidence the necessity of using a non-diagonal PF model.

4.1 Phase-field model

In this section, we present the non-diagonal three phase field model by defining three scalar phase-field order parameters ϕ_i ($i = \alpha, \beta, \gamma$), to distinguish the different phases α, β and γ, obeying the constraint

$$\sum_{i=\alpha,\beta,\gamma} \phi_i = 1. \tag{4.1}$$

In the following we use the vector notation $\vec{\phi} = (\phi_\alpha, \phi_\beta, \phi_\gamma)$. Generally, the phase-field parameter ϕ_i represents the volume fraction of phase i and is allowed to vary from 0 to 1, such that $\phi_\alpha = 1$, $\phi_\beta = \phi_\gamma = 0$ indicates the α phase. Additionally, an α/β interface is characterized by a spatial profile of phase fields in which ϕ_α and ϕ_β smoothly vary from 0 to 1 across the diffusional interface.

4.1.1 Free energy functional

We start with the Ginzburg-Landau type free energy functional:

$$F = \int_V \mathrm{d}V \left[H \left\{ \frac{W^2}{2} \sum_{i=\alpha,\beta,\gamma} (\boldsymbol{\nabla}\phi_i)^2 + \sum_{i=\alpha,\beta,\gamma} \phi_i^2 (1-\phi_i)^2 \right\} + X f_c \left(\vec{\phi}, c, T\right) \right], \quad (4.2)$$

which consists of three parts. The first one represents the gradient energy term, in which W is the interface width. The second part is a triple well potential, which is constructed as the sum of double-well potential for all phase fields. The free energy density H determines the height of the potential. The last term, formed as a function of phase fields $\vec{\phi}$, solute concentration c and temperature T, describes the free energy of the different bulk phases,

$$f_c \left(\vec{\phi}, c, T\right) = \frac{1}{2} \left[c - \sum_{i=\alpha,\beta,\gamma} A_i(T) g_i(\vec{\phi}) \right]^2 + \sum_{i=\alpha,\beta,\gamma} B_i(T) g_i(\vec{\phi}), \quad (4.3)$$

where $A_i(T)$ and $B_i(T)$ are functions of temperature T, to construct the desirable phase diagram, and g_i is an interpolating function, which is written as

$$g_i(\vec{\phi}) = \frac{\phi_i^2}{4} \Big\{ 15 (1-\phi_i) \left[1 + \phi_i - (\phi_k - \phi_j)^2 \right] + \phi_i \left(9\phi_i^2 - 5 \right) \Big\}, \quad (4.4)$$

where i, j, k are pairwise distinct (i.e. are all different). For binary interfaces, for example for an α/β interface with $\vec{\phi} = (\phi, 1-\phi, 0)$, the function $g_\alpha(\vec{\phi})$ reduces to the polynomial $p(\phi) = \phi^3(10 - 15\phi + 6\phi^2)$. The last term in Section 4.1.1 is parametrized by another free energy density X that sets the relation between the capillary length and the interface width W through the ratio H/X.

The chemical potential can be written as

$$u = \frac{\partial f_c}{\partial c} = c - \sum_{i=\alpha,\beta,\gamma} A_i(T) g_i(\vec{\phi}). \quad (4.5)$$

Specifically, the advantage of the fifth order interpolation function employed in the chemical free energy function is avoiding the appearance of spurious third phase contributions in a two phase interface [86].

4.1.2 Time evolution equations

We define our a scaled concentration field as

$$c = \frac{C - C_E}{C_\beta - C_\alpha}, \quad (4.6)$$

where C is the local alloy concentration, C_E, C_α, C_β are the equilibrium concentrations at the eutectic/eutectoid temperature T_E of the parent phase γ and growing phases α and β respectively. The concentration c is a conserved quantity that obeys the continuity equation

$$\dot{c} = -\boldsymbol{\nabla} \cdot \mathbf{J}, \quad (4.7)$$

where $\mathbf{J}$ is the diffusion flux.

Our goal is to write down a non-diagonal PF model in the spirit of Ref. [107] that formally maintains the symmetry between the different phase fields. In order to fulfill the condition (4.1), one may introduce a Lagrange multiplier in the free energy functional and its elimination yields the following definitions:

$$\left.\frac{\delta F}{\delta \phi_i}\right|_{\sum \phi_n=1} = \frac{2}{3}\frac{\delta F}{\delta \phi_i} - \frac{1}{3}\frac{\delta F}{\delta \phi_j} - \frac{1}{3}\frac{\delta F}{\delta \phi_k}, \tag{4.8}$$

$$\boldsymbol{\nabla}\phi_i|_{\sum \phi_n=1} = \frac{2}{3}\boldsymbol{\nabla}\phi_i - \frac{1}{3}\boldsymbol{\nabla}\phi_j - \frac{1}{3}\boldsymbol{\nabla}\phi_k. \tag{4.9}$$

Again, (i, j, k) is a permutation of (α, β, γ). The terms on the left side of these equations are operators explicitly informing that the constraint in Eq. (4.1) is fulfilled, while on the right side, the operators are calculated as if ϕ_α, ϕ_β and ϕ_γ were independent. In particular, we have

$$\sum_i \left.\frac{\delta F}{\delta \phi_i}\right|_{\sum \phi_n=1} = 0, \tag{4.10}$$

$$\sum_i \boldsymbol{\nabla}\phi_i|_{\sum \phi_n=1} = 0. \tag{4.11}$$

The Onsager linear relations between the driving forces and the fluxes that define the kinetics within the PF model are then

$$-\left.\frac{\delta F}{\delta \phi_i}\right|_{\sum \phi_n=1} = \tau\dot{\phi}_i + \left\{MW\ \boldsymbol{\nabla}\phi_i|_{\sum \phi_n=1}\right\}\cdot \mathbf{J}, \tag{4.12}$$

$$-\boldsymbol{\nabla}\frac{\delta F}{\delta c} = -\boldsymbol{\nabla}u = \sum_{i=\alpha,\beta,\gamma}\left\{MW\ \boldsymbol{\nabla}\phi_i|_{\sum \phi_n=1}\right\}\dot{\phi}_i + \frac{\mathbf{J}}{D}, \tag{4.13}$$

associated with the continuity equation (4.7) providing $\dot{u}$ through Eq. (4.5). We see that, due to Eqs. (4.10) and (4.11),

$$\sum_{i=\alpha,\beta,\gamma}\dot{\phi}_i = 0 \tag{4.14}$$

is locally satisfied at any time in accordance with the constraint in Eq. (4.1).

On the one hand, for each driving force in Eq. (4.12), we have a coupling to the conjugate flux $\dot{\phi}_i$ via the phase field dependent time scale $\tau = \tau(\vec{\phi})$, and a cross coupling to the diffusion flux $\mathbf{J}$ via the phase field dependent inverse velocity scale $M = M(\vec{\phi})$. The structure of the cross coupling term, and especially the reason for introducing the gradient of the phase field, is described in detail in [107, 109]. On the other hand, for the diffusion driving force, we have a coupling to the conjugate diffusion flux $\mathbf{J}$ via the phase field dependent diffusion coefficient $D = D(\vec{\phi})$, and to the three fluxes $\dot{\phi}_i$ via three cross coupling terms obeying Onsager symmetry, i.e. parametrized by the same coefficient as in the second term on the right-hand-side of Eq. (4.12). Let us note that when one omits the cross coupling term in Eq. (4.12) as in [86], the model corresponds to the PF model with the so-called anti-trapping current. This model is suited to a one-sided situation for eutectic growth, that does not require Onsager symmetry to be obeyed, as will be seen later. The Onsager relations given above may be represented using a 4×4 (symmetric) matrix, whose

determinant should be positive for a positive energy dissipation in the simulated system. Let us note that, while we have defined some phase field dependence of τ, M and D, we do not assume any for W, that is strictly a constant, yielding isotropic interface energies.

An explicit form of the evolution equations provided by Eqs. (4.12) and (4.13) can be obtained from a matrix inversion,

$$\begin{bmatrix} \dot{\phi}_\alpha \\ \dot{\phi}_\beta \\ \dot{\phi}_\gamma \end{bmatrix} = \begin{bmatrix} P_{\alpha\alpha} & P_{\alpha\beta} & P_{\alpha\gamma} \\ P_{\beta\alpha} & P_{\beta\beta} & P_{\beta\gamma} \\ P_{\gamma\alpha} & P_{\gamma\beta} & P_{\gamma\gamma} \end{bmatrix}^{-1} \begin{bmatrix} Q_\alpha \\ Q_\beta \\ Q_\gamma \end{bmatrix} \tag{4.15}$$

where, for $i \neq j$,

$$P_{ii} = \tau - D\left[MW\boldsymbol{\nabla}\phi_i|_{\sum \boldsymbol{\phi_n}=1}\right]^2, \tag{4.16}$$

$$P_{ij} = -DM^2W^2\boldsymbol{\nabla}\phi_i|_{\sum \boldsymbol{\phi_n}=1} \cdot \boldsymbol{\nabla}\phi_j|_{\sum \boldsymbol{\phi_n}=1}, \tag{4.17}$$

$$Q_i = -\left.\frac{\delta F}{\delta \phi_i}\right|_{\sum \boldsymbol{\phi_n}=1} + DMW\boldsymbol{\nabla}\phi_i|_{\sum \boldsymbol{\phi_n}=1} \cdot \boldsymbol{\nabla}u, \tag{4.18}$$

with

$$\begin{aligned} -\left.\frac{\delta F}{\delta \phi_i}\right|_{\sum \phi_n=1} &= HW^2\boldsymbol{\nabla}^2\phi_i - \frac{2H}{3}\Big[2\phi_i(1-\phi_i)(1-2\phi_i) \\ &\quad -\phi_j(1-\phi_j)(1-2\phi_j) - \phi_k(1-\phi_k)(1-2\phi_k)\Big] \\ &\quad + \sum_{j=\alpha,\beta,\gamma}(uA_j - B_j)\left[\frac{\partial g_j}{\partial \phi_i}(\vec{\phi}) - \frac{1}{3}\frac{\partial g_j}{\partial \phi_j}(\vec{\phi})\right] \end{aligned} \tag{4.19}$$

and

$$\frac{\partial g_i}{\partial \phi_i} = \frac{15\phi_i}{4}\left[(3\phi_i+2)(1-\phi_i)^2 + (3\phi_i-2)(\phi_j-\phi_k)^2\right], \tag{4.20}$$

$$\frac{\partial g_i}{\partial \phi_j} = -\frac{\partial g_i}{\partial \phi_k} = \frac{15}{2}\phi_i^2(1-\phi_i)(\phi_k-\phi_j) \tag{4.21}$$

for a permutation (i,j,k) of (α,β,γ).

For the chemical potential, we have

$$\dot{u} = \boldsymbol{\nabla}\cdot\left\{D\left[\boldsymbol{\nabla}u + \sum_{i=\alpha,\beta,\gamma} MW\dot{\phi}_i\boldsymbol{\nabla}\phi_i|_{\sum \phi_n=1}\right]\right\} - \sum_{i=\alpha,\beta,\gamma}\left[A_i(T)\sum_{j=\alpha,\beta,\gamma}\dot{\phi}_j\,\frac{\partial g_i}{\partial \phi_j}(\vec{\phi})\right]. \tag{4.22}$$

Again, if one sets $M = 0$, the evolution equations presented in [86] are recovered.

At equilibrium between two phases, for example between phase i and phase j, the one-dimensional (x is the spatial variable) phase field profiles reads

$$\phi_i^{eq}(x) = 1 - \phi_j^{eq}(x) = \phi_{eq}(x) = \frac{1}{2}\left[1 - \tanh\left(\frac{x}{\sqrt{2}\,W}\right)\right], \tag{4.23}$$

with $\phi_i^{eq}(x \to -\infty) = 1$ and $\phi_i^{eq}(x \to \infty) = 0$. The constant chemical potential equals

$$u_{ij}^{eq} = \frac{B_j - B_i}{A_j - A_i}, \tag{4.24}$$

and the concentration profile reads

$$c_{ij}^{eq}(x) = \frac{c_{ij}^0 + c_{ji}^0}{2} + \frac{c_{ij}^0 - c_{ji}^0}{2}\big\{2p[\phi_i^{eq}(x)] - 1\big\}, \tag{4.25}$$

where c_{ij}^0 (resp. c_{ji}^0) is the concentration in phase i (resp. phase j) when in equilibrium with phase j (resp. phase i).

It is important to generically map (not only for equilibrium) our three-phase field model to the problem of a two-phase system for which a single phase field ϕ is used. The fact that the variations of two phase fields are involved for a binary interface in our three-phase model brings additional contributions. In particular, the free energy of an interface between phase i and phase j reads now

$$\sigma_{ij} = 2\omega W H, \tag{4.26}$$

with the factor 2 coming from the fact that two phase fields are exhibiting hyperbolic tangent variations, and with the usual integral $\omega = W\int_{-\infty}^{\infty}[\partial_x\phi_i^{eq}(x)]^2\mathrm{d}x = \sqrt{2}/6$. We note here that in our fully symmetric model all interface energies are isotropic and equal, i.e. $\sigma_{ij} = \sigma_{jk} = \sigma_{ik}$. As for the classical eutectic growth, our results are expected to be qualitatively unchanged when, while remaining atomically rough, the interfaces present an anisotropic free energy. They are even expected to be quantitatively unchanged in the limit of small anisotropy. Concerning the dynamics, the three-phase field model for a two-phase system reduces to Onsager relations given by

$$-\frac{\delta F}{\delta \phi} = 2\tau\dot{\phi} + (2MW\boldsymbol{\nabla}\phi)\cdot\mathbf{J}, \tag{4.27}$$

$$-\boldsymbol{\nabla}\frac{\delta F}{\delta c} = (2MW\boldsymbol{\nabla}\phi)\dot{\phi} + \frac{\mathbf{J}}{D}. \tag{4.28}$$

These are, up to the factors 2 arising from the double contributions of the phase fields, the same Onsager relations presented in Ref. [107] where the kinetic cross coupling parametrized by M is introduced.

Before presenting the thin-interface results that link the parameters of the PF model with sharp interface conditions at the interfaces, let us define the dissipation function. It corresponds to the positive form built out of the products of the driving forces and their respective conjugate flux:

$$\begin{aligned}\dot{S} &= \int_V \mathrm{d}V\left(-\sum_{i=\alpha,\beta,\gamma}\frac{\delta F}{\delta\phi_i}\Big|_{\sum\phi_n=1}\dot{\phi}_i - \boldsymbol{\nabla}\frac{\delta F}{\delta c}\cdot\mathbf{J}\right)\\ &= \int_V \mathrm{d}V\left\{\tau\sum_{i=\alpha,\beta,\gamma}\left(\dot{\phi}_i\right)^2 + 2MW\left(\sum_{i=\alpha,\beta,\gamma}\dot{\phi}_i\boldsymbol{\nabla}\phi_i\Big|_{\sum\phi_i=1}\right)\cdot\mathbf{J} + \frac{\mathbf{J}^2}{D}\right\}.\end{aligned} \tag{4.29}$$

For a binary interface, for example j/k for which $\phi_i = 0, \phi_j = \phi, \phi_k = 1-\phi$, the dissipation reads

$$\dot{S}_{j/k} = \int_V \mathrm{d}V\left\{2\tau\left(\dot{\phi}\right)^2 + 4MW\dot{\phi}\boldsymbol{\nabla}\phi\cdot\mathbf{J} + \frac{\mathbf{J}^2}{D}\right\}, \tag{4.30}$$

and we recover the dissipation function for a PF model with a single phase field ϕ, i.e. $\dot{S} = \int_V \mathrm{d}V[(-\delta F/\delta\phi)\dot{\phi} + (-\boldsymbol{\nabla}\delta F/\delta c)\cdot\mathbf{J}]$, with Onsager relations given by Eqs. (4.27) and (4.28). The condition of positiveness of the dissipation $\dot{S}_{j/k}$ then reads $2\tau/D - 4M^2W^2\phi_{eq}'^2 > 0$.

4.1.3 Link with the free boundary description: thin-interface limit

In this section, we present the relation between the parameters that enter the PF model and the parameters that enter the sharp interface boundary conditions. This is called the thin-interface limit of the PF model and allows to set the PF parameters such that, even with varying interface width W, the desired boundary conditions are achieved in the equivalent sharp interface model. In particular, at low enough interface velocities, equilibrium boundary conditions may be assumed. We restrict ourselves to the binary interfaces, whereas an analysis of the triple junction is beyond the scope of this work.

The conservation of atoms A and B at a moving interface between phase i and j implies the relation

$$D_i \boldsymbol{\nabla} c|_i \cdot \mathbf{n} + V c_{ij}^0 = D_j \boldsymbol{\nabla} c|_j \cdot \mathbf{n} + V c_{ji}^0 = J_B. \tag{4.31}$$

V and J_B are the total normal flux of all atoms through the interface (i.e. the normal velocity) and the normal flux of atoms B through the interface, respectively. If J_A is the normal flux of atoms A, then $V = J_A + J_B$ (we neglect any volume density differences between the phases). The concentration gradient $\boldsymbol{\nabla} c|_i$ ($\boldsymbol{\nabla} c|_j$) is evaluated at the interface on the side of phase i (phase j) and $\mathbf{n}$ is the local unit vector normal to the interface V and J_B are then the scalar products of the actual fluxes and $\mathbf{n}$. D_i (D_j) is the bulk diffusion coefficient in phase i (phase j). Here we have assumed weak out-of-equilibrium conditions such that the concentration in phase i (phase j) that enters the mass conservation equations is the equilibrium concentration c_{ij}^0 (c_{ji}^0).

Together with mass conservation, kinetic boundary conditions are defined. They relate linearly the jumps $\delta\Omega$ and δu across the interface of the grand potential and the chemical potential (rigorously the diffusion potential), respectively, to the two fluxes V and J_B. These boundary conditions involve the bulk free energies $f_i(c)$ and $f_j(c)$ of the two phases and especially their second derivatives at i/j equilibrium [which is equal to 1 for the parabolic free energies in Eq. (4.3)]. They prescribe the interface concentrations c_{ij} and c_{ji} when the sharp interface problem is solved, according to $\delta\Omega = f_j''(c_{ji}^0)c_{ji}^0(c_{ji} - c_{ji}^0) - f_i''(c_{ij}^0)c_{ij}^0(c_{ij} - c_{ij}^0)$ and $\delta u = f_i''(c_{ij}^0)(c_{ij} - c_{ij}^0) - f_j''(c_{ji}^0)(c_{ji} - c_{ji}^0)$. Consequently, the kinetic boundary conditions are written as

$$\delta\Omega = \bar{\mathcal{A}} V + \bar{\mathcal{B}} J_B + d_0 \kappa, \tag{4.32}$$

$$\delta u = \bar{\mathcal{B}} V + \bar{\mathcal{C}} J_B, \tag{4.33}$$

where $\bar{\mathcal{A}}, \bar{\mathcal{B}}, \bar{\mathcal{C}}$ are the components of the 2×2 Onsager matrix of kinetic coefficients, d_0 is the capillary length (as mentioned in Section 4.1.1, the relation between the capillary length and the interface width in the present PF model is given by $d_0/W = 2\omega H/X$) and κ the curvature of the interface. In the following we present the strategy to achieve equilibrium boundary conditions, i.e. $\delta\Omega = 0$ and $\delta u = 0$, even when V and J_B do not vanish. In this case one recovers the Gibbs-Thomson relation:

$$c_{ij} - c_{ij}^0 = (c_{ji} - c_{ji}^0) f_j''/f_i'' = -\tilde{d}\kappa, \tag{4.34}$$

where

$$\tilde{d} = \frac{d_0}{(c_{ij}^0 - c_{ji}^0) f_i''}. \tag{4.35}$$

The equilibrium concentrations c_{ij}^0 and c_{ji}^0 are temperature dependent through A_i and B_i.

In [108], the general expressions for the kinetic coefficients $\bar{\mathcal{A}}, \bar{\mathcal{B}}$ and $\bar{\mathcal{C}}$ in terms of the PF model equilibrium properties were derived. For our equilibrium i/j interface centered at $x = 0$, we have $\phi_i(x) = \phi_{eq}(x)$ given by Eq. (4.23), $\phi_j(x) = 1 - \phi_{eq}(x)$, and $\phi_k(x) = 0$. Furthermore, we have $c(x) = c_{eq}(x) = (c_{ij}^0 + c_{ji}^0)/2 + \{(c_{ij}^0 - c_{ji}^0)/2\}\{2p[\phi_{eq}(x)] - 1\}$ given by Eq. (4.25). Here we note that, since $p(\phi) = \phi^3(10 - 15\phi + 6\phi^2)$, $2p-1$ is an odd function of x. Taking into account the double contribution of the phase fields at binary interfaces, the kinetic coefficients read

$$\begin{aligned} \bar{\mathcal{A}} = 2 \int_{-\infty}^{\infty} \tau [\phi_{eq}'(x)]^2 \mathrm{d}x - 4 \int_{-\infty}^{\infty} \left\{ MW [\phi_{eq}'(x)]^2 c_{eq}(x) \right\} \mathrm{d}x \\ + \int_{-\infty}^{\infty} \left\{ \frac{c_{eq}^2(x)}{D} - \frac{(c_{ij}^0)^2}{2D_i} - \frac{(c_{ji}^0)^2}{2D_j} \right\} \mathrm{d}x, \end{aligned} \tag{4.36}$$

$$\bar{\mathcal{B}} = 2 \int_{-\infty}^{\infty} \left\{ MW [\phi_{eq}'(x)]^2 \right\} \mathrm{d}x - \int_{-\infty}^{\infty} \left\{ \frac{c_{eq(x)}}{D} - \frac{c_{ij}^0}{2D_i} - \frac{c_{ji}^0}{2D_j} \right\} \mathrm{d}x, \tag{4.37}$$

$$\bar{\mathcal{C}} = \int_{-\infty}^{\infty} \left\{ \frac{1}{D} - \frac{1}{2D_i} - \frac{1}{2D_j} \right\} \mathrm{d}x. \tag{4.38}$$

We recall at this point that in these expressions $\tau = \tau(\vec{\phi})$, $M = M(\vec{\phi})$ and $D = D(\vec{\phi})$, which we have not specified yet.

For a two-phase PF model with a single phase field ϕ, it was shown that constant τ and M are sufficient to achieve the desired boundary conditions, both for a one-sided [108] and a two-sided model [109]. Here, for the three-phase model, the necessity for the constraint in Eq. (4.1) to be fulfilled imposes that $\tau(\vec{\phi})$ and $M(\vec{\phi})$, as single quantities, contain enough information for the properties of the three kind of interfaces to be ascribed independently. We have chosen the following forms with six parameters:

$$\tau(\vec{\phi}) = \tau_{\alpha\beta}(1 + \phi_\alpha \phi_\beta) + \tau_{\beta\gamma}(1 + \phi_\beta \phi_\gamma) + \tau_{\gamma\alpha}(1 + \phi_\gamma \phi_\alpha), \tag{4.39}$$

$$M(\vec{\phi}) = M_{\alpha\beta} \phi_\alpha \phi_\beta + M_{\beta\gamma} \phi_\beta \phi_\gamma + M_{\gamma\alpha} \phi_\gamma \phi_\alpha. \tag{4.40}$$

The diffusion coefficient $D(\vec{\phi})$ should be able to reproduce the three different bulk diffusion coefficients but also to allow for a tuning of the effective surface diffusion coefficient that arises due to the finiteness of the interface width W [110]. As shown in [109], the phase field dependent diffusion coefficient appears as harmonic mean in order for $\bar{\mathcal{C}}$ to vanish. Here, we define

$$\frac{1}{D(\vec{\phi})} = \frac{1}{3} \sum_{i=\alpha,\beta,\gamma} \left\{ \frac{1}{D_i} + h_i(\vec{\phi}) \left(\frac{1}{D_i} - \frac{1}{2D_j} - \frac{1}{2D_k} \right) \right\} \tag{4.41}$$

where

$$h_i(\vec{\phi}) = (2\phi_i - 1)(1 + 4a_{ij}\phi_i\phi_j + 4a_{ik}\phi_i\phi_k), \tag{4.42}$$

for a permutation (i,j,k) of (α,β,γ). We have here three additional parameters a_{ij}. We will see in the following how the assumptions of equilibrium boundary conditions and vanishing surface diffusion allow to determine the nine parameters $\tau_{ij}, M_{ij}, a_{ij}$.

For a binary i/j interface, $D_{i/j}(\phi) = D(\phi_i = \phi, \phi_j = 1-\phi, \phi_k = 0)$ is such that

$$\frac{1}{D_{i/j}(\phi)} = \frac{1}{2D_i} + \frac{1}{2D_j} + h_{i/j}(\phi)\left(\frac{1}{2D_i} - \frac{1}{2D_j}\right), \tag{4.43}$$

where

$$h_{i/j}(\phi) = (2\phi - 1)\big[1 + 4a_{ij}\phi(1-\phi)\big]. \tag{4.44}$$

This is precisely the phase field dependent diffusion coefficient that was used in the two-phase model presented in Ref. [110]. Let us however note that in Ref. [110] ϕ varies from -1 to 1, while here it is in the range 0 to 1. The factor 4 in $h_{i/j}(\phi)$ then allows a_{ij} to be identified with a in Ref. [110].

Returning to our calculation of the kinetic coefficients given in Eqs. (4.36) to (4.38), we find for the i/j interface:

$$\bar{\mathcal{A}} = 2\,\frac{\omega(\tau_{\alpha\beta}+\tau_{\beta\gamma}+\tau_{\gamma\alpha}) + \chi\tau_{ij}}{W} - \frac{\zeta(c^0_{ij}-c^0_{ji})^2}{4}\left(\frac{W}{2D_i}+\frac{W}{2D_j}\right), \tag{4.45}$$

$$\bar{\mathcal{B}} = 2\chi M_{ij} - \frac{\varrho_{ij}(c^0_{ji}-c^0_{ij})}{2}\left(\frac{W}{2D_i}-\frac{W}{2D_j}\right), \tag{4.46}$$

$$\bar{\mathcal{C}} = 0, \tag{4.47}$$

where

$$\chi = W\int_{-\infty}^{\infty}\phi_{eq}[1-\phi_{eq}]\,[\phi'_{eq}]^2\mathrm{d}x \approx 0.04714, \tag{4.48}$$

$$\zeta = \frac{1}{W}\int_{-\infty}^{\infty}\Big(1-\{2p[\phi_{eq}]-1\}^2\Big)\mathrm{d}x \approx 1.40748, \tag{4.49}$$

$$\varrho_{ij} = \frac{1}{W}\int_{-\infty}^{\infty}\Big(1-\big(2p[\phi_{eq}]-1\big)h_{i/j}(\phi_{eq})\Big)\mathrm{d}x. \tag{4.50}$$

As mentioned above, $\bar{\mathcal{C}}$ vanishes, and this is due to the oddness of $h_{i/j}(\phi_{eq})$, i.e. the oddness of $2\phi_{eq}-1$. In order to achieve equilibrium boundary conditions at the i/j interface, i.e. having $\delta\Omega = 0$ and $\delta u = 0$ in Eqs. (4.32) and (4.33), we need also $\bar{\mathcal{A}} = 0$ and $\bar{\mathcal{B}} = 0$. Moreover, we want to achieve equilibrium conditions also at the j/k and the k/i interfaces. The condition $\bar{\mathcal{A}} = 0$ at each interface yields 3 equations for the 3 parameters $\tau_{\alpha\beta}, \tau_{\beta\gamma}, \tau_{\gamma\alpha}$:

$$\chi\tau_{ij} + \omega(\tau_{\alpha\gamma}+\tau_{\alpha\beta}+\tau_{\beta\gamma}) = \frac{\zeta(c^0_{ij}-c^0_{ji})^2}{8}\left(\frac{W^2}{2D_i}+\frac{W^2}{2D_j}\right) = A_{ij}, \tag{4.51}$$

where i,j,k are pairwise different, and the solution for τ_{ij} reads

$$\tau_{ij} = \frac{1}{\chi}\left[A_{ij} - \frac{\omega}{3\omega+\chi}(A_{\alpha\gamma}+A_{\alpha\beta}+A_{\beta\gamma})\right]. \tag{4.52}$$

On the other hand, $\bar{\mathcal{B}} = 0$ at the three interfaces yields three more equations,

$$M_{ij} = \frac{\varrho_{ij}(c^0_{ji}-c^0_{ij})}{4\chi}\left(\frac{W}{2D_i}-\frac{W}{2D_j}\right). \tag{4.53}$$

We note here that no cross coupling is necessary, i.e. $M_{ij} = 0$, when $D_i = D_j$. In the general case, M_{ij} does not vanish and depends on ϱ_{ij}, that remains to be determined. This is achieved by the assumption of vanishing surface diffusion coefficient, through the determination of a_{ij}. This corresponds to the condition

$$\int_{-\infty}^{\infty} \mathrm{d}x \left(D_{i/j}(\phi_{eq}) - \frac{D_i}{2} - \frac{D_j}{2} \right) = 0. \tag{4.54}$$

This gives three additional equations in order to be able to fully determine the nine aforementioned parameters. The coefficient a_{ij} that satisfies Eq. (4.54) is a function of the ratio D_i/D_j, and it has the property: $a_{ij}(D_i/D_j) = a_{ij}(D_j/D_i)$ [99]. Hence, we have also $\varrho_{ij}(D_i/D_j) = \varrho_{ij}(D_j/D_i)$. In Fig. 3.1, we present the values of a_{ij} and ϱ_{ij} as a function of $D_i/D_j > 0.06$.

Let us give a brief comment before presenting the one-sided model. We have seen that the condition of positiveness of the dissipation corresponds to the inequality $2\tau/D - 4M^2W^2\phi_{eq}'^2 > 0$, and thus the magnitude of M may not be too large. When considering equilibrium boundary conditions, this inequality sets an upper bound for the contrast D_i/D_j beyond which M is too large. According to our definition of $\tau(\vec{\phi})$, τ_{ij} is a function of all three diffusion coefficients (see Eq. (4.52)) and the maximum contrast D_i/D_j depends on the other contrasts D_i/D_k and D_j/D_k. In this respect, more suitable definitions of $\tau(\vec{\phi})$ may be used. In Fig. 3.1, $(D_i/D_j)_{min} = 0.06$ corresponds roughly to the maximum contrast that is used in the simulations in the following section, i.e. $(D_j/D_i)_{max} = 15$.

One-sided model. Here, we present simulations for a negligible diffusion coefficient in the growing phases α and β ($D_\alpha, D_\beta \ll D_\gamma$). In the PF model, we then use

$$\tau_{\alpha\beta} = 0, \tag{4.55}$$
$$M_{\alpha\beta} = 0, \tag{4.56}$$
$$D(\vec{\phi}) = D_{1s}(\vec{\phi}) = D_\gamma(1 - \phi_\alpha - \phi_\beta). \tag{4.57}$$

In the mass conservation equation (4.31) for an interface between the mother phase γ and one of the growing phases j ($j = \alpha, \beta$), the diffusion flux in the growing phase vanishes, yielding

$$V c_{j\gamma}^0 = J_B. \tag{4.58}$$

The kinetic boundary conditions (4.32), (4.33) become

$$\delta\Omega = (\bar{\mathcal{A}} + c_{j\gamma}^0 \bar{\mathcal{B}})V + d_0\kappa, \tag{4.59}$$
$$\delta u = (\bar{\mathcal{B}} + c_{j\gamma}^0 \bar{\mathcal{C}})V. \tag{4.60}$$

The two fluxes V and J_B are no more linearly independent, and Onsager symmetry becomes irrelevant since for example two driving forces are expressed in terms of a single flux. As mentioned earlier, this allows to use the PF model with the so-called anti-trapping current.

In view of Eqs. (4.59) and (4.60), the assumption of equilibrium boundary conditions thus demands $\bar{\mathcal{A}} + c_{j\gamma}^0 \bar{\mathcal{B}} = 0$ and $\bar{\mathcal{B}} + c_{j\gamma}^0 \bar{\mathcal{C}} = 0$. According to Eqs. (4.36),

(4.37), and (4.38), we have

$$\bar{\mathcal{A}} + c_{j\gamma}^0 \bar{\mathcal{B}} = 2\frac{(\omega+\chi)\tau_{j\gamma} + \omega\tau_{k\gamma}}{W} - \frac{(c_{\gamma j}^0 - c_{j\gamma}^0)^2 W\xi}{4D_\gamma} \tag{4.61}$$

$$\bar{\mathcal{B}} + c_{j\gamma}^0 \bar{\mathcal{C}} = 2\chi M_{j\gamma} - \frac{(c_{\gamma j}^0 - c_{j\gamma}^0) W\kappa}{2D_\gamma} \tag{4.62}$$

where

$$\kappa = \frac{1}{W}\int_{-\infty}^{\infty} \frac{\phi_{eq} + 1 - 2p[\phi_{eq}]}{1-\phi_{eq}} \mathrm{d}x \approx 2.12132, \tag{4.63}$$

$$\xi = \frac{1}{W}\int_{-\infty}^{\infty} \frac{1 - (2p[\phi_{eq}]-1)^2}{1-\phi_{eq}} \mathrm{d}x \approx 3.42778. \tag{4.64}$$

The assumption of equilibrium boundary conditions at interfaces α/γ and β/γ provides four equations for $\tau_{\alpha\gamma}, \tau_{\beta\gamma}, M_{\alpha\gamma}, M_{\beta\gamma}$ ($j = \alpha, \beta$, $k \neq j$):

$$M_{j\gamma} = \frac{(c_{\gamma j}^0 - c_{j\gamma}^0) W\kappa}{4\chi D_\gamma}, \tag{4.65}$$

and

$$(\omega+\chi)\tau_{j\gamma} + \omega\tau_{k\gamma} = \frac{(c_{\gamma j}^0 - c_{j\gamma}^0)^2 W^2 \xi}{8D_\gamma} = A_j^{1s}, \tag{4.66}$$

yielding

$$\tau_{j\gamma} = \frac{1}{\chi}\left[A_j^{1s} - \frac{\omega}{2\omega+\chi}(A_\alpha^{1s} + A_\beta^{1s})\right]. \tag{4.67}$$

Here, for an interface j/γ for which $\phi_j(x) = \phi_{eq}(x)$, we have $D = 1-\phi_{eq}$ and surface diffusion is automatically eliminated, i.e. $\int_{-\infty}^{\infty}(D - D_\gamma/2)\mathrm{d}x = (D_\gamma/2)\int_{-\infty}^{\infty}(1 - 2\phi_{eq})\mathrm{d}x = 0$.

4.2 Simulation details

To investigate the capabilities of the non-diagonal three PF model during eutectic/eutectoid transformations, we perform two-dimensional simulations of lamellar steady-state growth with different diffusivities in the growing phases, and different global compositions C_∞, i.e. different compositions in the mother phase far ahead of the growth front. In dimensionless units we thus define $c_\infty = (C_\infty - C_E)/(C_\beta - C_\alpha)$. In a first step we perform simulations corresponding to eutectic directional solidification (with one-sided diffusion). The scaled undercooling at the steady-state growth front is extracted from simulations and benchmarked against the boundary integral calculations reported in Ref. [86]. In a second step we perform simulations of isothermal transformations in the two-sided case. The non-diagonal PF simulation results are analyzed in the frame of the extended Jackson-Hunt theory by Ankit *et al.* [152] for various lamellar spacings λ at the eutectoid and one off-eutectoid compositions.

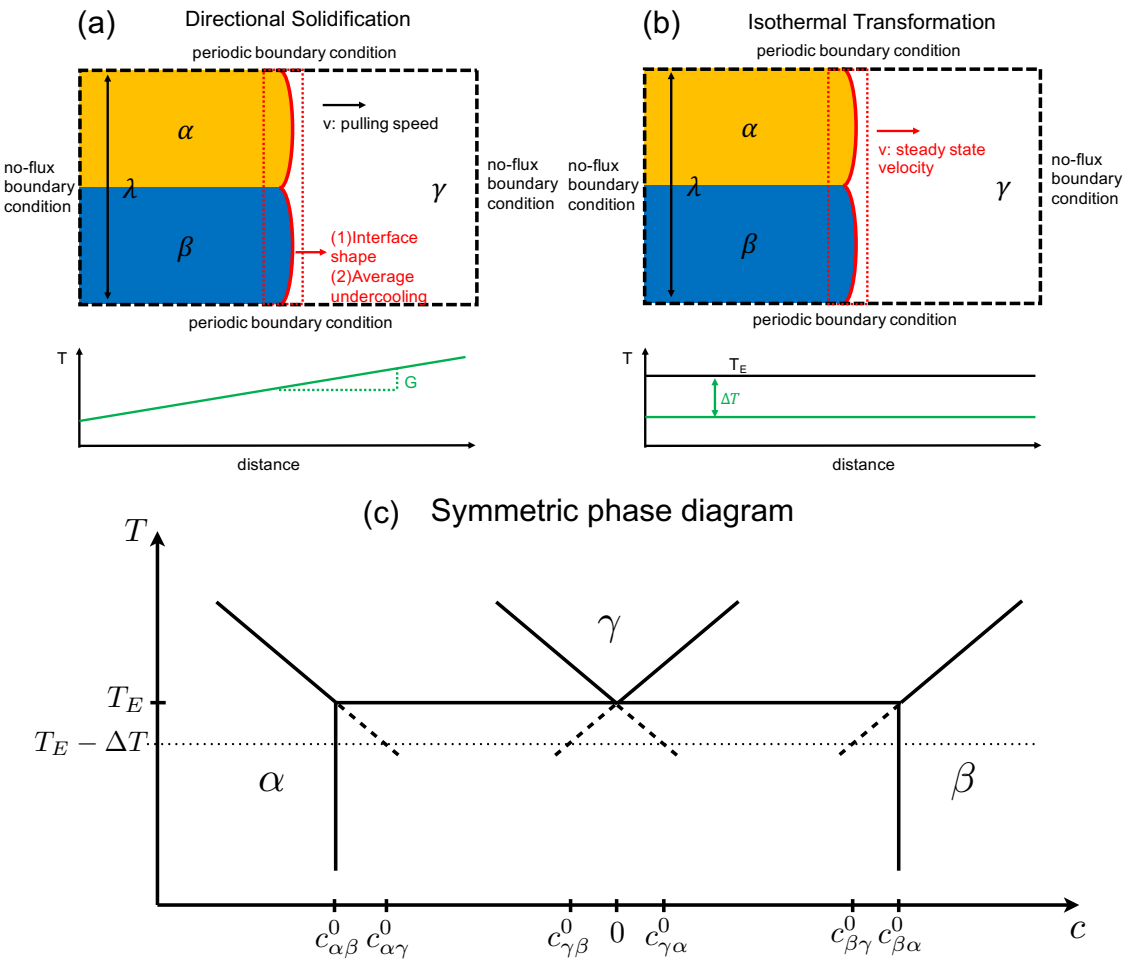

Figure 4.1: (a) and (b) show the setup of the simulations during directional solidification and during isothermal transformations, respectively. (c) Symmetric phase diagram for eutectic/eutectoid transformations.

The 2D simulation boxes of total size $n_x \times n_y$ with the grid spacing $\Delta x = \Delta y = 0.4W$ are illustrated in Figs. 4.1a and b, where n_x and n_y are the length of simulation boxes in the direction parallel and perpendicular to the solidification front. We require $\lambda \leq 0.1 n_y$ to ensure that the simulation domain is large enough in order to describe the diffusion field in the parent phase. For the purpose of obtaining steady state periodic lamellar arrays, periodic boundary conditions are prescribed at the boundaries parallel to the growth direction, while no-flux boundary conditions are used at the boundaries perpendicular to the growth direction (see Fig. 4.1). Also, a moving-frame method and GPU acceleration are applied in the simulations to reduce the computational effort.

Following Ref. [86], we assume for the symmetric phase diagram that $A_\gamma = B_\gamma = 0$, that the A_i's are independent of the temperature T, i.e.

$$A_\alpha = -A_\beta = -0.5, \tag{4.68}$$

and that

$$B_\alpha = A_\alpha \Delta = B_\beta = -A_\beta \Delta. \tag{4.69}$$

In this way, the concentration of phase i in equilibrium with phase j reads $c^0_{ij} =$

$A_i + (B_j - B_i)/(A_j - A_i)$. Explicitly, this gives

$$c^0_{\alpha\beta} = -c^0_{\beta\alpha} = A_\alpha, \tag{4.70}$$

$$c^0_{\gamma\alpha}(T) = c^0_{\alpha\gamma}(T) - A_\alpha = -c^0_{\gamma\beta}(T) = A_\beta - c^0_{\beta\gamma}(T) = \Delta, \tag{4.71}$$

where $\Delta = \frac{T_E - T}{m(C_\beta - C_\alpha)}$ with $m > 0$ being the liquidus slope. Thus Δ is the dimensionless undercooling. The corresponding phase diagram is schematically presented in Fig. 4.1c. In a positive thermal gradient in the z-direction, we have $\Delta = (z_E - z)/l_T$ where z_E is the position of the eutectic/eutectoid temperature and $l_T > 0$ denotes the corresponding thermal length.

In the first step corresponding to eutectic directional solidification, we choose three different values for λ_e/W, i.e. $\lambda_e/W = 64, 96, 128$, where λ_e is the Jackson-Hunt spacing (corresponding to the minimum undercooling) given in Eq. (2.17) in Ref. [86] (recall that here $\sin\theta_\alpha = \sin\theta_\beta = 1/2$), i.e. $\lambda_e = \sqrt{l_D \tilde{d}/P(\eta)}$ where $l_D = D_\gamma/V$ and the polynomial $P(\eta) = \sum_{n=1}^{\infty} \sin^2(\pi\eta n)/(\pi n)^3$ depends on the phase fraction $\eta = (c^0_{\beta\alpha} - c_\infty)/(c^0_{\beta\alpha} - c^0_{\alpha\beta})$ of phase α (which is 1/2 at eutectic composition). For each of these values, we then choose $\tilde{d}$ and l_D such that $l_D/\tilde{d} = 51200$. The thermal gradient is chosen such that $l_T/l_D = 4$.

In the second step corresponding to isothermal eutectoid transformations, we prescribe $\tilde{d}/W = 0.5$ and an undercooling $\Delta = 0.03125$ [see Eq. (4.71)]. This gives λ_e such that, according to $\lambda_e = \tilde{d}/[\eta(1-\eta)\Delta]$, $\lambda_e/W = 64$ for $c_\infty = 0$ (i.e. $\eta = 0.5$), and $\lambda_e = 66.6667$ for $c_\infty = 0.1$ (i.e. $\eta = 0.4$).

4.3 Results and discussions

4.3.1 Verification of the non-diagonal PF model in the one-sided case

In the present section, we perform non-diagonal PF (NPF, i.e. with cross-coupling term $M(\vec{\phi})$) and classical PF (CPF, $M(\vec{\phi}) = 0$) simulations in the one-sided case for different lamellar spacings, $\lambda = \lambda_e = 64W, 96W$ and $128W$, during directional solidification. λ_e is related to the spacing with the minimum interface undercooling for directional solidification and to the maximum growth velocity for isothermal solidification. We extract the scaled interface shapes in steady state from the PF simulations and benchmark them with boundary integral (BI) calculations, as presented in Fig. 4.2a. The position z is the distance to the eutectic temperature, that lies ahead at higher temperature, and is normalized by the thermal length l_T. As can be seen, when the abnormal interface effects are eliminated in the NPF simulations, the quantitative agreement with the BI calculation is significantly improved compared to the CPF simulations. We quantify this improvement in Fig. 4.2b where we give the deviation of the lamella's tip position in the PF simulations from the one obtained in the BI calculation. Let us note also that, as the inset in Fig. 4.2a and the dependence on W/λ_e in Fig. 4.2b show, we obtain a better agreement with the BI method when a better separation of length scale is achieved, i.e. when λ_e/W increases.

Next, using the parameters as aforementioned, a series of NPF simulations is performed at $\lambda = \lambda_e$ for various λ_e during directional solidification. The dependence

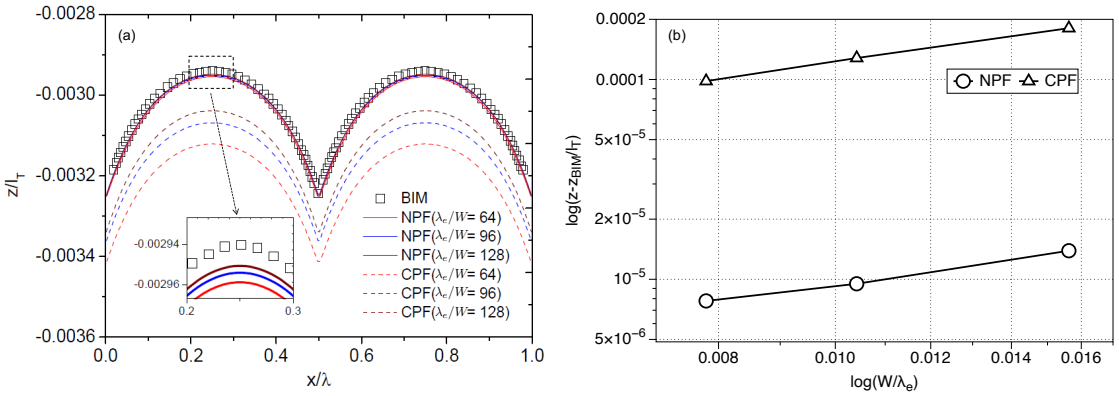

Figure 4.2: (a) Comparison between NPF (solid lines) and CPF (dashed lines) simulation results with the boundary integral method (BIM, squares) taken from Ref. [86] for $\lambda_e/W = 64$, 96 and 128. Inset: enlargement of the dashed rectangle. (b) Deviation of the lamella's tip position ($x/\lambda = 0.25$) between NPF and CPF simulation results and BI calculations.

on the lamellar spacing of the extracted average interface undercooling in the steady state regime can then be compared with the Jackson-Hunt theory and is exhibited in Fig. 4.3. As can be seen from the comparison, there exists a 5%-7% discrepancy with the JH theory, due to the assumption of a flat solidification front in the latter theory. In addition, we also show the results from Ref. [86] in Fig. 4.3. We see a slight discrepancy with our NPF results, certainly due to the fact that we use a symmetric matrix in the force-flux Onsager relations, while only the anti-trapping current is present in the model used in Ref. [86] (see the brief discussion immediately after Eq. (4.60)). Overall, the capabilities of the NPF model for eutectics, i.e. when diffusion in the growing phases is inhibited, are demonstrated in a convincing way.

4.3.2 Comparison of the non-diagonal PF model with the extended JH theory in the two-sided case

In this section, we investigate the case where diffusion is also present in the growing phases, i.e. where $\mu_\alpha = D_\alpha/D_\gamma$ and $\mu_\beta = D_\beta/D_\gamma$ are finite. As mentioned in the introduction, an extension of the JH theory was developed [152] in order to take into account these additional ingredients in the dynamics of the system. Within this theory, diffusion fluxes in the growing phases are simply added to the flux in the mother phase, and in isothermal conditions, the velocity

$$V = V_{JH}\rho \tag{4.72}$$

is multiplied by the factor ρ given in Eq. (B.53). For our symmetric phase diagram, we have

$$\rho = 1 + A\big[\mu_\alpha\eta + \mu_\beta(1-\eta)\big], \tag{4.73}$$

where A is described as a factor related to the difference in solidus and liquidus slopes. First we perform simulations for $\mu_\alpha = \mu_\beta$. The cross coupling parameter $M_{\alpha\beta}$ thus vanishes and surface diffusion is automatically suppressed at the α/β interface (no need to adjust the coefficient $\varrho_{\alpha\beta}$ - see discussion following Eq. (4.53)).

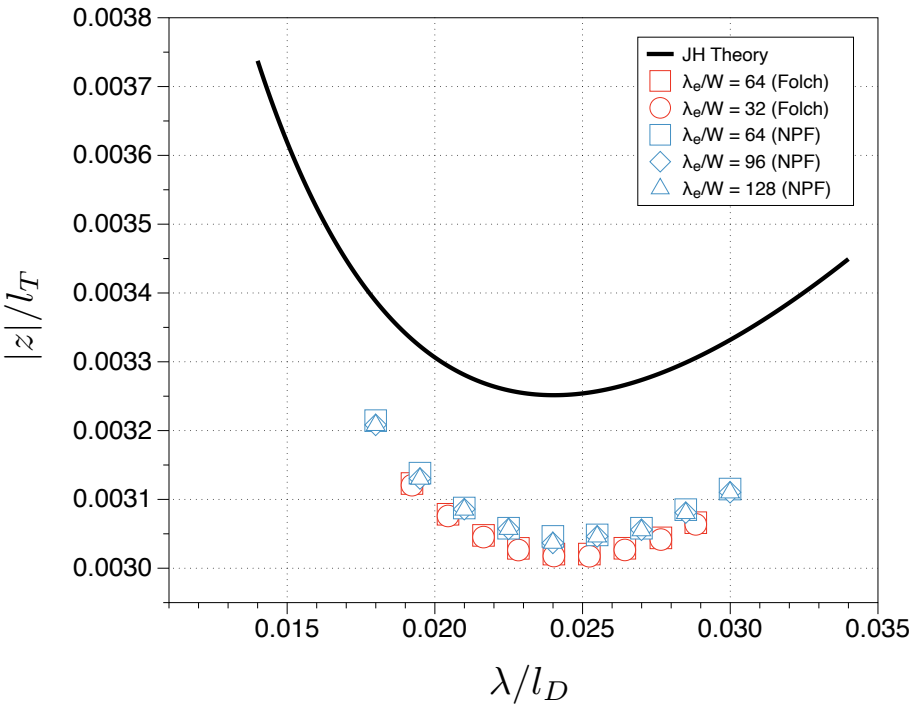

Figure 4.3: Comparison between the PF simulation results and Jackson-Hunt theory during directional solidification for different λ_e/W. The solid line is the Jackson-Hunt theory. The blue points present the NPF results. The red points indicate the results taken from Ref. [86].

Moreover, we use $c_\infty = 0$ ($\eta = 0.5$), yielding a fully symmetric pattern. We investigate the dependence of the growth velocity on λ (we recall that $\lambda_e/W = 64$ and $\tilde{d}/W = 0.5$).

Since the extension of the JH theory in Ref. [152] is only approximate, at least because it neglects some curvature effects just as Jackson and Hunt do, we have decided to determine A by choosing the value for which Eq. (4.72) best fits our simulations results for $\mu_\alpha = \mu_\beta = 1$. We found $A = 0.8924$.

In order to investigate the relevance of the scaling proposed by Eq. (4.72), we plot in Fig. 4.4 the rescaled dimensionless velocity

$$\tilde{V} = \frac{V\lambda_e}{D_\gamma}\,\frac{1}{\rho} \tag{4.74}$$

as a function of λ for $0 \leq \mu \leq 15$ where $\mu = \mu_\alpha = \mu_\beta$. Here we thus have $\rho = 1 + 0.8924\mu$. The solid line corresponds to the reference case, i.e. $\mu = 1$, that provides through the fit the quantity ρ (through A) by which we divide the velocity. We clearly observe a scattering of the simulations results around the solid line, showing that $\tilde{V}$ is not independent of μ. However, the relatively small amplitude of this scattering demonstrates that Eq. (4.72) provides a very good prediction of the velocity. Indeed, in view of the fact that μ spans a huge range within which the velocity is multiplied by a factor close to 15, a discrepancy of at most 30% for $\tilde{V}$ between the cases $\mu = 0$ and $\mu = 15$ corresponds to a rather convincing data collapse. If the arguments developed in Ref. [152] were inappropriate and for example diffusion would not take place in the growing phases even if their diffusion coefficient is large, the velocity would not change much when this diffusion coefficient

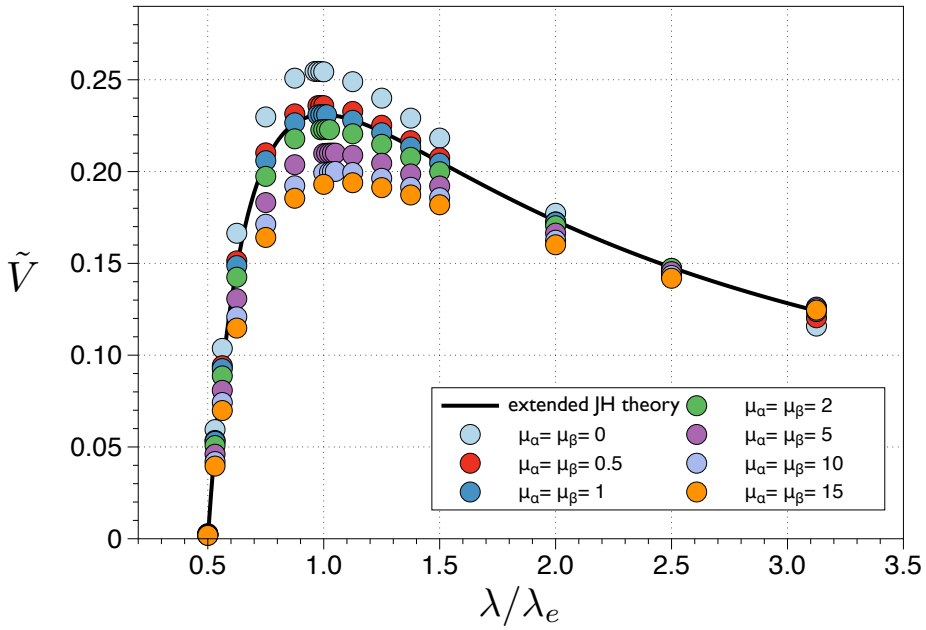

Figure 4.4: Rescaled dimensionless growth velocities obtained from NPF simulations for different lamellar spacing with a varying diffusion coefficient being equal in the growing phases, i.e. $0 \leq \mu \leq 15$ ($\mu = \mu_\alpha = \mu_\beta$). The solid lines corresponds to $\mu = 1$ (see text). The relatively small amplitude of the scattering of the results for a given λ validates the relevance of Eq. (4.72) to predict the velocity as a function of μ.

increases, and $\tilde{V}$ would end up close to 0.01 at $\lambda/\lambda_e = 1$. The situation here is very different.

When we look, for a given λ, at the dependence of $\tilde{V}$ on μ, our simulations suggest that it converges when μ becomes large. When $\mu \gg 1$, i.e. when the diffusion coefficient in the growing phases α and β is much larger than the one in the mother phase γ, the main diffusion path is within the growing phases and the diffusion fluxes in the mother phase become negligible. Then, $\rho \sim \mu$, and the steady-state velocity becomes proportional to $D_\alpha = D_\beta$ according to $V/D_\gamma \sim \rho \sim D_{\alpha(\beta)}/D_\gamma$. Thus, V exhibits a linear variation with μ (i.e. $\tilde{V}$ becomes independent of μ) when $\mu \gg 1$, and the shape of the interfaces becomes self-similar. This is what we see in Figure 4.5, where we plot the shape of the α/γ and β/γ interfaces (we recall that due to symmetry the α/β interface is straight behind the triple junction) for $\lambda/\lambda_e = 1$ and $\lambda/\lambda_e = 2$, and for $\mu = 0, 5, 10$ and 15. We also plot the shape that is obtained for the case where μ is formally infinite, i.e. when D_γ is strictly vanishing (we then use the one-sided model). This situation is at odd to the usual assumption for eutectic growth, and we are not aware of any description of such a steady-state in the literature. Let us note that we have checked that this scenario exists also for off-eutectoid concentration, showing that the existence of the steady-state is not restricted to high symmetry conditions.

On the other hand, since $\rho = 1 + A\mu$, $V - V_{JH}$ varies linearly with μ when $\mu \ll 1$. We exhibit these two linear regimes in Fig. 4.6 where we plot our simulations results (squares) for $V\lambda_e/D_\gamma$ as a function of μ for $\lambda/\lambda_e = 1$ and 2. We see that close to the origin we may approximate our results by the straight solid lines, and, that this

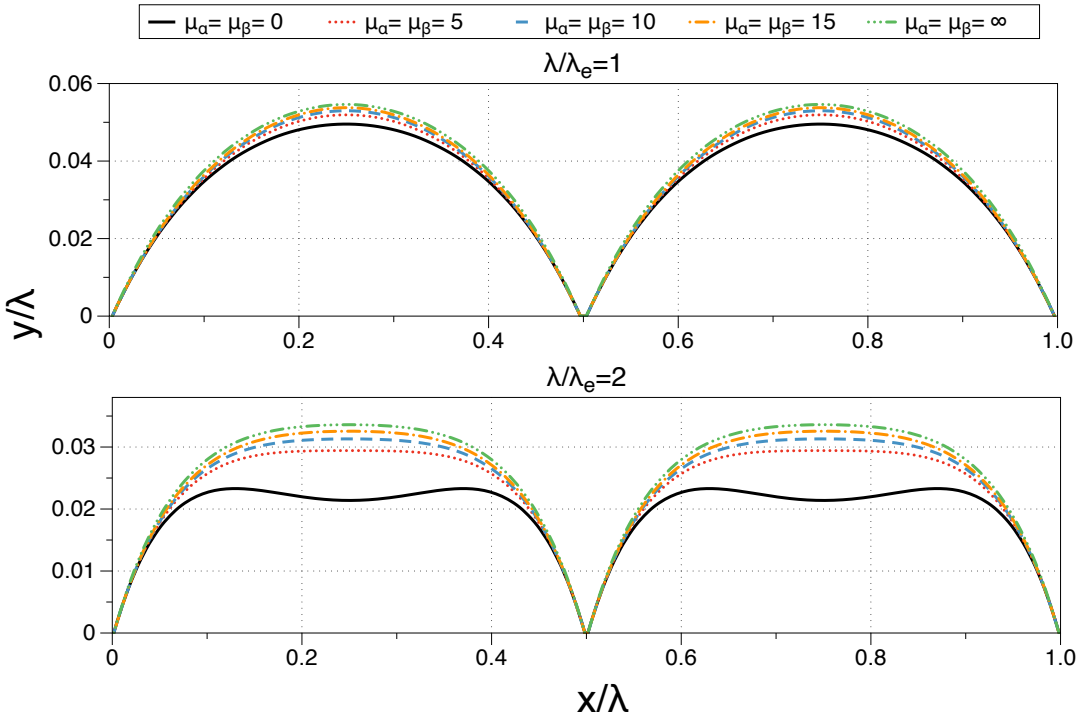

Figure 4.5: The scaled shapes of the growth fronts extracted from the NPF simulation results for $\mu_\alpha = \mu_\beta = 0, 5, 10, 15, \infty$ and $\lambda/\lambda_e = 1, 2$.

linear regime actually extends to values of μ of order unity. As mentioned before, the diffusivity ratio μ may not be too small due to the stability constraints. Moreover, small μ simulations show minor inaccuracies owing to the sharp variations across the interface of the function that allows for elimination of surface diffusion h_i. Note that a tensorial diffusivity [174] has been proposed as an alternative to h_i in Ref. [175], and according to the authors no constraint on the diffusivity ratio then exists.

Complementary, when μ is large enough, our results are well approximated by the dashed straight lines. In the same plot in Fig. 4.6, we also display the results (crosses) that one obtains for the classical PF model (CPF). We see that the larger μ the larger the discrepancy between the NPF and CPF models, indicating the importance of the cross coupling terms parametrized by $M(\vec{\phi})$.

4.3.3 Influence of the different diffusivity ratios of growing phases on the lamellar growth patterns at eutectoid and off-eutectoid composition

Let us now investigate the situation where the three diffusion coefficients are different, i.e. $\mu_\alpha \neq \mu_\beta$ (here all cross coupling terms M_{ij} are thus non-vanishing and surface diffusion should be eliminated at each interface, i.e. all values ϱ_{ij} should be adjusted).

We first perform simulations at $c_\infty = 0$ and $\lambda/\lambda_e = 1$. In Fig. 4.7, we present $\tilde{V}$ for $\mu_\beta \leq \mu_\alpha$ (owing to the choice $c_\infty = 0$, the velocity is invariant under an exchange of μ_α and μ_β). The coefficient A in the expression for ρ is the same as in the previous study, i.e. $\rho = 1 + 0.8924(\mu_\alpha + \mu_\beta)/2$. The dashed line represents the

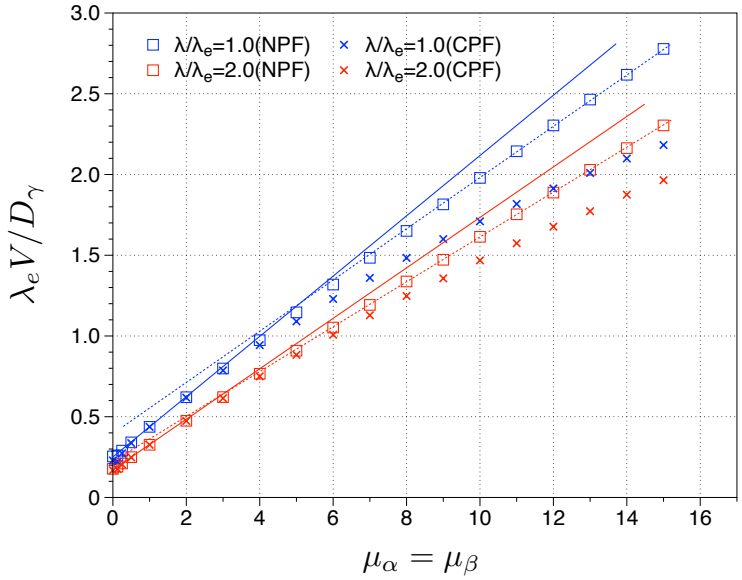

Figure 4.6: Dimensionless velocity obtained with the non-diagonal PF model (NPF, squares) and the classical PF model (CPF, crosses) as a function of the diffusion coefficient in the growing phases $\mu_\alpha = \mu_\beta$ for two different lamellar spacings $\lambda/\lambda_e = 1$ and 2. The solid lines illustrate the small μ linear regime for which the steady-state velocity is proportional to the diffusion coefficient in the mother phase γ and the dashed lines illustrate the large μ linear regime for which the velocity scales as the diffusion coefficient in the growing phases.

results corresponding to $\mu_\alpha = \mu_\beta$. Again, we observe some scattering of the results showing that $\tilde{V}$ is not strictly independent of ρ. However, the amplitude of this scattering, that reaches at most around 30% for $\mu_\beta = 1$, is still much smaller than the variation of ρ, demonstrating that Eq. (4.72) is able to predict quite faithfully the steady-state velocity as a function of μ_α and μ_β.

Even though $c_\infty = 0$, the pattern is non-symmetric due to the choice $\mu_\alpha \neq \mu_\beta$. In particular, as can be seen in Fig. 4.7b – e, where we present the interfaces shapes for different ratios μ_β/μ_α and $\mu_\alpha = 10$, the α/β interface forms a finite angle with the vertical direction, and we denote it as θ at the triple junction. In Fig. 4.7f, we plot θ (in degrees) as a function of μ_β ($1 \leq \mu_\beta \leq 10$) for $\mu_\alpha = 10$. It decreases when μ_β increases and vanishes at $\mu_\beta = \mu_\alpha$ as expected for a fully symmetric pattern.

Let us now investigate a case where the composition is off-eutectoid, i.e. $c_\infty = 0.1$. Then $\eta = 0.4$ and $\rho = 1 + A(0.4\mu_\alpha + 0.6\mu_\beta)$. Here, the best fit to our simulation results for $\mu_\alpha = \mu_\beta = 1$ gives $A = 0.8989$. We use this value to calculate the rescaled dimensionless velocity $\tilde{V}$, and we plot the latter in Fig. 4.8 for different μ_α and μ_β. While the dashed line corresponds to the fit providing A, we see again a scattering of the simulations results, with a small enough amplitude that validates the scaling $V \sim \rho$. In opposition to the case $c_\infty = 0$, i.e. $\eta = 0.5$, the α/β interface is vertical only when $\mu_\alpha = \mu_\beta = 0$. This is indeed the usual assumption when one studies eutectic growth within the one-sided model at arbitrary global composition [176]. However, as soon as the diffusion coefficient in the growing phases is finite, the α/β interface becomes curved. Noticeably, when $\mu_\alpha = \mu_\beta$, the width of the lamella with the larger (smaller) phase fraction, here β (α), is larger (smaller) at the triple junction than at equilibrium, i.e. far behind the triple junction. This

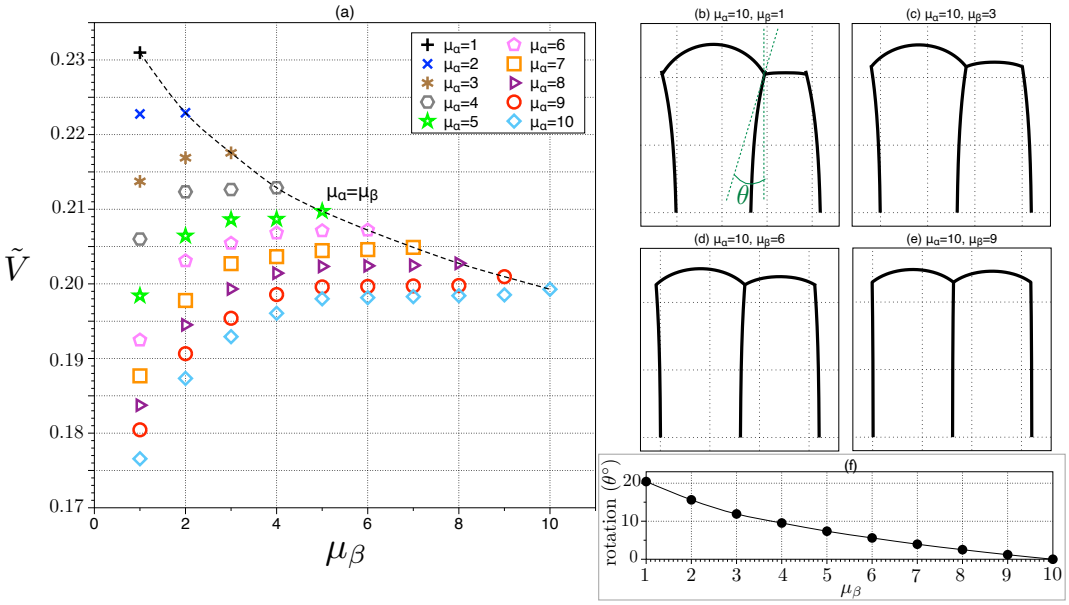

Figure 4.7: (a) Rescaled dimensionless growth velocities obtained from NPF simulations during isothermal transformation at eutectoid composition and $\lambda = \lambda_e$, with unequal μ_α and μ_β (the dashed line corresponds to $\mu_\alpha = \mu_\beta$). (b)-(j) shows the alteration of the lamellar shapes extracted from NPF results for $\mu_\alpha = 10$, $\mu_\beta = 1$ to 9, respectively. (k) the rotation angle (θ) of the triple junction in (b)-(j).

yields a rotation of the triple junction. This rotation is further accentuated when $\mu_\beta > \mu_\alpha$, and in opposition, when $\mu_\beta < \mu_\alpha$, the sign of the rotation angle is opposite.

Until now it was proposed that the scatter observed for $\tilde{V}$ in our results, i.e. in Figs. 4.4, 4.7, and 4.8, is due to the inaccuracy of the theory developed in Ref. [152]. However, it should be verified that this scatter is not instead related to interfacial effects, that are eliminated with different choices of parameters when μ_α and μ_β change. Therefore, here, we finally perform a convergence study with respect to $\tilde{d}/W$. For a sake of generality, we choose the asymmetric situation where $c_\infty = 0$, $\mu_\alpha = 10$ and $\mu_\beta = 3$. This corresponds to a result presented in Fig. 4.7, more precisely the third blue diamond when starting from the left. In Fig. 4.9, we present the convergence of $\tilde{V}$ when $\tilde{d}/W$ increases, i.e. when the interface width W decreases. At the interface width used in Fig. 4.7 (and also in Figs. 4.4 and 4.8), i.e. for the encircled data point at $\tilde{d}/W = 0.5$, a 2% error on $\tilde{V}$ is found (compared to the converged value), which is quite satisfactory. This supports that the scatter observed in our results is indeed due to the, small but still existing, inaccuracy of the theory developed in Ref. [152].

4.4 Summary

In this chapter, we have developed a quantitative non-diagonal phase field model for three-phase transformations, such as eutectic and eutectoid. In the latter case, the diffusion coefficient in the growing phases D_α and D_β are of the same order as the diffusion coefficient in the mother phase D_γ, and a kinetic cross coupling between the diffusion field and the phase fields is thus required. Special attention is paid

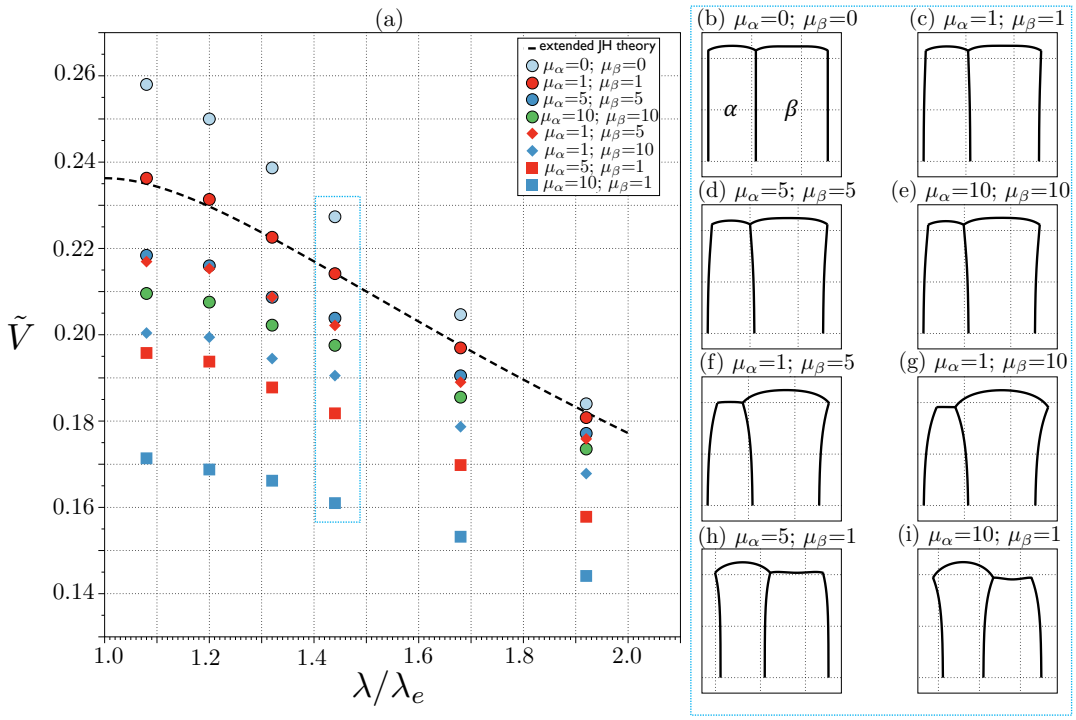

Figure 4.8: (a) Rescaled dimensionless growth velocities obtained from NPF simulations at off-eutectoid composition for different μ_α and μ_β. (b)-(i) shows the alteration of the lamellar shapes extracted from NPF simulations for $\lambda/\lambda_e = 1.44$.

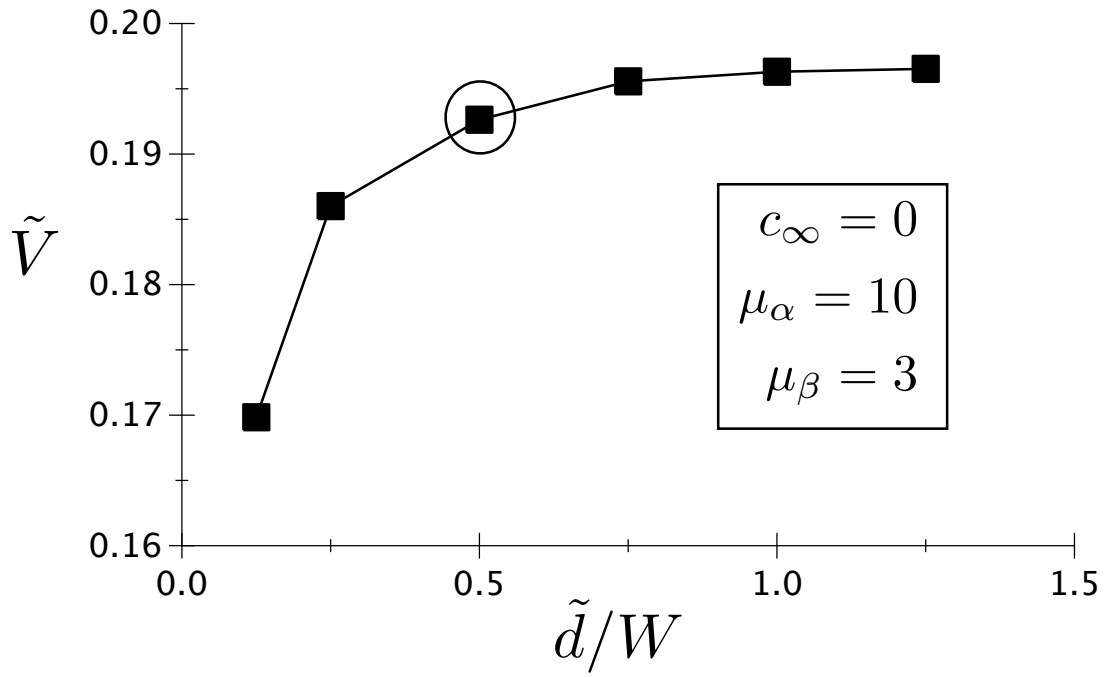

Figure 4.9: Convergence study with the interface width W for a situation corresponding to Fig. 4.7, i.e. $c_\infty = 0, \mu_\alpha = 10, \mu_\beta = 3$. The encircled data point for $\tilde{d}/W = 0.5$, that corresponds to the interface width used in Fig. 4.7 (and also in Figs. 4.4 and 4.8), shows a 2% error compared to the converged value of $\tilde{V}$, which is quite satisfactory.

to the elimination of all abnormal interface effects that arise when analyzing the thin-interface limit of the model.

First, we have benchmarked our model against phase field and boundary integral results from Ref. [86] in the one-sided case (when $D_\alpha = D_\beta = 0$). Second, we have performed simulations in the two-sided case where D_α and D_β are non-negligible. We evidence the relevance of the scaling law suggested in Ref. [152] for the steady-state velocity as a function of the ratio of diffusion coefficients. We observe the two limiting cases, i.e. the classical one for which diffusion is mainly present in the mother phase due to $D_\alpha, D_\beta \ll D_\gamma$, and the one for which diffusion is mainly present in the growing phases due to $D_\alpha, D_\beta \gg D_\gamma$. In both the one- and two-sided cases we verify the necessity of using a non-diagonal phase field model, i.e. having a kinetic cross coupling, for quantitative simulations.

In the present work, the influence of the bulk diffusion in the growing phase has been investigated. During eutectoid transformations such as the pearlite transformation, not only bulk diffusion in the growing ferrite but also surface diffusion are believed to play a crucial role. The non-diagonal phase field model provides the possibility to tune the surface diffusion coefficient, while eliminating other kinetic effects such as solute trapping. Thus, it may be a potential tool for a future study of the pearlite transformation at steady-state and the divorced pearlite microstructure [177, 178] with the consideration of all possible diffusion paths. In this regard, the complex thermodynamics of pearlite may necessitate the usage of a phase field model based on a grand-potential formulation [105], which is pursued in the following chapter.

Chapter 5

Pearlite transformation

The pearlitic microstructure in steels, typically consisting of alternating lamellae of ferrite (α) and cementite (θ) formed through the eutectoid reaction from the austenite (γ), is of considerable importance and technological interest due to its high strength and good ductility. During the pearlite transformation, the cooperative growth velocity of ferrite and cementite is controlled by carbon diffusion and the possible diffusion pathways are volume diffusion (diffusion in γ phase), bulk diffusion (diffusion in α phase) and interface diffusion (diffusion along γ/α and γ/θ interfaces). The Zener-Hillert theory firstly predicted the stable growth velocity of pearlite during isothermal transformation for a given undercooling and lamellar spacing. However, the predictions showed a large discrepancy to the experimental observations, as aforementioned in Section 2.6.1. For accurate predictions of the kinetics during the pearlite transformation, interface diffusion and bulk diffusion mechanisms are also proposed as possible dominant diffusion paths to narrow the gap between theoretical predictions and experimental results.

The aim of the chapter is to study the influence of different diffusion paths on the pearlite transformation in a quantitative way. In this chapter, the derivation of the grand potential based nondiagonal three-phase field model is presented in Section 5.1.1. Then, the procedure of linking the phase field parameters with free boundary conditions is depicted in section 5.1.2. Since the surface diffusion plays a crucial role during pearlite growth, the method to tune the surface diffusion in the simulations is described in section 5.1.3. Subsequently, the simulations are performed for five different cases by using the grand potential based nondiagonal phase field model. The corresponding simulation parameters and results are elucidated in section 5.2 and section 5.3, respectively. Finally, the conclusion of this chapter is presented in section 5.4.

5.1 Grand potential based nondiagonal phase field model

The free energy based nondiagonal three-phase field model presented in chapter 4 is restricted to simple symmetric phase diagrams. For example, the concentration difference in the parent phase is reproduced well, whereas it can not be tuned flexibly in the growing phases. In this section, to reproduce the complex thermodynamics of phase transformations, such as pearlite transformation, a new nondiagonal three-

phase field model is derived based on a grand potential formulation in analogy to Ref. [105].

5.1.1 Time evolution equations

Firstly, three phase field order parameters are defined as ϕ_i $(i = \alpha, \beta, \gamma)$ to distinguish the different bulk phases α, β and γ. Then, a binary alloy is a mixture of two pure substances A and B. B is considered as the solvent. The number density of A atoms related to the local concentration of A atoms, C_a, is defined as

$$\rho = \frac{C_a}{V_a}, \tag{5.1}$$

where V_a is the atomic volume and we assume that A atoms occupy the same atomic volume as the B atoms. The number density is a conserved field, which obeys

$$\dot{\rho} = -\boldsymbol{\nabla} \cdot \mathbf{J}, \tag{5.2}$$

with $\mathbf{J}$ being the mass flux. In anology to free energy functional, the grand potential functional is [105]

$$\begin{aligned} \Omega &= \int_V (\omega_{grad} + \omega_{tw} + \omega_{chem})\, \mathrm{d}V \\ &= \int_V \left\{ \frac{HW^2}{2} \sum_{i=\alpha,\beta,\gamma} (\boldsymbol{\nabla}\phi_i)^2 + H \sum_{i=\alpha,\beta,\gamma} \phi_i^2(1-\phi_i)^2 + \sum_{i=\alpha,\beta,\gamma} g_i(\phi)\omega_i(\mu) \right\}, \end{aligned} \tag{5.3}$$

which consists of three parts. The first part indicates the gradient energy term, in which W is the interface thickness. The second part is the triple well potential, which is constructed as the sum of double-well potential of all phase fields. The parameter H determines the height of the triple well potential. The last term presents the grand potential density of different bulk phases, in which $g_i(\phi)$ is the interpolation function and $\omega_i(\mu)$ is

$$\omega_i(\mu) = f_i - \mu\rho, \tag{5.4}$$

where f_i is the Helmholtz free energy of phase i, and μ is the chemical potential of B atom. At here, a parabolic free energy function is used for f_i, i.e., $f_i = 1/2\epsilon_i(c - c_i^{eq})^2 + f_i^0$, where f_i^0 is the minimum value of the parabolic free energy function, which is dependent on temperature. Then, the chemical potential is $\mu = \partial f_i/\partial\rho = V_a\epsilon_i(c - c_i^{eq})$, the concentration has the formulation $c = \mu/(V_a\epsilon_i) + c_0^{eq}$ and $\omega_i(\mu)$ can be expressed as $\omega_i(\mu) = -1/2\mu^2/(V_a^2\epsilon_i) - \mu/V_a c_0^{eq}$. Besides, $g_i(\phi)$ is a fifth order interpolation function as defined in Ref. [86] to avoid the appearance of spurious third phase contributions in a two phase interface. It can be written as

$$g_i(\phi) = \frac{\phi_i^2}{4}\left\{15(1-\phi_i)\left[1 + \phi_i - (\phi_k - \phi_j)^2\right] + \phi_i\left(9\phi_i^2 - 5\right)\right\}, \tag{5.5}$$

for a two phase interface, such as an i/j interface, $g_i(\phi)$ reduces to $p(\phi)$

$$p(\phi) = \phi^3(10 - 15\phi + 6\phi^2). \tag{5.6}$$

According to the Onsager relations and the free energy based nondiagonal three-phase field model presented in Ref. [173], we write down the formulation of the

grand potential based nondiagonal phase field equations in the following variational form:

$$-\frac{\delta\Omega}{\delta\phi_i}\bigg|_{\sum\phi_j=1} = \tau\left(\phi\right)\dot{\phi}_i + M\left(\phi\right) W\boldsymbol{\nabla}\phi_i|_{\sum\phi_j=1}\cdot\mathbf{J}, \tag{5.7}$$

$$\boldsymbol{\nabla}\frac{\delta\Omega}{\delta\mu} = \sum_i M\left(\phi\right) W\boldsymbol{\nabla}\ \phi_i|_{\sum\phi_j=1}\dot{\phi}_i + \frac{\mathbf{J}}{D\left(\phi\right)}, \tag{5.8}$$

where $\tau(\phi)$ is the relaxation time, $M(\phi)$ is the cross-coupling term that can be tuned to present the free boundary conditions, $D(\phi)$ is the diffusion coefficient. To fulfill the constraint $\sum_i \phi_i = 1$, a Lagrange multiplier is introduced in the grand potential functional, which yields

$$\frac{\delta\Omega}{\delta\phi_i}\bigg|_{\sum\phi_n=1} = \frac{2}{3}\frac{\delta\Omega}{\delta\phi_i} - \frac{1}{3}\frac{\delta\Omega}{\delta\phi_j} - \frac{1}{3}\frac{\delta\Omega}{\delta\phi_k}, \tag{5.9}$$

$$\boldsymbol{\nabla}\phi_i|_{\sum\phi_n=1} = \frac{2}{3}\boldsymbol{\nabla}\phi_i - \frac{1}{3}\boldsymbol{\nabla}\phi_j - \frac{1}{3}\boldsymbol{\nabla}\phi_k. \tag{5.10}$$

We should note here that each driving force of the phase fields in Eq. (5.7) is coupled to the conjugate flux $\dot{\phi}_i$ through the relaxation time $\tau(\phi)$ and cross-coupled to the diffusion flux J through the cross coupling term $M(\phi)$. As mentioned in Refs. [108, 109], the cross-coupling term only exist in the interface region as it is defined as the gradient of the phase fields. Similarly, the diffusion driving force is coupled to the conjugate diffusion flux $\mathbf{J}$ through the diffusivity $D(\phi)$ and coupled to the fluxes $\dot{\phi}_\alpha$, $\dot{\phi}_\beta$ and $\dot{\phi}_\gamma$. Moreover, after omitting the cross-coupling term in Eq. (5.7), the phase field model does not obey Onsager's relations and becomes identical to the quantitative phase field model in Ref. [85] with anti-trapping current. To be consistent with the nonequilibrium thermodynamics, we can write down the explicit form of Eqs. (5.7) and (5.8) by using a matrix inversion

$$\begin{bmatrix} \dot{\phi}_\alpha \\ \dot{\phi}_\beta \\ \dot{\phi}_\gamma \end{bmatrix} = \begin{bmatrix} P_{\alpha\alpha} & P_{\alpha\beta} & P_{\alpha\gamma} \\ P_{\beta\alpha} & P_{\beta\beta} & P_{\beta\gamma} \\ P_{\gamma\alpha} & P_{\gamma\beta} & P_{\gamma\gamma} \end{bmatrix}^{-1} \begin{bmatrix} Q_\alpha \\ Q_\beta \\ Q_\gamma \end{bmatrix} \tag{5.11}$$

where, for $i \neq j$,

$$P_{ii} = \tau - D\left[MW\boldsymbol{\nabla}\phi_i|_{\sum\boldsymbol{\phi_n}=1}\right]^2, \tag{5.12}$$

$$P_{ij} = -DM^2W^2\boldsymbol{\nabla}\phi_i|_{\sum\boldsymbol{\phi_n}=1}\cdot\boldsymbol{\nabla}\phi_j|_{\sum\boldsymbol{\phi_n}=1}, \tag{5.13}$$

$$Q_i = -\frac{\delta\Omega}{\delta\phi_i}\bigg|_{\sum\boldsymbol{\phi_n}=1} + DMW\chi\boldsymbol{\nabla}\phi_i|_{\sum\boldsymbol{\phi_n}=1}\cdot\boldsymbol{\nabla}\mu, \tag{5.14}$$

where χ is the susceptibility, which is defined as [105]

$$\chi = \frac{\partial\rho}{\partial\mu}. \tag{5.15}$$

Furthermore,

$$
\begin{aligned}
-\left.\frac{\delta\Omega}{\delta\phi_i}\right|_{\sum\phi_n=1} &= HW^2\boldsymbol{\nabla}^2\phi_i - \frac{2H}{3}\Big[2\phi_i(1-\phi_i)(1-2\phi_i) \\
&\quad -\phi_j(1-\phi_j)(1-2\phi_j) - \phi_k(1-\phi_k)(1-2\phi_k)\Big] \\
&\quad +\omega_i(\frac{2}{3}\frac{\partial g_i}{\partial\phi_i} - \frac{1}{3}\frac{\partial g_i}{\partial\phi_j} - \frac{1}{3}\frac{\partial g_i}{\partial\phi_k}) \\
&\quad +\omega_j(\frac{2}{3}\frac{\partial g_j}{\partial\phi_i} - \frac{1}{3}\frac{\partial g_j}{\partial\phi_j} - \frac{1}{3}\frac{\partial g_j}{\partial\phi_k}) \\
&\quad +\omega_k(\frac{2}{3}\frac{\partial g_k}{\partial\phi_i} - \frac{1}{3}\frac{\partial g_k}{\partial\phi_j} - \frac{1}{3}\frac{\partial g_k}{\partial\phi_k})
\end{aligned} \tag{5.16}
$$

and

$$
\frac{\partial g_i}{\partial\phi_i} = \frac{15\phi_i}{4}\left[(3\phi_i+2)(1-\phi_i)^2 + (3\phi_i-2)(\phi_j-\phi_k)^2\right], \tag{5.17}
$$

$$
\frac{\partial g_i}{\partial\phi_j} = -\frac{\partial g_i}{\partial\phi_k} = \frac{15}{2}\phi_i^2(1-\phi_i)(\phi_k-\phi_j). \tag{5.18}
$$

For the chemical potential, we have

$$
\dot{\mu} = \frac{1}{\chi}\left\{\boldsymbol{\nabla}\left[D(\phi)\chi\nabla\mu + J_{at}\right] - \sum_{i=\alpha,\beta,\gamma}\frac{\partial\rho}{\partial\phi}\dot{\phi}_i\right\}, \tag{5.19}
$$

where

$$
J_{at} = \sum_{i=\alpha,\beta,\gamma} D(\phi)M(\phi)W\boldsymbol{\nabla}\ \phi_i|_{\sum\phi_j=1}, \tag{5.20}
$$

and

$$
\rho = -\frac{\delta\Omega}{\delta\mu} = -g_i(\phi)\frac{\partial\omega_i}{\partial\mu} - g_j(\phi)\frac{\partial\omega_j}{\partial\mu} - g_k(\phi)\frac{\partial\omega_k}{\partial\mu}. \tag{5.21}
$$

The interface dissipation of the grand potential based nondiagonal phase field model can be expressed as

$$
\begin{aligned}
\dot{S} &= \int_V \mathrm{d}V\left(-\left.\frac{\delta\Omega}{\delta\phi_\alpha}\right|_{\sum\boldsymbol{\phi}=1}\dot{\phi}_\alpha - \left.\frac{\delta\Omega}{\delta\phi_\beta}\right|_{\sum\boldsymbol{\phi}=1}\dot{\phi}_\beta - \left.\frac{\delta\Omega}{\delta\phi_\gamma}\right|_{\sum\boldsymbol{\phi}=1}\dot{\phi}_\gamma + \vec{\nabla}\frac{\delta\Omega}{\delta\mu}\cdot\vec{J}\right) \\
&= \int_V \mathrm{d}V\left\{\tau(\phi)\left[\left(\dot{\phi_\alpha}\right)^2 + \left(\dot{\phi_\beta}\right)^2 + \left(\dot{\phi_\gamma}\right)^2\right] + 2M(\phi)W\left(\left.\vec{\nabla}\phi_\alpha\right|_{\sum\phi_i=1}\dot{\phi}_\alpha\right.\right. \\
&\quad \left.\left. + \left.\vec{\nabla}\phi_\beta\right|_{\sum\phi_i=1}\dot{\phi}_\beta + \left.\vec{\nabla}\phi_\gamma\right|_{\sum\phi_i=1}\dot{\phi}_\gamma\right)\cdot\vec{J} + \frac{\vec{J}^2}{D(\phi)}\right\}.
\end{aligned} \tag{5.22}
$$

At equilibrium between two phases, such as an i/j interface, the one-dimensional phase field profile reads

$$
\phi_{eq}(x) = \frac{1}{2}\left[1 - \tanh\left(\frac{x}{\sqrt{2}W}\right)\right], \tag{5.23}
$$

and the equilibrium number density file reads

$$
\rho_{eq}(x) = \frac{\rho_{ij}^0 + \rho_{ji}^0}{2} + \frac{\rho_{ij}^0 - \rho_{ji}^0}{2}\big\{2p[\phi_{eq}(x)] - 1\big\}. \tag{5.24}
$$

5.1.2 Link with free-boundary description

In this section, we present how to reproduce the desired boundary conditions through appropriately choosing the parameters of the grand potential based nondiagonal phase field model with or without surface diffusion for different interface thickness. Firstly, the mass conservation equation of atoms A and B at a liquid/solid interface between phase i and j reads

$$D_i \boldsymbol{\nabla}\rho|_i \cdot \mathbf{n} + V\rho_{ij}^0 = D_j \boldsymbol{\nabla}\rho|_j \cdot \mathbf{n} + V\rho_{ji}^0 = J_A, \tag{5.25}$$

with V being the total normal flux of all atoms through the interface and J_A being the normal flux of atoms A through the interface. The detailed explanation of Eq. (5.25) can be found in Section 4.1.3. We should note that the surface diffusion is neglected in Eq. (5.25), since it is negligible at a liquid/solid interface. However, at a solid/solid interface, surface diffusion plays more crucial role than bulk diffusion or volume diffusion due to the interface defects. Therefore, with the consideration of surface diffusion, the tangential surface diffusion takes part in the solute transportation along the interface, the corresponding mass conservation equation is modified to

$$D_i \boldsymbol{\nabla}\rho|_i \cdot \mathbf{n} + V\rho_{ij}^0 + WD_{surf}\nabla_S^2\rho_{inter} = D_j \boldsymbol{\nabla}\rho|_j \cdot \mathbf{n} + V\rho_{ji}^0, \tag{5.26}$$

where D_{surf} is the surface diffusion coefficient and will be elaborated in Section 5.1.3.

Together with the mass conservation law, the aforementioned fluxes V and J_A linearly relate to the grand potential jump $\delta\Omega$ and chemical potential jump $\delta\mu$ (diffusion potential) by using an Onsager matrix. When surface diffusion is negligible, the kinetic boundary conditions are identical to Eqs. (4.32) and (4.33). Although the mass conservation law is modified while considering the surface diffusion, it does not change the kinetic boundary conditions based on Onsager relations, since the normal fluxes V and J_A are perpendicular to the tangential surface diffusion. Thus, for the two different cases, the kinetic boundary conditions are

$$\delta\Omega = \bar{\mathcal{A}}V + \bar{\mathcal{B}}J_A + d_0\kappa, \tag{5.27}$$

$$\delta u = \bar{\mathcal{B}}V + \bar{\mathcal{C}}J_A, \tag{5.28}$$

where $\bar{\mathcal{A}}$, $\bar{\mathcal{B}}$, $\bar{\mathcal{C}}$ are the kinetic coefficients of the 2×2 Onsager matrix, d_0 is the capillary length, κ is the curature of the interface. At weak out-of-equilibrium boundary conditions, we can write down the formation of $\delta\Omega$ and $\delta\mu$ [108, 173]

$$\delta\Omega = f_j''(c_{ji}^0)\rho_{ji}^0(\rho_{ji} - \rho_{ji}^0)/V_a^2 - f_i''(c_{ij}^0)\rho_{ij}^0(\rho_{ij} - \rho_{ij}^0)/V_a^2, \tag{5.29}$$

$$\delta\mu = f_j''(c_{ji}^0)(\rho_{ji} - \rho_{ji}^0)/V_a - f_i''(c_{ij}^0)(\rho_{ij} - \rho_{ij}^0)/V_a, \tag{5.30}$$

where $f_i(c)$ and $f_j(c)$ are the free energy functions of i and j phases, respectively. c_{ij}^0 and c_{ji}^0 are the equilibrium concentrations in phase i and j, while c_{ij} and c_{ji} are the interface concentrations. To achieve equilibrium boundary conditions, the grand potential and diffusion potential jumps are eliminated, i.e. $\delta\Omega = \delta\mu = 0$. Thus, Eq. (5.29) is rewritted as

$$\delta\Omega = f_j''(c_{ji}^0)(\rho_{ji} - \rho_{ji}^0)(\rho_{ji}^0 - \rho_{ij}^0)/V_a^2 = f_i''(c_{ij}^0)(\rho_{ij} - \rho_{ij}^0)(\rho_{ji}^0 - \rho_{ij}^0)/V_a^2, \tag{5.31}$$

and the Gibbs-Thomson relation is

$$(\rho_{ji} - \rho_{ji}^0)f_j''(c_{ji}^0)/f_i''(c_{ji}^0) = (\rho_{ij} - \rho_{ij}^0) = -\tilde{d}\kappa, \tag{5.32}$$

where

$$\tilde{d} = \frac{d_0 V_a^2}{(\rho_{ij}^0 - \rho_{ji}^0) f_i''(c_{ji}^0)}. \tag{5.33}$$

According to the derivation in Refs. [108], the expression of $\bar{\mathcal{A}}$, $\bar{\mathcal{B}}$ and $\bar{\mathcal{C}}$ with respect to equilibrium phase field properties are

$$\begin{aligned}
\bar{\mathcal{A}} &= 2\int_{-\infty}^{\infty} \tau[\phi_{eq}'(x)]^2 \mathrm{d}x - 4\int_{-\infty}^{\infty} \left\{ MW[\phi_{eq}'(x)]^2 \rho_{eq}(x) \right\} \mathrm{d}x \\
&\quad + \int_{-\infty}^{\infty} \left\{ \frac{\rho_{eq}^2(x)}{D} - \frac{(\rho_{ij}^0)^2}{2D_i} - \frac{(\rho_{ji}^0)^2}{2D_j} \right\} \mathrm{d}x, \qquad (5.34) \\
\bar{\mathcal{B}} &= 2\int_{-\infty}^{\infty} \left\{ MW[\phi_{eq}'(x)]^2 \right\} \mathrm{d}x - \int_{-\infty}^{\infty} \left\{ \frac{\rho_{eq}(x)}{D} - \frac{\rho_{ij}^0}{2D_i} - \frac{\rho_{ji}^0}{2D_j} \right\} \mathrm{d}x, \qquad (5.35) \\
\bar{\mathcal{C}} &= \int_{-\infty}^{\infty} \left\{ \frac{1}{D} - \frac{1}{2D_i} - \frac{1}{2D_j} \right\} \mathrm{d}x. \qquad (5.36)
\end{aligned}$$

To determine the kinetic coefficients of the Onsager matrix, the expressions for $\tau(\phi)$, $M(\phi)$ and $D(\phi)$ need to be specified. Here, we have chosen the following forms

$$\tau(\phi) = \frac{\tau_{ij}\phi_i\phi_j + \tau_{ik}\phi_i\phi_k + \tau_{jk}\phi_j\phi_k}{\phi_i\phi_j + \phi_i\phi_k + \phi_j\phi_k}, \tag{5.37}$$

$$M(\phi) = \frac{M_{ij}\phi_i\phi_j + M_{ik}\phi_i\phi_k + M_{jk}\phi_j\phi_k}{\phi_i\phi_j + \phi_i\phi_k + \phi_j\phi_k}. \tag{5.38}$$

We should note that $\tau(\phi)$ and $M(\phi)$ are only meaningful in the interface region. For example, at a binary i/j interface, $\tau(\phi)$ and $M(\phi)$ are constants, i.e., τ_{ij}, M_{ij}, while in a triple junction, $\tau(\phi)$ and $M(\phi)$ are dependent on the phase field order parameters. However, these expressions are not suitable for bulk phases due to $\phi_i\phi_j + \phi_i\phi_k + \phi_j\phi_k = 0$. Thus, the average values $(\tau_{ij} + \tau_{ik} + \tau_{jk})/3$ and $(M_{ij} + M_{ik} + M_{jk})/3$ are defined as the relaxation time and cross-coupling coefficient in the bulk phases. It is noted at here that this approximation has only a slight influence on the phase field simulation results.

Furthermore, for the diffusion function $D(\phi)$, not only the diffusion coefficients of the different bulk phases but also the surface diffusion should be reproduced. As shown in Ref. [173], the diffusion function can be defined as

$$\frac{1}{D(\vec{\phi})} = \frac{1}{3} \sum_{i=\alpha,\beta,\gamma} \left\{ \frac{1}{D_i} + h_i(\vec{\phi}) \left(\frac{1}{D_i} - \frac{1}{2D_j} - \frac{1}{2D_k} \right) \right\}, \tag{5.39}$$

where

$$h_i(\vec{\phi}) = (2\phi_i - 1)(1 + 4a_{ij}\phi_i\phi_j + 4a_{ik}\phi_i\phi_k). \tag{5.40}$$

We define three additional parameters a_{ij} to tune the desired surface diffusion. The procedure to determine phase field paramters τ_{ij}, M_{ij} and a_{ij} have been described in Ref. [173]. For a binary i/j interface, the kinetic coefficients are

$$\begin{aligned}
\bar{\mathcal{A}} &= \frac{2\Phi\tau_{ij}}{W} - \frac{\zeta(\rho_{ij}^0 - \rho_{ji}^0)^2}{4} \left(\frac{W}{2D_i} + \frac{W}{2D_j} \right), \qquad (5.41) \\
\bar{\mathcal{B}} &= 2\Phi M_{ij} - \frac{\varrho_{ij}(\rho_{ji}^0 - \rho_{ij}^0)}{2} \left(\frac{W}{2D_i} - \frac{W}{2D_j} \right), \qquad (5.42) \\
\bar{\mathcal{C}} &= 0, \qquad (5.43)
\end{aligned}$$

where

$$\Phi = W \int_{-\infty}^{\infty} [\phi'_{eq}]^2 \mathrm{d}x \approx 0.23570, \tag{5.44}$$

$$\zeta = \frac{1}{W} \int_{-\infty}^{\infty} \Big(1 - \{2p[\phi_{eq}] - 1\}^2\Big) \mathrm{d}x \approx 1.40748, \tag{5.45}$$

$$\varrho_{ij} = \frac{1}{W} \int_{-\infty}^{\infty} \Big(1 - \big(2p[\phi_{eq}] - 1\big) h_{i/j}(\phi_{eq})\Big) \mathrm{d}x. \tag{5.46}$$

As mentioned in Section 4.1.3, $\bar{\mathcal{C}}$ automatically vanishes due to the oddness of $h_{i/j}(\phi_{eq})$. To achieve equilibrium boundary conditions, i.e., $\delta\Omega = \delta\mu = 0$, $\bar{\mathcal{A}} = \bar{\mathcal{B}} = 0$ is also required. Thus, we can obtain the expressions of τ_{ij} and M_{ij}

$$\tau_{ij} = \frac{\zeta(\rho^0_{ij} - \rho^0_{ji})^2 W^2}{8\Phi} \left(\frac{1}{2D_i} + \frac{1}{2D_j}\right), \tag{5.47}$$

$$M_{ij} = \frac{\varrho_{ij}(\rho^0_{ji} - \rho^0_{ij})}{4\Phi} \left(\frac{W}{2D_i} - \frac{W}{2D_j}\right). \tag{5.48}$$

When the diffusion coefficients in the growing α and β phases are negligible, i.e. $D_\alpha, D_\beta \ll D_\gamma$, we have

$$\tau_{\alpha\beta} = M_{\alpha\beta} = 0, \tag{5.49}$$

$$D(\phi) = D_\gamma(1 - \phi_\alpha - \phi_\beta). \tag{5.50}$$

Consequently, the kinetic boundary conditions become [108, 173]

$$\delta\Omega = (\bar{\mathcal{A}} + \rho^0_{j\gamma}\bar{\mathcal{B}})V + d_0\kappa, \tag{5.51}$$

$$\delta\mu = (\bar{\mathcal{B}} + \rho^0_{i\gamma}\bar{\mathcal{C}})V. \tag{5.52}$$

Then, the equilibrium boundary conditions require $\bar{\mathcal{A}} + \rho^0_{i\gamma}\bar{\mathcal{B}} = 0$ and $\bar{\mathcal{B}} + \rho^0_{i\gamma}\bar{\mathcal{C}} = 0$, which yields

$$\tau_{i\gamma} = \frac{(\rho^0_{\gamma i} - \rho^0_{i\gamma})^2 W^2 \xi}{8\Phi D_\gamma}, \tag{5.53}$$

$$M_{i\gamma} = \frac{(\rho^0_{\gamma j} - \rho^0_{j\gamma}) W \kappa}{4\Phi D_\gamma}, \tag{5.54}$$

where

$$\kappa = \frac{1}{W} \int_{-\infty}^{\infty} \frac{\phi_{eq} + 1 - 2p[\phi_{eq}]}{1 - \phi_{eq}} \mathrm{d}x \approx 2.12132, \tag{5.55}$$

$$\xi = \frac{1}{W} \int_{-\infty}^{\infty} \frac{1 - (2p[\phi_{eq}] - 1)^2}{1 - \phi_{eq}} \mathrm{d}x \approx 3.42778. \tag{5.56}$$

As mentioned above, we consider the diffusion in all three phases (two-sided case), diffusion in the parent phase only (one-sided case) The corresponding phase field parameters are determined to reproduce the equilibrium boundary conditions. However, there is another case during the three phase transformation when the diffusion of only one of the growing phases is negligible ($D_\beta \ll D_\gamma, D_\alpha$). The corresponding kinetic boundary conditions for α/γ interface are described in Eqs. (5.27) and (5.28). Similarly, the corresponding kinetic boundary conditions for β/γ and

α/β interfaces are described in Eqs. (5.51) and (5.52). To reproduce the equilibrium boundary conditions in the third case, we propose a new diffusion coefficient expression

$$D(\phi) = \frac{2D_\gamma D_\alpha(1-\phi_\beta)(1+a_{\beta\gamma}\phi_\beta\phi_\gamma)(1+a_{\alpha\beta}\phi_\alpha\phi_\beta)}{D_\gamma + D_\alpha + (\phi_\gamma - \phi_\alpha)(1+4a_{\alpha\gamma}\phi_\alpha\phi_\gamma)(D_\alpha - D_\gamma)}. \tag{5.57}$$

In analogy to the two-sided case, three parameters $a_{\alpha\gamma}$, $a_{\beta\gamma}$ and $a_{\alpha\beta}$ are chosen to tune the surface diffusion at α/γ, β/γ and α/β interfaces. For an α/γ interface, where $\phi_\alpha = 1-\phi_\gamma$ and $\phi_\beta = 0$, the diffusion expression Eq. (5.57) becomes

$$\frac{1}{D_{\alpha/\gamma}(\phi)} = \frac{1}{2D_\gamma} + \frac{1}{2D_\alpha} + h_{\alpha/\gamma}(\phi)\left(\frac{1}{2D_\gamma} - \frac{1}{2D_\alpha}\right). \tag{5.58}$$

In order to reproduce equilibrium boundary conditions at an α/γ interface, we obtain the expression for $\tau_{\alpha/\gamma}$ and $M_{\alpha/\gamma}$ according to Eqs. (5.47) and (5.48),

$$\tau_{\alpha/\gamma} = \frac{\zeta(\rho^0_{\alpha/\gamma} - \rho^0_{\gamma/\alpha})^2 W^2}{8\Phi}\left(\frac{1}{2D_\alpha} + \frac{1}{2D_\gamma}\right), \tag{5.59}$$

$$M_{\alpha/\gamma} = \frac{\varrho_{\alpha/\gamma}(\rho^0_{\gamma/\alpha} - \rho^0_{\alpha/\gamma})}{4\Phi}\left(\frac{W}{2D_\alpha} - \frac{W}{2D_\gamma}\right). \tag{5.60}$$

For a binary i/β interface ($i = \alpha, \gamma$), where $\phi_i = 1-\phi_\beta$ and $D_\beta \ll D_i$, the diffusion coefficient in Eq. (5.57) becomes

$$D_{i/\beta}(\phi_i) = 2D_i\frac{\phi_i[1+a_{i\beta}\phi_i(1-\phi_i)]}{(1+\mu)+\phi_i(1-\mu)}, \tag{5.61}$$

with $\mu = D_\alpha/D_\gamma$. In analogy to Eqs. (5.53) and (5.54), we can write down the expressions for $\tau_{i\beta}$ and $M_{i\beta}$ to eliminate the grand potential and diffusion potential jump in Eqs. (5.51) and (5.52)

$$\tau_{i\beta} = \frac{(\rho^0_{i\beta} - \rho^0_{\beta i})^2 W^2 \xi_1}{8\Phi D_i}, \tag{5.62}$$

$$M_{i\beta} = \frac{(\rho^0_{i\beta} - \rho^0_{\beta i}) W \kappa_1}{4\Phi D_i}, \tag{5.63}$$

where

$$\kappa_1 = \frac{1}{W}\int_{-\infty}^{\infty}\left\{\frac{2-2p[\phi_{eq}]}{D_{i\beta}(\phi_i)/D_i} - 1\right\}\mathrm{d}x, \tag{5.64}$$

$$\xi_1 = \frac{1}{W}\int_{-\infty}^{\infty}\frac{1-(2p[\phi_{eq}]-1)^2}{D_{i\beta}(\phi_i)/D_i}\mathrm{d}x. \tag{5.65}$$

Different from Eqs. (5.55) and (5.56), we should note that κ_1 and ξ_1 are dependent on $\mu = D_\alpha/D_\gamma$ instead of being constants.

5.1.3 Surface diffusion

In the previous section, we have presented the procedure of determination of parameters in $\tau(\phi)$, $M(\phi)$ and $D(\phi)$ to eliminate the grand potential and diffusion potential jumps and reproduce equilibrium boundary conditions. In chapter 4, the parameters a_{ij} were chosen to vanish surface diffusion. However, in solid-solid transformations, the surface diffusion is typically not negligible. As mentioned above, the tangential surface diffusion is perpendicular to the normal flux V and J_A, which modifies the mass conservation law rather than kinetic bounary conditions. In the following, we explain how to tune the surface diffusion in our model.

For a binary i/j interface, D_i and D_j are the diffusivities of i and j grains or phases. The interface between i and j is an area with a defined width δ, in which the diffusivity usually has a constant value D_{inter} and significantly differs from D_i and D_j. Hence, a diffusivity jump appears at the sharp interface area. In contrast, a diffuse interface is used in the phase field method and the diffusivity curve varies smoothly between two bulk phases. To relate the two situations, the surface diffusion is defined as the total excess diffusivity with regard to the bulk values and calculated by the integral

$$D_{surf} = D_{inter}\delta = \int_{-\infty}^{\infty} [D(\phi) - \frac{1}{2}D_i - \frac{1}{2}D_j]\mathrm{d}x. \tag{5.66}$$

When $D_j \ll D_i$ in the one-sided case, D_{surf} is

$$D_{surf} = D_{inter}\delta = \int_{-\infty}^{\infty} [D(\phi) - \frac{1}{2}D_i]\mathrm{d}x. \tag{5.67}$$

To incorporate the surface diffusion into the diffusion expression $D(\phi)$, on the one hand, an additional term is introduced in $D(\phi)$ in the one-sided case to enhance the diffusivity at interface region. Thus, $D(\phi)$ is defined as

$$D(\phi) = D_i\phi_i + 4D^{ij}_{inter}\phi_i\phi_j. \tag{5.68}$$

The corresponding surface diffusion becomes

$$D_{surf} = \int_{-\infty}^{\infty} (4D^{ij}_{inter}\phi_i\phi_j)\mathrm{d}x = 2\sqrt{2}D^{ij}_{inter}W. \tag{5.69}$$

On the other hand, when $D(\phi)$ is chosen as Eqs. (5.39) and (5.57), one method to obtain the desired surface diffusion is tuning the parameter a_{ij}. An increase of a_{ij} leads to larger surface diffusion. However, a_{ij} has a upper limit which depends on the diffusion ratios of i and j phases since the positiveness of the dissipation should be obeyed.

Subsequently, the grand potential and diffusion potential difference have to be eliminated to reproduce the equilibrium boundary conditions when the surface diffusion exists. For instance, the desired surface diffusion coefficient at a binary i/j interface is obtained by using a new a_{ij} in the two-sided case. Since the parameters Φ, ζ and τ_{ij} in Eqs. (5.44), (5.45) and (5.47) are independent of a_{ij}, they do not need to be recalculated. However, ϱ_{ij} is a function of a_{ij}. A new ϱ_{ij} is calculated by integrating Eq. (5.46). The corresponding cross-coupling term M_{ij} is obtained by using Eq. (5.48). In the one-sided case, an expression for the diffusion coefficient

functions is given by Eq. (5.68). The integrals of κ and ξ in Eqs. (5.55) and (5.56) become

$$\kappa_{surf} = \frac{1}{W}\int_{-\infty}^{\infty} \frac{2 - 2p[\phi_{eq}]}{\phi_i + 4D^{ij}_{inter}/D_i\phi_i(1-\phi_i)}\mathrm{d}x, \tag{5.70}$$

$$\xi_{surf} = \frac{1}{W}\int_{-\infty}^{\infty} \frac{1 - (2p[\phi_{eq}] - 1)^2}{\phi_i + 4D^{ij}_{inter}/D_i\phi_i(1-\phi_i)}\mathrm{d}x. \tag{5.71}$$

When the surface diffusion is considered the in one-sided case, the parameters κ and ξ have new expressions. After integrating Eqs. (5.70) and (5.71), the corresponding values, τ_{ij} and M_{ij}, can be obtained by using Eqs. (5.53) and (5.54). Furthermore, to maintain the stability of nondiagonal phase field, the constraint $D_{inter}/D_i < 0.875$ needs to be satisfied.

5.2 Simulation parameters

To investigate the growth kinetics of the pearlite transformation, the alloy Fe-3.44%atC is chosen and simulated by the presented grand-potential based non-diagonal phase field model. At this composition, the pearlite directly forms from the austenite phase. The linearized phase diagram of Fe-C for the simulations is illustrated in Fig. 5.1. The chosen thermodynamic and kinetic parameters and the simulations parameters are listed in Table 5.1 and Table 5.2, respectively. The free energy densities of γ, α and θ phases are plotted in Fig. 5.2. As shown in Fig. 5.2, the curvature of the cementite free energy parabola is much larger than for austenite and ferrite, the produced concentration gradient in cementite is closed to 0. In two-dimensional simulations, a pair of lamellae is computed in a rectangular simulation box of total size $n_x \times n_y$ with the grid spacing $\Delta x = \Delta y = 0.4W$ as illustrated in Fig. 5.3, where W is the interface width and equals to unity. For the present simulations, we consider $\sigma_{\alpha\gamma} = \sigma_{\theta\gamma} = \sigma_{\alpha\theta}$. In order to obtain steady state periodic lamellar arrays, periodic boundary conditions are used perpendicular to the growth front, while no-flux boundary conditions are used at the top and bottom sides of the simulation box. The length of n_y is large enough to ensure that the diffusion in the y-direction is not hampered. During the simulations, different diffusion paths are activated in five cases to study the influence of bulk, volume and surface diffusion on the growth kinetics of pearlite transformation. In the cases 1 to 4, we prescribe the capillary length $\widetilde{d}/W = 0.21696, 0.65088, 1.0848$ to obtain the same lamellar spacing at the extreme condition, i.e., $\lambda_e/W = 96$ and $\lambda_m/W = 48$, under the different undercooling 10K, 30K and 50K. In case 5, the capillary length $\widetilde{d}/W = 1.0848$ is used for all the undercoolings 20K, 30K, 40K, 50K and 60K. Also, a moving-frame method and GPU acceleration are applied in the simulations to increase the computational efficiency.

5.3 Results and discussions

Before presenting the simulations of pearlite growth, we make a number of simplifying assumptions:

- We assume that there is no grain boundary segregation (no solute drag effect).

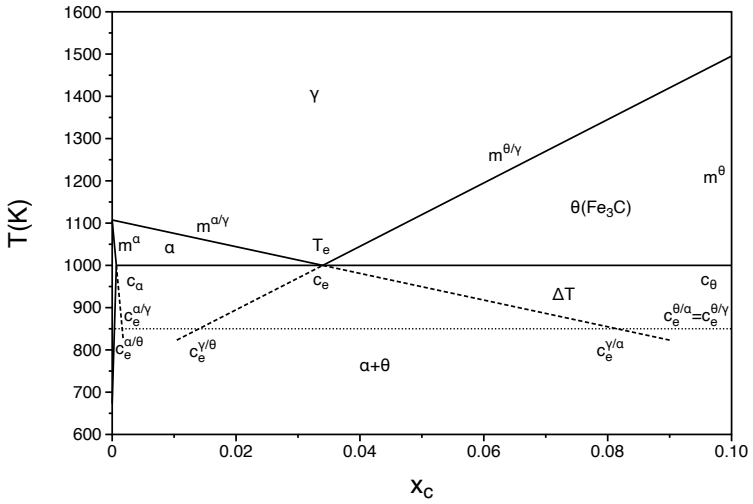

Figure 5.1: Linearized Fe-C eutectoid phase diagram.

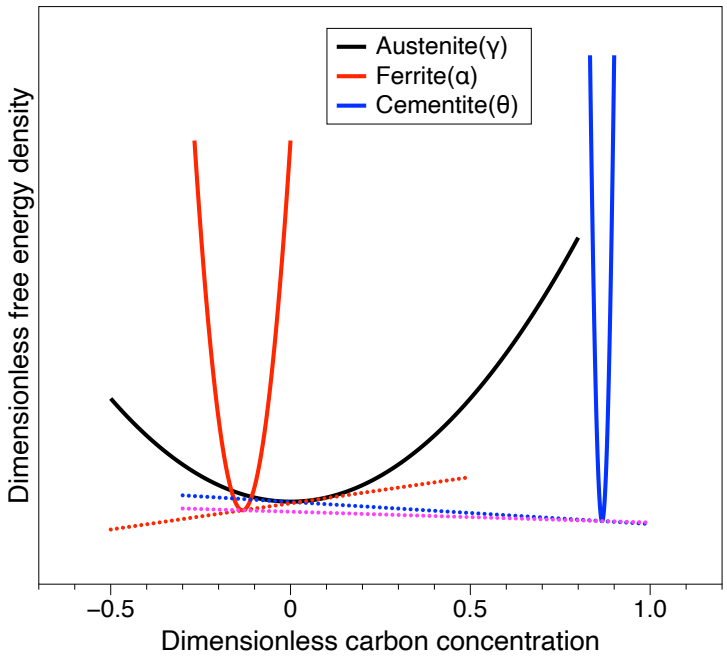

Figure 5.2: Demonstration of parabolic free energy densities of the α, θ and γ phases. Dashed lines depict the common tangent constructions.

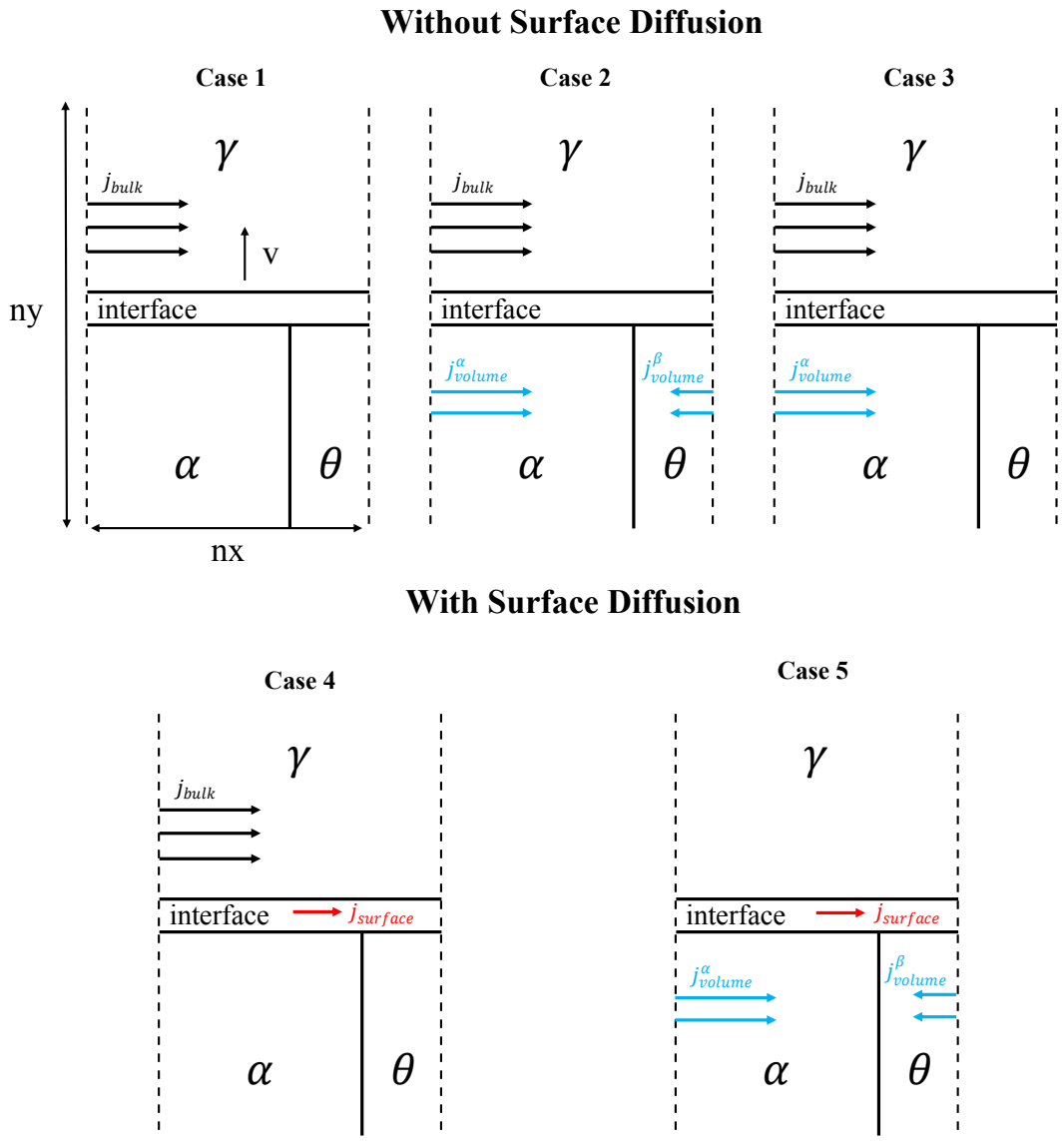

Figure 5.3: Demonstration of the simulation scenarios. In cases 1 to 3, the surface diffusion is eliminated, while case 4 and 5 consider surface diffusion. Case 1 only considers the diffusion in γ phase. Case 2 considers the diffusion in γ, α and θ phases. Case 3 considers the diffusion in γ and α phases. Case 4 considers the diffusion in γ phase and surface diffusion. Case 5 considers the diffusion in α and θ phases and surface diffusion.

Table 5.1: Thermodynamic and kinetic properties of pearlite transformation

Symbol	Definition and units	Value
R	Gas constant (J/(molK))	8.314
T_e	Temperature of the eutectoid point (K)	1000 [150]
c_e	eutectoid composition (mol)	0.034 [150]
c_α	Concentration of α at the eutectoid point (mol)	0.000677 [150]
c_θ	Concentration of θ at the eutectoid point (mol)	0.25 [150]
$m^{\alpha/\gamma}$	Slope of γ/α transformation line (K/mol)	3155 [150]
m^α	Slope of α phase line (K/mol)	158572 [150]
$m^{\theta/\gamma}$	Slope of γ/θ transformation line (K/mol)	-7503 [150]
m^θ	Slope of θ phase line (K/mol)	$-\infty$
D_γ	Diffusion coefficient in γ phase (m^2/s)	$1.5 \times 10^{-5} \exp(-142100/(RT))$[150]
D_α	Diffusion coefficient in α phase (m^2/s)	$2.2 \times 10^{-4} \exp(-122500/(RT))$[150]
D_B	Diffusion coefficient along interface (m^2/s)	$8.51 \times 10^{-5} \exp(-96851/(RT))$[147]
δ	Interface thicknesses of γ/α and γ/θ (nm)	0.25 [179]

Table 5.2: Dimensionless parameters used in the nondiagoanl phase field simulations of the pearlite transformation

Symbol	Definition	Value
W	Interface thickness	1
$\mathrm{d}x = \mathrm{d}y$	grid size	0.4
V_a	Atomic Volume	1
D_γ	diffusion coefficient in γ phase	1
ϵ_γ	parameters of parabolic free energy function of γ phase	1
ϵ_α	parameters of parabolic free energy function of α phase	50.213
ϵ_θ	parameters of parabolic free energy function of α phase	1000
c_γ^{eq}	concentration of γ phase at eutectoid point	0
c_α^{eq}	concentration of α phase at eutectoid point	-0.1336
c_β^{eq}	concentration of β phase at eutectoid point	0.8664

- The diffusivities along γ/α and γ/θ interfaces are assumed to be the same, while the diffusivity along the α/θ interface is not considered (γ is the austenite, α is the ferrite and θ is the cementite).
- Equilibrium boundary conditions at the α/γ, θ/γ and α/θ interfaces are satisfied.

5.3.1 Case 1: diffusion in γ phase

To benchmark the presented grand potential based nondiagonal phase field model in the one-sided case where only the diffusion in γ phase is considered, we compare the growth kinetic of pearlite at steady state obtained from the nondiagonal phase field simulations with the predictions of the Zener-Hillert model under different undercooling $\Delta T = 10K, 30K, 50K$ for different lamellar spacings $\lambda/\lambda_m = 2.667, 3.0, 3.333$. In Ref. [126, 141], the Zener-Hillert model is

$$V_{Zener} = \frac{2D_\gamma}{\eta_\alpha \eta_\theta} \frac{C_e^{\gamma/\alpha} - C_e^{\gamma/\theta}}{C_e^{\theta/\gamma} - C_e^{\alpha/\gamma}} \frac{1}{\lambda} \left(1 - \frac{\lambda_m}{\lambda}\right), \tag{5.72}$$

where V_{Zener} is the growth velocity of the lamellae at steady state, D_γ is the diffusion coefficient in the γ phase, which is defined as unity in phase field simulations. η_α and η_θ are the fractions of α and θ phases. $C_e^{\gamma/\alpha}$, $C_e^{\gamma/\theta}$, $C_e^{\theta/\gamma}$ and $C_e^{\alpha/\gamma}$ are the equilibrium concentrations, which are dependent on temperature. λ is the lamellar spacing, while λ_m denotes minimum spacing when the lamellar growth velocity equals to zero.

In the simulations, the diffusion in α and θ phases and the surface diffusion along α/γ and θ/γ vanish, i.e., $D_\alpha = D_\theta = D_{inter}^{\alpha/\gamma} = D_{inter}^{\theta/\gamma} = 0$. Hence, the growth of pearlite is merely controlled by bulk diffusion in the γ phase. With time, the curvatures of the α/γ and θ/γ interfaces become constant and the growth velocity of pearlite (V_γ) reaches steady-state. The dimensionless growth velocities $V_\gamma\lambda_m/D_\gamma$ obtained from nondiagonal phase field simulations are depicted in Fig. 5.4 together with the predictions of the Zener-Hillert model under given undercooling ΔT= 10K, 20K and 30K. In Fig. 5.4, the solid lines present the dimensionless growth velocities according to Zener-Hillert model, while the points indicate the phase field simulation results. The phase field simulation results lead to a similar relation between growth velocity and lamellar spacing as Zener-Hillert model predicts. However, when the undercooling becomes large, such as 50K, the deviation between nondiagonal phase field simulation results and the predictions of Zener-Hillert model reaches 39%, while it decreases to 18% for $\Delta T = 10K$. As elucidated in Ref. [173], the deviation is caused by the simplification of the Zener-Hillert model rather than the presented phase field model. The lamellar microstructure at steady state is presented in Fig. 5.5 where ΔT = 30K and λ/λ_m = 2.667, 3.0, 3.333. In Fig. 5.5, the curvature of α decreases with the increase of lamellar spacing. Since the diffusion in α and θ is not considered, the $\alpha - \theta$ phase boundaries are perpendicular to the growth front. Overall, the nondiagonal phase field results have a nice agreement with the predictions of the Zener-Hillert model. The larger the lamellar spacing is, the smaller the curvature of α phase is, which reduces the deviation between the simulation results and the predictions of Zener-Hillert model.

5.3.2 Case 2: diffusion in α, θ and γ phases

In this section, we investigate the capabilities of the nondiagonal phase field in the two-sided case where the diffusion in α, θ and γ phases are activated. The diffusion coefficient in γ, α and θ phases are defined as D_γ, D_α and D_θ, respectively. Thus, the ratios between the diffusion coefficients in growing phases and mother phase are prescribed as $\mu_{\alpha/\gamma} = D_\alpha/D_\gamma$, $\mu_{\theta/\gamma} = D_\theta/D_\gamma$. Since new diffusion paths for carbon transportation are introduced, the steady-state growth velocity of pearlite increases. In the work of Ankit et al. [152], an approximate linear relation is obtained to describe the steady-state growth velocity of pearlite, $V_{\gamma+\alpha+\theta}$, through simply combining the diffusion flux in the growing phases with the diffusion flux in the mother phase, which can be written as

$$V_{\gamma+\alpha+\theta} = V_\gamma \rho_{\gamma+\alpha+\theta}, \tag{5.73}$$

where $\rho_{\gamma+\alpha+\theta}$ is a factor depending on the phase diagram parameters, which is given by

$$\rho_{\gamma+\alpha+\theta} = 1 + \frac{m^{\alpha/\gamma}}{m_\alpha}\mu_{\alpha/\gamma}\eta_\alpha + \frac{m^{\theta/\gamma}}{m_\theta}\mu_{\theta/\gamma}\eta_\theta, \tag{5.74}$$

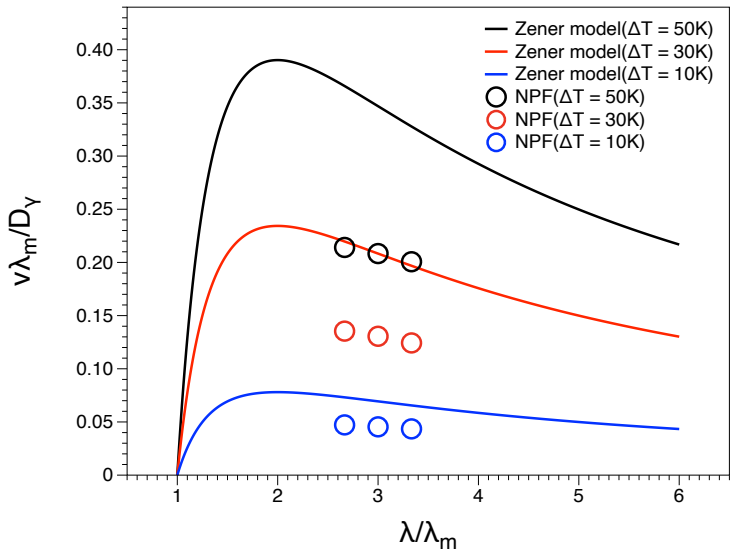

Figure 5.4: Case 1: Comparison between NPF simulation results with the Zener-Hillert theory in the one-sided case with ΔT = 10K, 30K and 50K. The deviation between NPF simulation results and Zener-Hillert calculations is reduced when the undercooling is decreased.

with $m^{\alpha/\gamma}/m^{\alpha}$ = 50.213 and $m^{\theta/\gamma}/m^{\theta}$ = 1000 for pearlite transformation, and η_α, η_θ are the phase fractions of the α and θ phases. The simulation results are illustrated in Fig. 5.6. The dimensionless growth velocities $V_{\gamma+\alpha+\theta}\lambda_e/D_\gamma$ for ΔT= 10K, 30K, 50K and λ/λ_m = 2.667 are presented in Fig. 5.6(a), the points indicate the NPF simulation results, while the dashed lines are fitted lines for $\mu_\alpha = \mu_\theta > 0$. The nondiagonal phase field simulation results show perfect linear relations. Small deviations between simulation results for $\mu_\alpha = \mu_\theta = 0$ (case 1) and the fitted dashed lines may be caused by the two different diffusivity functions used in case 1 and 2. However, the deviation becomes smaller when the undercooling is decreased. Then, the velocity ratios $V_{\gamma+\alpha+\theta}/V_\gamma$ obtained from NPF simulations are compared with Ankit's model, which is shown in Fig. 5.6(b). The NPF simulation results agree well with the calculation of Ankit's model, and the ratios are independent of the undercooling. The deviation is smaller than 7%, which is caused by the lower growth velocity for $\mu_\alpha = \mu_\theta = 0$ as mentioned above. Furthermore, the lamellar microstructure is presented in Fig. 5.7 for $\Delta T = 30K$, $\lambda/\lambda_m = 2.667$ and $\mu_{\alpha/\gamma} = \mu_{\theta/\gamma}$ = 1, 5, 10, 15. In contrast to case 1, the solute can be transported inside the α phase due to the concentration gradient and absorbed by the θ phase in case 2. Therefore, the thickening and tapering of cementite is observed near the growth front, which agrees with the observations in Ref. [150, 152].

Moreover, in the two-sided case, lamellar growth can be controlled by bulk diffusion (diffusion in γ phase) or volume diffusion (diffusion in α and θ phases) by choosing different diffusion ratios. For the pearlite transformation, the concentration gradients in the α and θ phases are much smaller than in the γ phase, i.e. $\nabla c_\theta \ll \nabla c_\alpha \ll \nabla c_\gamma$, which can be easily found from the Fe-C phase diagram. The growth velocity ratios $(V(\mu_\alpha = \mu_\theta = 15)/V(\mu_\alpha = \mu_\theta = 0))$ is smaller than 1.4, while these values are larger than 5 for the symmetric phase diagram as shown in Fig. 4.6 in Chapter 4. Consequently, the growth velocity of the lamellae is controlled not

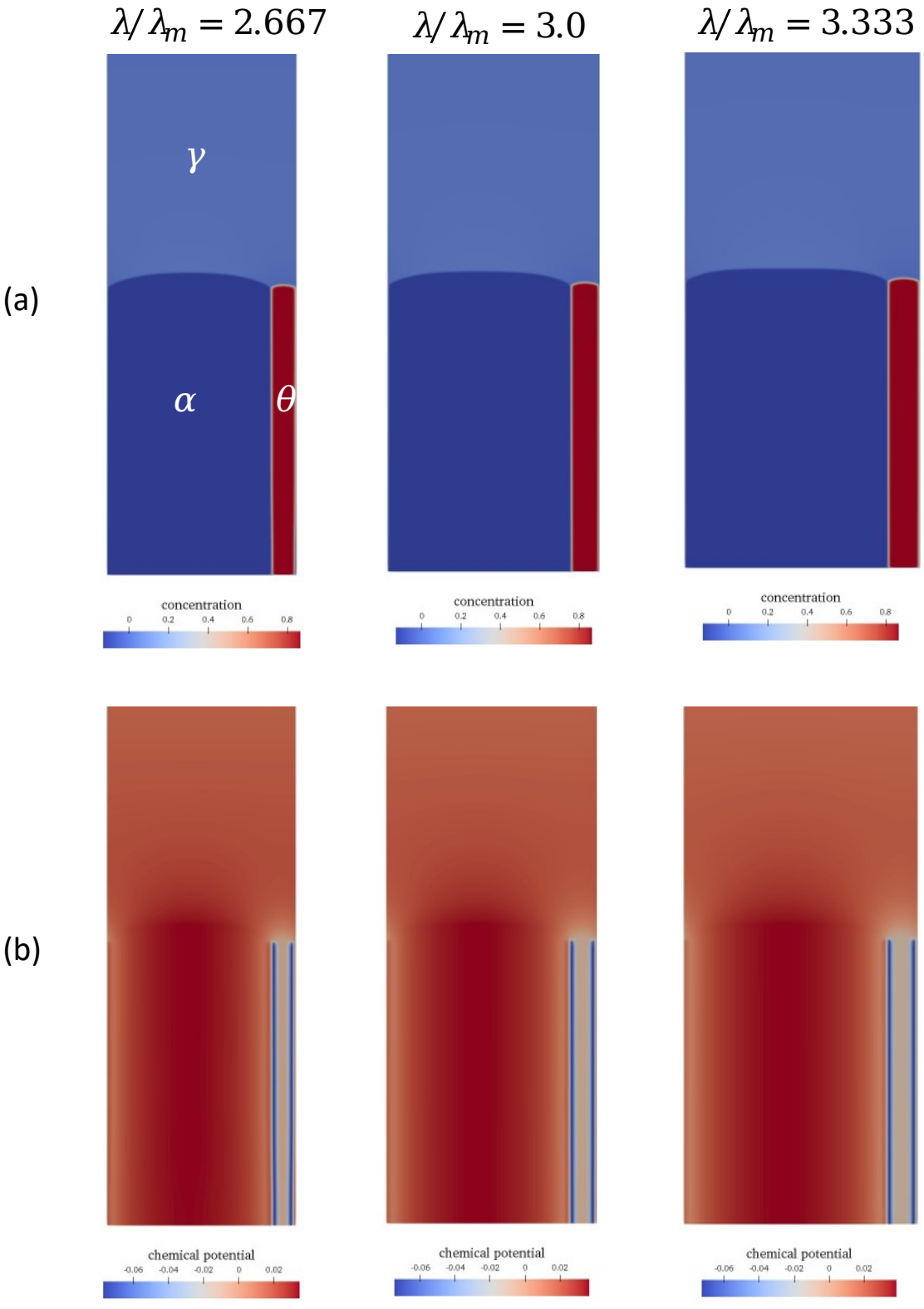

Figure 5.5: Demonstration of the lamellar microstructure as obtained from nondiagonal phase field simulations in case 1 with $\Delta T = 30$K and $\lambda/\lambda_m = 2.667$, 3.0, 3.333. Figure (a) is the concentration field. Figure (b) is the chemical potential field. The curvature of the α phase decreases when the lamellar spacing increases.

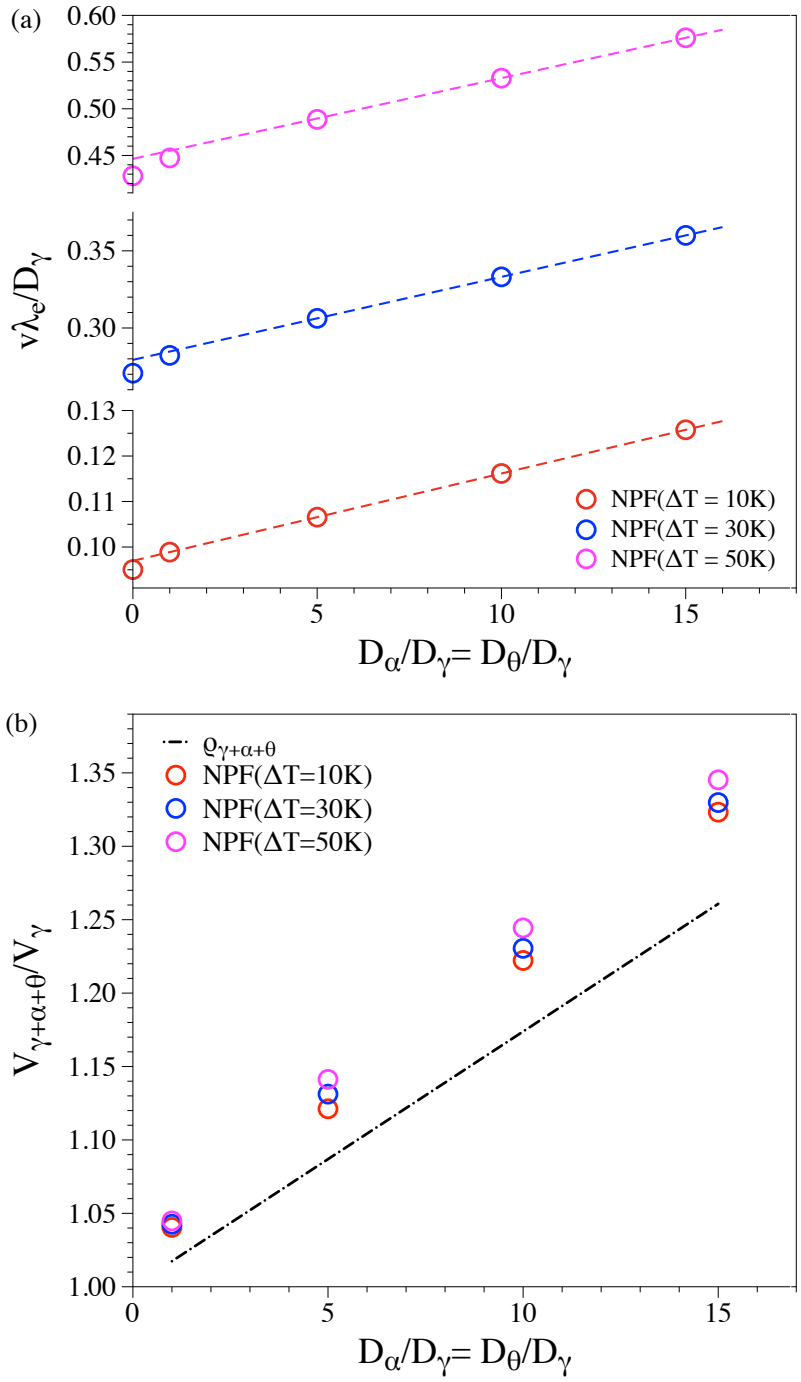

Figure 5.6: Case 2: Panel (a) indicates that the nondiagonal phase field (NPF) simulation results show a perfect linear relation for different undercoolings, i.e., ΔT = 10K, 30K and 50K with $\lambda/\lambda_e = 2.667$. Points are nondiagonal phase field simulation results, while the dashed lines are fitted lines by using the simulation results. The deviation between the growth velocity in one-sided case ($V(\mu_{\alpha/\gamma} = \mu_{\alpha/\gamma} = 0)$) and the fitted lines is narrowed when the undercooling decreases. Figure (b) demonstrates the comparison between velocity ratios ($V_{\gamma+\alpha+\theta}/V_\gamma$) and $\rho_{\gamma+\alpha+\theta}$ calculated by using Eq. (5.74). The largest deviation is smaller than 7%, which implies a good agreement with the predictions by Ankit.

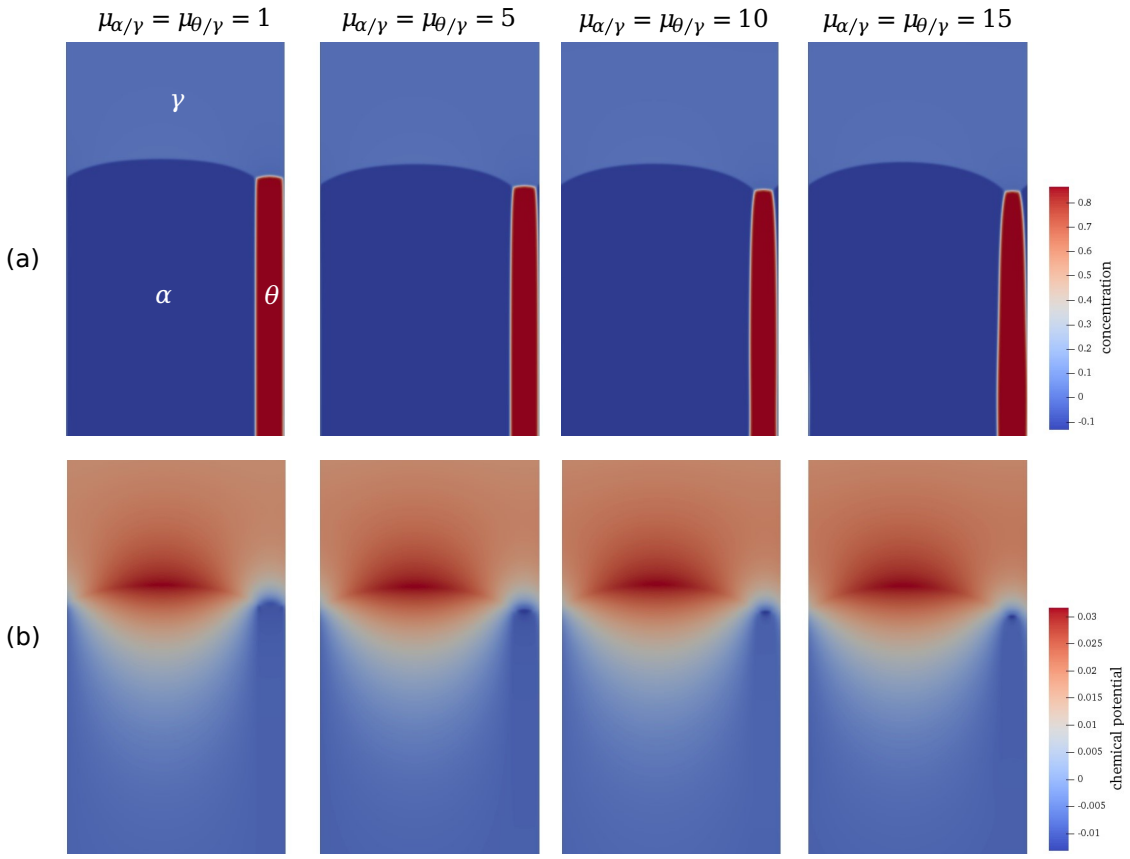

Figure 5.7: Demonstration of the steady state lamellar microstructure obtained from nondiagonal phase field simulations with $\Delta T = 30$K, $\lambda/\lambda_m = 2.667$ and $\mu_{\alpha/\gamma} = \mu_{\theta/\gamma}$ = 1, 5, 10, 15. With the incorporation of diffusion in α and θ phases, thickening and tapering of cementite is observed near the growth front. Figure (a) is the concentration field. Figure (b) is the chemical potential field.

only by the diffusivities but also the concentration gradients in the growing phases in the two-sided case. In the presented simulations, μ_α and μ_θ have to be smaller than 17 to ensure the stability of nondiagonal phase field model. When $\mu_\alpha = \mu_\theta = 15$, the bulk diffusion is more dominant than volume diffusion. The transition from a bulk diffusion dominant growth pattern to a volume diffusion dominant growth pattern is not included in Fig. 5.6. However, the necessity of introducing a crossing-coupling term for volume diffusion dominant growth patterns has already been clarified in Chapter 4. To sum up, Ankit's model is well reproduced by the presented nondiagonal phase field model for diffusion in α, γ and θ phases.

5.3.3 Case 3: diffusion in γ and α phases

Since the θ phase is stoichiometric, the concentration gradient in the θ phase is 0. The solute transportation in the θ phase theoretically vanishes. In this section, we investigate the growth rate of pearlite when the diffusion in θ phase is suppress. Thus, we ignore the diffusion in the θ phase and consider the diffusion in the γ and α phases by using a new diffusion coefficient expression presented in Eq. (5.57). The parameters $a_{\alpha\gamma}$, $a_{\gamma\theta}$, $a_{\alpha\theta}$ in Eq. (5.57) are chosen to tune the surface diffusion at α/γ, γ/θ and α/θ interfaces. Here, the surface diffusion is eliminated. The nondiagonal phase field simulations are carried out for $\Delta T = 30$K, 50K and $\lambda/\lambda_m = 2.667$. The simulation results are presented in Fig. 5.8.

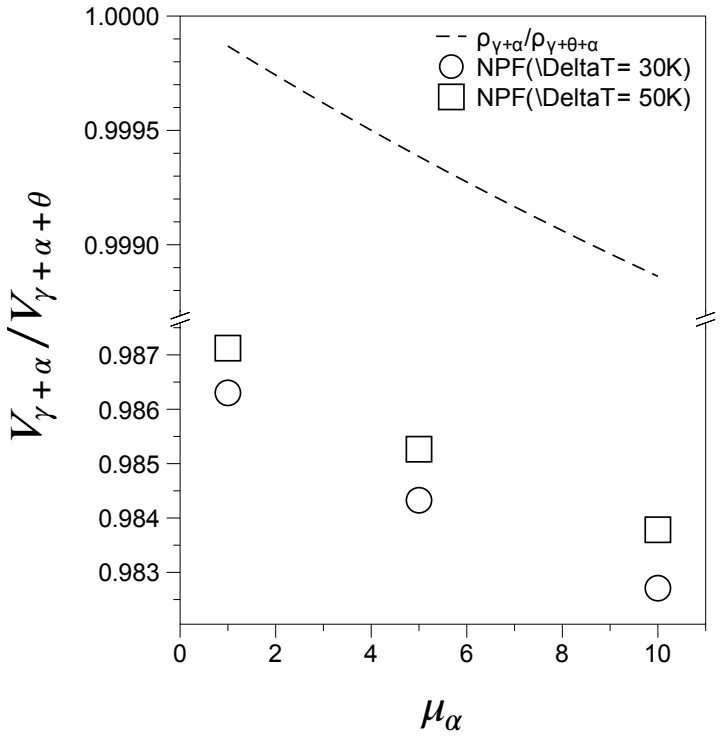

Figure 5.8: Case 3: Demonstration of nondiagonal phase field simulation results with diffusion in α and γ phases for $\lambda/\lambda_m = 2.667$ and $\Delta T = 30$K, 50K. The nondiagonal phase field results and the predictions of Eq. (5.75) both indicate the slight influence of the θ phase on the growth rate of pearlite growth.

We should note that the dashed line in Fig. 5.8 is the calculation of the following

equation

$$\frac{\rho_{\gamma+\alpha}}{\rho_{\gamma+\alpha+\theta}} = \frac{1+\mu_\alpha\eta_\alpha\frac{m^{\alpha/\gamma}}{m_\alpha}}{1+\mu_\alpha\eta_\alpha\frac{m^{\alpha/\gamma}}{m_\alpha}+\mu_\theta\eta_\theta\frac{m^{\theta/\gamma}}{m_\theta}}, \tag{5.75}$$

where $\rho_{\gamma+\alpha}$ indicates the the ratio between the growth velocity when the diffusion in the γ and α phases is considered and the growth velocity in the one-sided case, while $\rho_{\gamma+\alpha+\theta}$ has already been defined in Eq. (5.74). $\rho_{\gamma+\alpha}$ is obtained by omitting the influence of diffusion in the θ phase, i.e., $\mu_\theta\eta_\theta m^{\theta/\gamma}/m_\theta = 0$, which is reasonable for the cementite phase. From the calculation results of Eq. (5.75) for $\mu_\alpha = \mu_\theta \leq 10$, we can see that the difference between $\rho_{\gamma+\alpha}$ and $\rho_{\gamma+\theta+\alpha}$ is less than 0.1%. The nondiagonal phase field simulation results presented by the points in Fig. 5.8 indicate that the difference between $V_{\gamma+\alpha}$ and $V_{\gamma+\alpha+\theta}$ is smaller than 2% when the diffusion in the θ phase is neglected. In one word, the slight difference indicates that diffusion in the θ phase has negligible influence on the growth velocity of pearlite at steady state as expected. The concentration gradient in the θ phase produced by phase field simulation is small enough in the two-side case to transport solute from α phase to θ phase.

Up to here, we have presented the nondiagonal phase field simulation results when the diffusion occurs in (i) γ phase; (ii) α, θ and γ phases; (iii) α and γ phases. In these cases, the free boundary conditions are reproduced and surface diffusion is all eliminated. The agreement between simulation results and the theoretical models, i.e., the Zenner-Hillert model and Ankit's model, illustrates the capabilities of the nondiagonal phase field model and validates the approximations. Then, in the following sections, the influence of surface diffusion is investigated.

5.3.4 Case 4: diffusion in γ phase and along surfaces

In this section, we investigate the influence of the surface diffusion on the growth kinetics of pearlite in the one-sided case. The simulation results are benchmarked with Pandit's model in Ref. [147]. Firstly, the surface diffusion at α/γ and θ/γ interfaces are assumed to have the same value. It is integrated in the simulations by using Eq. (5.68), and the phase dependent diffusion coefficient is

$$D(\phi) = D_\gamma\phi_\gamma + 4D^{\alpha\gamma}_{inter}\phi_\alpha\phi_\gamma + 4D^{\theta\gamma}_{inter}\phi_\theta\phi_\gamma. \tag{5.76}$$

In Ref. [147], the growth velocity with surface diffusion is predicted as

$$V_{\gamma+surf} = \frac{1}{\eta_\alpha\eta_\theta}\frac{C_e^{\gamma/\alpha}-C_e^{\gamma/\theta}}{C_e^{\theta/\gamma}-C_e^{\alpha/\gamma}}\left(2D_\gamma+\frac{12D_B\delta}{\lambda}\right)\frac{1}{\lambda}\left(1-\frac{\lambda_m}{\lambda}\right), \tag{5.77}$$

where D_B is the diffusion coefficient of the α/γ and θ/γ interfaces, δ is the interface width. It has to be clarified that $D_B\delta$ equals to the surface diffusion coefficient D_{surf} in the phase field simulations. Then, the ratio $\rho_{\gamma+surf}$ is defined as $\rho_{\gamma+surf} = V_{\gamma+surf}/V_\gamma$, which can be written as

$$\rho_{\gamma+surf} = 1+\frac{6D_{surf}}{D_\gamma\lambda}. \tag{5.78}$$

We should note that, for given D_γ and λ, $\rho_{\gamma+surf}$ is proportional to D_{surf}. In the present simulations, the interface diffusivities $D^{\alpha\gamma}_{inter}$ and $D^{\theta\gamma}_{inter}$ are chosen as 0.25,

0.5 and 0.75. The corresponding surface diffusion coefficients D_{surf} are $\sqrt{2}/2$, $\sqrt{2}$ and $3\sqrt{2}/2$ according to Eq. (5.69). To link the equilibrium boundary conditions, M and τ are recalculated to eliminate all the abnormal interface effects except the surface diffusion.

We compare the simulation results with cross-coupling term ($M \neq 0$, NPF) and without it ($M = 0$, CPF) for $\Delta T = 10K, 30K, 50K$ and $\lambda/\lambda_m = 2.667$. The comparison results is presented in 5.9(a). In Fig. 5.9(a), the NPF results exhibit a linear relation and the slope is dependent on the temperature, while the CPF results are nonlinear. When the undercooling is increased, ρ obtained from the NPF simulations becomes closer and closer to the analytical calculations of Eq. (5.78). In Ref. [147] (see Figure 4), the diffusion in the γ phase is dominant when the temperature is close to the highest transformation temperature. However, when the undercooling decreases, a transition from γ-dominated to interface-dominated diffusion takes place. Consequently, the ratio of γ diffusion to surface diffusion is converged when the undercooling is continuously decreased. Moreover, when $\lambda/\lambda_e = 1.333$, the NPF simulation results in Fig. 5.9(a) are lower than the calculations of Eq. (5.78).

In Fig. 5.9(b), we plot the curves of ρ versus dimensionless lamellar spacing λ/λ_m obtained from NPF and CPF to investigate the influence of lamellar spacing on the ratio $\rho_{\gamma+surf}$. From the comparison results, the deviation decreases when the lamellar spacing is increased as shown in Fig. 5.9(b). This difference is attributed to the modification of the curvature of lamellar growth fronts. The larger the lamellar spacing is, the smaller is the curvature of growth front is. Therefore, at larger lamellar spacing, the flat growth front leads to the decrease of the deviation between NPF simulation results and $\rho_{\gamma+surf}$.

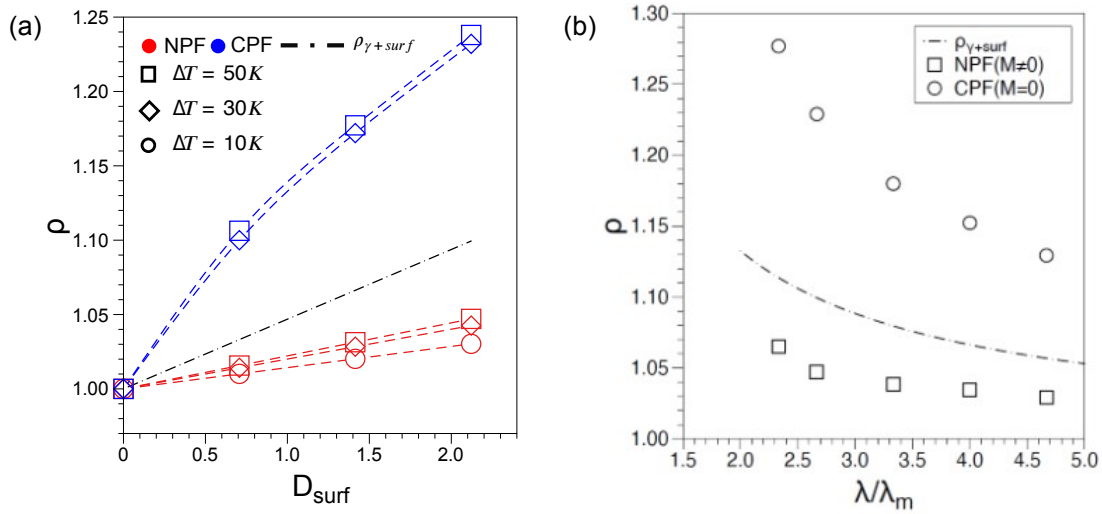

Figure 5.9: Phase field simulation results with diffusion in the γ phase and along surface. Figure (a) depicts the NPF results, CPF results and the predictions of Eq. (5.78) for different undercooling and $\lambda/\lambda_m = 2.667$. Figure (b) demonstrates the NPF results, CPF results and the predictions of Eq. (5.78) for $\Delta T = 50K$ and different lamellar spacings.

In conclusion, the diffusion in the γ phase and along the surface are taken into account in the phase field simulations in this section. For given undercooling and

lamellar spacing, the growth velocities obtained from NPF simulations are proportional to the surface diffusion coefficient, which agrees well the linear relation suggested in Ref. [147]. The higher the undercooling is, the smaller the deviation between the NPF results and the predictions of Pandit's model. Additionally, for given undercooling and surface diffusion coefficient, an increase of the lamellar spacing also decreases the deviation. Furthermore, the comparison between NPF results and CPF results reveals the necessity of introducing the cross-coupling term and elimination of abnormal interface effects.

5.3.5 Case 5: diffusion in α, θ phases and along surfaces

In this section, we reproduce the growth patterns of the pearlite transformation with respect to surface diffusion as well as diffusion in α and θ phase with $\Delta T =$ 20K, 30K, 40K, 50K and 60K and compare the simulation results to experimental observations. On the one hand, the diffusion coefficient of the α phase obtained from Table 5.1 is 160 times larger than of theγ phase. Although the concentration gradient in the α phase is much smaller than in the γ phase, according to the prediction of Ankit's model in Ref. [152], the diffusion in the α phase can approximately enhance the growth velocities of pearlite 4 times. On the other hand, the diffusion in the θ phase has little influence on the growth kinetic of pearlite as aforementioned in Section 5.3.3. Hence, we assume the diffusivities to be identical in the α and θ phases. To obey the stability condition of NPF, i.e., $D_\alpha/D_\gamma < 17$, the diffusion in the γ phase is neglected in the simulations and the one-sided model is used for the nondiagonal phase field simulations. Furthermore, to match the surface diffusion between the experimental calculations and phase field simulations, we define a dimensionless ratio k_{surf}

$$k_{surf} = \frac{D_{inter}\delta}{D_\gamma \lambda_m} = \frac{D_{surf}}{D_\gamma \lambda_m}. \tag{5.79}$$

The experimental data of D_{inter}, δ and D_γ can be obtained from Table 5.1 for different undercoolings. λ_e at 980K, 970K, 960K, 950K and 940K are 0.319μm, 0.215μm, 0.158μm, 0.126μm, 0.104μm, respectively, which are taken from Ref. [150]. Combining these data, we can obtain the corresponding value of k_{surf}, i.e., k_{surf} =2.298, 3.60, 5.20, 6.936, 8.886. For phase field simulation, λ_m/W = 120, 80, 60, 48, 40 at 980K, 970K, 960K, 950K, 940K and the dimensionless average capillary length $\bar{d}/W$ is 1.0848. Then, the corresponding surface diffusion coefficient D_{surf} is obtained by using the same k_{surf}, i.e., D_{surf} = 275.8, 288.1, 311.6, 332.9, 355.5.

First, we simulate the pearlite growth without surface diffusion. Due to the high asymmetry of pearlite ($\eta_\alpha = 6.485\eta_\theta$), the α phase always overgrows the θ phase at different temperatures. The steady state growth velocities cannot be obtained when only volume diffusion is considered. Afterwards, the surface diffusion is added into the simulations. The simulation results are presented in Fig. 5.10. In Fig. 5.10, the relation between the velocity ratios V/V_{Zener} and temperature is investigated. The blue points indicate PF simulation results in Ref. [150], which consider the diffusion in the γ and α phases. The simulation results at $T = 950K$ are 4 times larger than V_{Zener}, whereas they are still much smaller than the experimental observations represented by black points. The red points are the NPF simulation results. From the comparison, we can see that the nondiagonal phase field (NPF) simulation results with the consideration of surface diffusion agree well with the experimental results.

As mentioned in Ref. [147], the surface diffusion is the principle path for solute transport. A similar trend is observed in the simulation results and experimental data. When the temperature increases, the velocity ratio V/V_{Zener} also decreases.

In Fig. 5.11, the pearlite structures at steady state obtained from NPF simulations are presented at T = 970K and 940K. As mentioned above, they fail to obtain the steady state when the diffusion in α and θ phases only is turned on, which implies that the surface diffusion plays a decisive part in pearlite growth. For high temperature, such as T=970K, the tapering and thickening of the θ phase near the growth front is more obvious. They are mitigated for lower temperature, which agree well with the observations that the thickening of cementite is not strong in the experiments [180].

Overall, in this section, we performed nondiagonal phase field simulations to investigate the growth velocities of the pearlite transformation with respect to diffusion in α and γ phases as well as surface diffusion at different temperatures. To reproduce realistic surface diffusion, the surface diffusion coefficients in the simulations are taken from experimental measurements. The agreement between simulation results and experimental results implies the importance of surface diffusion and the quantitative properties of the nondiagonal phase field model. In addition, the tapering and thickening of cementite near the growth front is mitigated by the surface diffusion at lower temperatures.

5.4 Summary

The capabilities of the free energy based nondiagonal phase field model for the two-sided case have been benchmarked in the previous chapters. However, the formation of the free energy demands that the phase diagram has to be symmetric. To break in this restriction, in this chapter, the grand potential based nondiagonal phase field model is developed for complex phase transformation according to Onsager's principles. Then, the presented nondiagonal phase field simulations are carried out for 5 cases to investigate the influence of different diffusion paths on the growth kinetics of pearlite transformation.

When the surface diffusion is eliminated (Case 1 to 3), the nondiagonal phase field simulation results are compared with the Zener-Hillert model in the one-sided case (bulk diffusion) and Ankit's model in the two-sided case (volume diffusion). The agreement between simulation results and theoretical predictions supports the quantitative properties of the nondiagonal phase field model. In Case 3, the diffusion in stoichiometric cementite is eliminated and the simulation results demonstrate that the diffusion in cementite has only slight influence on the pearlite growth. In Case 4, the surface diffusion and diffusion in γ phase are taken into account. The growth velocities of the lamellae are proportional to the surface diffusion coefficient, which agrees well with Pandit's model. The comparison between simulations results ($M \neq 0$) and without ($M = 0$) cross-coupling term evidences the importance for introducing the cross-coupling term. In Case 5, the diffusion in α and θ phases and surface diffusion are considered. Through matching the same surface diffusion between experiments and phase field simulations for different undercoolings, the growth velocities obtained by the nondiagonal phase field model show a convincing agreement with experimental observations.

In conclusion, the capabilities of the grand potential based nondiagonal phase

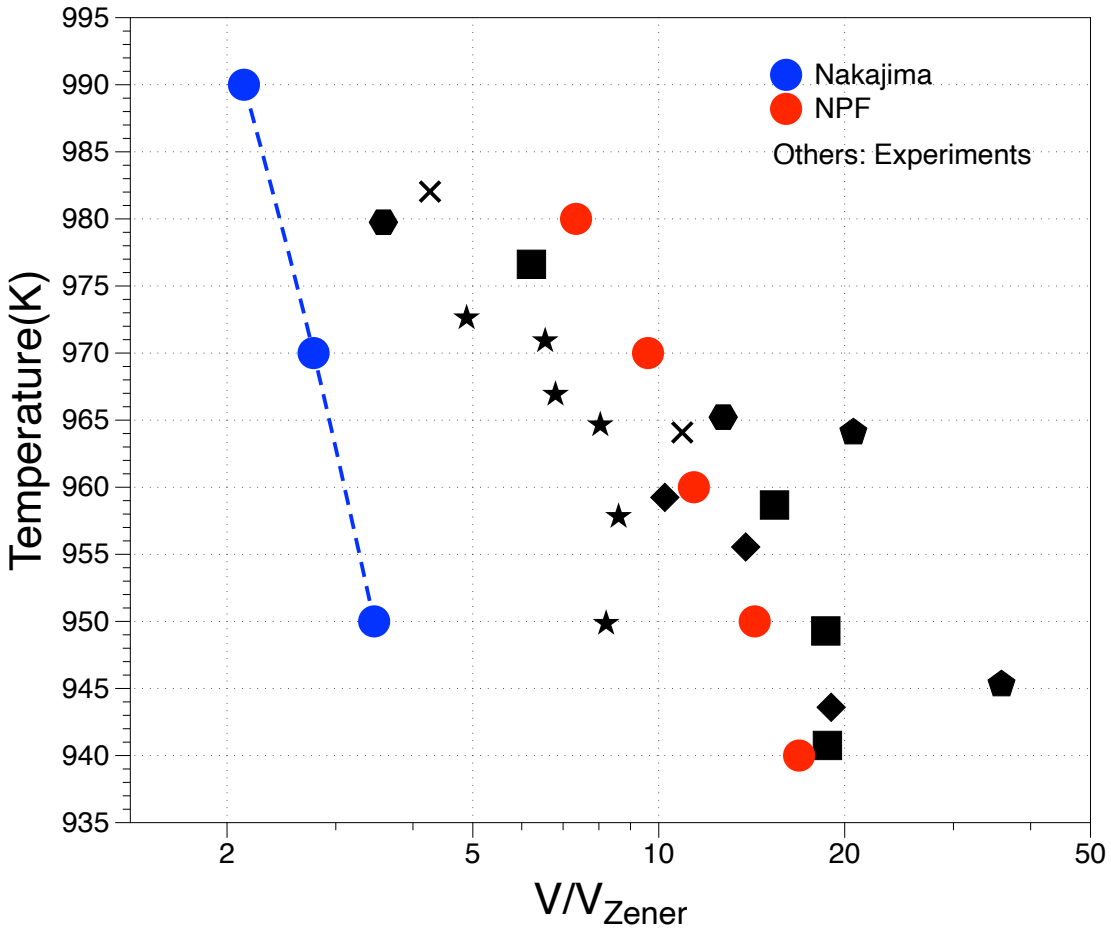

Figure 5.10: The relative growth velocity with diffusion in α, θ phases and along interfaces normalized to the Zener-Hillert predictions. Red points are NPF simulation results. Blue points are PF simulation results taken from Ref. [150]. Other black points are experimental observations and taken from Refs. [181–187].

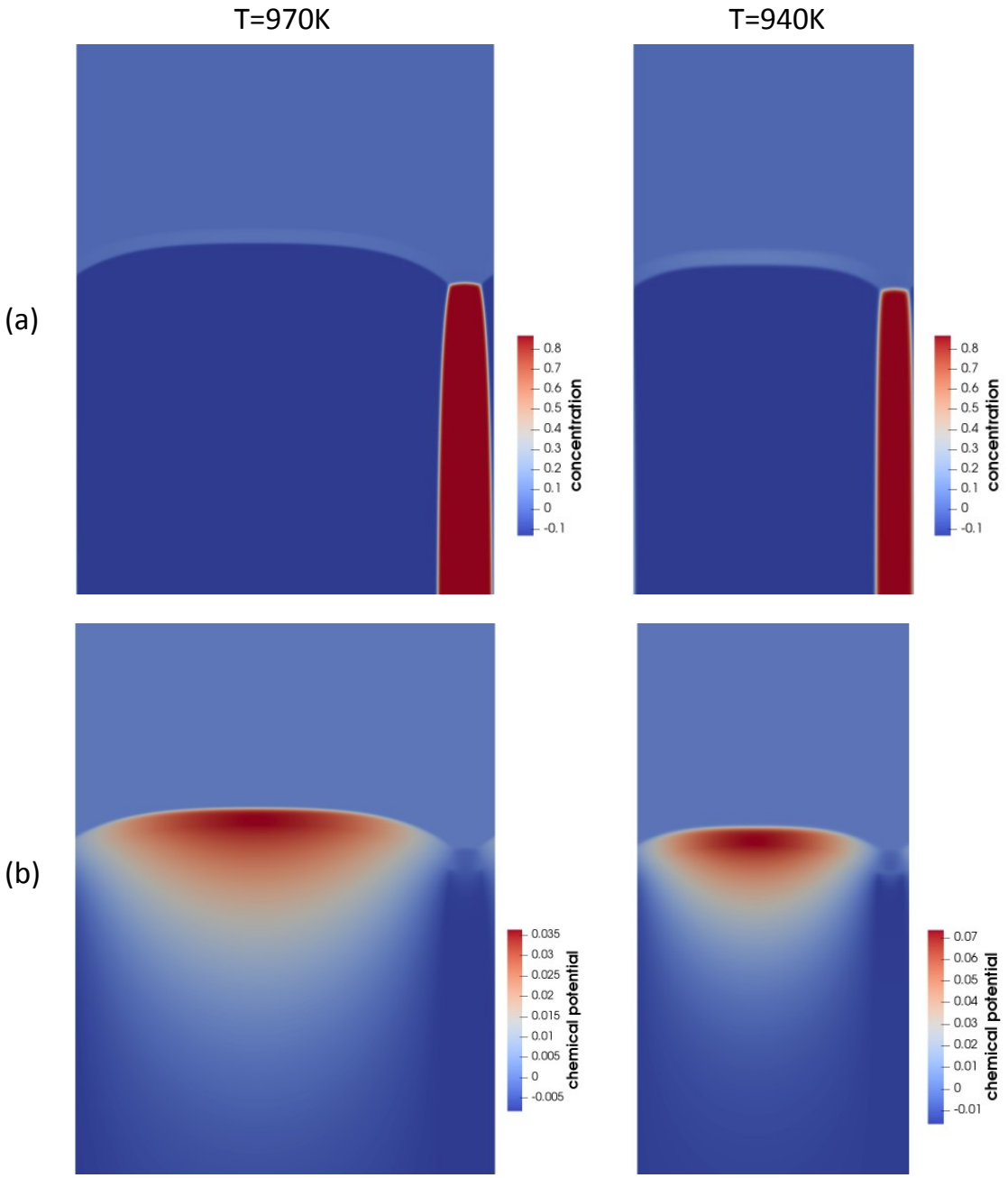

Figure 5.11: Demonstration of NPF simulation results of pearlite growth at steady state when the temperature is 970K and 940K. Figure (a) is the concentration field, while figure (b) is the chemical potential field. The tapering and thickening of cemenite is mitigated when the temperature decreases.

field model are systematically benchmarked for pearlite growth with and without surface diffusion. Based on the advantages of the nondiagonal phase field model, it may be a promising tool for future studies of peritectic solidification, divorced pearlite microstructure formation and pearlite colony formation.

Chapter 6

Summary and conclusions

Due to the artificial enhancement of the interface thickness for typical phase field applications, the elimination of abnormal interface effects and reproduction of the free boundary conditions is a long-standing unsolved problem in the phase field community. Although the thin-interface limit and the anti-trapping current are proposed for quantitative phase field modeling in symmetric and one-sided cases, a thermodynamically consistent solution for the two-sided case has not been elaborated so far. Recently, a nondiagonal phase field model has been developed based on Onsager's reciprocity relations, which introduces a new cross-coupling term to fully remove all the abnormal interface effects in the two-sided case. The aim of this thesis is to solve the persistent problem in the phase field community by developing a nondiagonal phase field model for more general circumstances during phase transformations and metallurgical applications. For this purpose, through reproducing the dendrite growth, eutectic solidification and eutectoid transformations, the capabilities of the developed nondiagonal phase field model are benchmarked and various new insights are gathered.

First, a 4-fold surface energy anisotropy is incorporated in the binary nondiagonal phase field model to investigate the free dendrite growth of pure substances solidification in two-dimensions. In the symmetric and one-sided cases, the dimensionless growth velocities obtained from nondiagonal phase field simulations are benchmarked with Green's function calculations (sharp-interface method). The deviation between simulation results and sharp interface calculations is less than 5%, which is very satisfactory. In the two-sided case, the nondiagonal phase field simulation results demonstrate significant deviations from the Baribieri-Langer theory due to the assumptions of small anisotropy and undercooling (weak out of equilibrium) within this model [124]. In view of our simulation results, a generalization of the prediction is proposed for the two-sided case. The nondiagonal phase field results for small undercooling have a satisfactory agreement with the predictions. Furthermore, the phase field results are also presented when the new cross-coupling term or the elimination of surface diffusion are turned off. These simplifications, which are used in conventional phase field models, lead to significant deviations to the sharp interface results and evidence the necessity of using the nondiagonal phase field model.

The aforementioned nondiagonal phase field model is restricted to two-phase transformations. For the sake of multi-phase transformation, the nondiagonal phase field is extended to three-phase transformations, such as eutectic and eutectoid

transformations, again based on Onsager's principles. The link between the nondiagonal phase field model and free boundary description determines the parameters of the nondiagonal phase field model. The two-dimensional nondiagonal phase field simulations are carried out not only for eutectic solidification in the one-sided case, but also for eutectoid transformation in the two-sided case. The obtained simulation results during eutectic solidification are benchmarked against boundary integral calculations from the literature in the one-sided case. Simulations performed in the two-sided case during eutectoid transformations reveal that the dimensionless growth velocities of lamellae are proportional to the ratio of diffusion coefficients, as described in Ref. [152]. Specifically, when the diffusion coefficients of the growing phases are smaller than the parent phase, the diffusion path in the parent phase is the dominant solute transport path. With the increase of the diffusion coefficients of the growing phases, the transition between parent phase diffusion to growing phases diffusion happens, which leads to modified growth kinetics. Furthermore, in both the one- and two-sided cases, the necessity of using the cross-coupling term in the nondiagonal phase field model is verified for quantitative simulations.

Up to this point, the nondiagonal three-phase field model is derived based on a free energy functional, which is limited to simple symmetric phase diagrams. Therefore, we have developed a grand potential based nondiagonal three-phase field model for complex alloy transformations. The parameters in phase field model are determined with or without surface diffusion through reproducing the proper free boundary conditions. The corresponding two-dimensional phase field simulations are implemented to investigate the growth kinetics of the pearlite transformation with respect to different diffusion paths. When the surface diffusion is eliminated, the simulation results are compared with the Zener-Hillert model in the one-sided case and Ankit's model [152] in the two-sided case. Additionally, when only the diffusion in α and γ phases are considered, the simulation results indicate that the diffusion in cemenite has low influence on the growth kinetic of the pearlite transformation. When the surface diffusion is considered, in the one-sided case, the growth velocities of the lamellae is proportional to the surface diffusion coefficient, which agrees well with the predictions of Pandit's model [147]. Subsequently, we take the diffusion in α, γ phases as well as the surface diffusion into account and reproduce the pearlite growth for different undercoolings. By matching the surface diffusion coefficient in the phase field simulations with experimental data, the nondiagonal phase field simulation results agree well with the experimental observations. Furthermore, the tapering and thickening of cementite phase near the growth front are mitigated at lower temperatures.

This thesis shows the quantitative benefits of the thermodynamically consistent nondiagonal phase field model with the cross-coupling term in symmetric, one- and two-sided cases. Based on the advantages of the nondiagonal phase field model, this quantitative model provides a basis for investigation of various microstructure evolution processes of complex alloys. For instance, this model can be applied not only for two-phase transformations, such as free dendrite growth, dendrite orientation transitions, needle-like dendrite growth in Li polymer, but also for multi-phase transformations, including stable and unstable eutectic solidification, peritectic solidification, monotectic solidification and eutectoid transformation in the solid state. Meanwhile, the limitations of the nondiagonal phase field model should be improved for the applicability of this model. The first one is related to the diffusion ratio con-

trast between growing and parent phases. Secondly, computational techniques, such as adaptive mesh refinement method and multi-GPU acceleration, should be utilized to accelerate large-scale simulations. Finally, more fields, including elastic, flow, magnetic and electric fields, need to be coupled to the nondiagonal phase field model to reproduce the realistic microstructure evolution for various applications in material science. I believe these challenges will be solved in the future.

Appendix A

Asmptotic procedure of thin interface limit

To demonstrate the accurate quantitative solutions of the free boundary conditions in symmetric model, Karma and Rappel analyzed the convergence of the phase field model, which is named "thin-interface limit" [82–84]. In the following, this thin-interface limit is shortly explained.

Firstly, we can write down a simple form of phase field model for pure substance solidification

$$\tau\partial_t\phi = W^2\nabla^\phi - \frac{\partial F(\phi,\lambda u)}{\partial\phi}, \tag{A.1}$$

$$\partial_t u = D\nabla^2 u + \partial_t h(\phi)/2, \tag{A.2}$$

where τ is the relaxation time, W is the interface thickness, $F(\phi,\lambda u)$ includes the double well potential ($f_{dw}(\phi)$) and the chemical free energy ($f_c(\phi)$), i.e., $F(\phi,\lambda u) = f_{dw}(\phi) + \lambda f_c(\phi)u$, with λ being a constant. D is the diffusivity, $h(\phi)$ is the interpolation function, which has two forms

$$h_{VF}(\phi) = 15(\phi - 2\phi^3/3 + \phi^5)/8, \tag{A.3}$$

$$h_{IVF}(\phi) = \phi. \tag{A.4}$$

Then, Eqs. (A.1) and (A.2) can be rewritten in dimensionless form with length unit of l_c and time unit l_c/D, with $l_c \sim D/V_c$ being a mesoscopic length scale,

$$\alpha p^2\partial_t\phi = p^2\nabla^2\phi - f_{dw} - \lambda f_c u, \tag{A.5}$$

$$\partial_t u = \nabla^2 u + \partial_t h/2, \tag{A.6}$$

where $p = W/l_c$, $\alpha = D\tau/W^2$ is the dimensionless diffusivity. For $p \ll 1$, the solutions of Eqs. (A.5) and (A.6) are expanded in powers of p in the inner region,

$$\phi = \phi_0 + p\phi_1 + p^2\phi_2 + \cdots, \tag{A.7}$$

$$u = u_0 + pu_1 + p^2u_2 + \cdots, \tag{A.8}$$

and expanded in the outer region,

$$\tilde{\phi} = \tilde{\phi}_0 + p\tilde{\phi}_1 + p^2\tilde{\phi}_2 + \cdots, \tag{A.9}$$

$$\tilde{u} = \tilde{u}_0 + p\tilde{u}_1 + p^2\tilde{u}_2 + \cdots. \tag{A.10}$$

In the outer region, ϕ is constant in the bulk phase, $\tilde{u}_j$ obeys the diffusion equation

$$\partial_t \tilde{u}_j = \nabla^2 \tilde{u}_j. \tag{A.11}$$

In the inner region, the phase field equations Eqs. (A.5) and (A.6) were rewritten in the curvilinear coordinates (ξ_1, ξ_2, ξ_3), where ξ_1 and ξ_2 measure arclength along the two principal directions of the interface, while ξ_3 measures length along the normal direction. Thus, Eqs. (A.5) and (A.6) become

$$p(\alpha v + \kappa)\partial_\eta \phi + \partial_\eta^2 \phi - \lambda g_\phi u = 0, \tag{A.12}$$

$$p(v + \kappa)\partial_\eta u + \partial_\eta^2 u - pv\partial_\eta h/2 = 0, \tag{A.13}$$

where η is defined as ξ_3/p, $v = Vl_c/D$ is the dimensionless interface velocity and $\kappa = l_c(1/R_1 + R_2)$ is the curvature, where R_1 and R_2 indicate the two principal radii of curvature of the boundary. After substituting Eqs. (A.7) and (A.8) into Eqs. (A.5) and (A.6) without considering the trivial higher order terms in p^2, at the leading order, we obtain

$$\partial_\eta^2 \phi_0 - f_\phi^0 - \lambda g_\phi^0 u_0 = 0, \tag{A.14}$$

$$\partial_\eta^2 u_0 = 0. \tag{A.15}$$

At the first order, it yields

$$\mathcal{L}\phi_1 = \lambda g_\phi^0 u_1 - (\alpha v + \kappa)\partial_\eta \phi_0, \tag{A.16}$$

$$\partial_\eta \left(\partial_\eta u_1 - \frac{v}{2} h^0 \right) = 0, \tag{A.17}$$

with the linear operator $\mathcal{L} = \partial_\eta^2 - f_{\phi\phi}^0$. Integrating Eq. (A.17) once and twice yields

$$-\frac{v}{2} h^0 + \partial_\eta u_1 = A, \tag{A.18}$$

$$u_1 = \bar{u}_1 + A\eta + \frac{v}{2} \int_0^\eta d\eta' h^0, \tag{A.19}$$

where A and $\bar{u}_1$ donate the integration constant. Since the right-hand side of Eq. (A.16) must be orthogonal to $\partial_\eta \phi$ for the existed solution ϕ_1. For $1 \ll \mid \eta \mid \ll p^{-1}$, we have

$$\lim_{\eta \to \pm\infty} \partial_\eta u_1 = \lim_{\xi_3 \to 0^\pm} \partial_{\xi_3} \tilde{u}_0 = \partial_{\xi_3} \tilde{u}_0 |^\pm, \tag{A.20}$$

$$\lim_{\eta \to \pm\infty} h^0(\eta) = \mp 1. \tag{A.21}$$

Inserting Eqs. (A.20) and (A.21) into Eq. (A.18) yields

$$\frac{v}{2} + \partial_{\xi_3} \tilde{u}_0 |^+ = A, \tag{A.22}$$

$$-\frac{v}{2} + \partial_{\xi_3} \tilde{u}_0 |^- = A. \tag{A.23}$$

Elimination of A in Eqs. (A.22) and (A.23) recovers the heat conservation condition

$$v = \partial_{\xi_3} \tilde{u}_0 |^- - \partial_{\xi_3} \tilde{u}_0 |^+. \tag{A.24}$$

To match the regions on both sides of the solid-liquid interface, the outer and inner solutions take the form

$$\tilde{u} = u_i^{\pm} + \partial_{\xi_3}\tilde{u}|^{\pm}\xi_3, \tag{A.25}$$

$$u = p\left(\bar{u}_1 + \frac{v}{2}F^{\pm}\right) + \partial_{\xi_3}\tilde{u}_0|^{\pm}\xi_3, \tag{A.26}$$

where $F^{\pm}$ is defined as

$$F^{\pm} = \int_0^{\pm\infty} d\eta(h^0 \pm 1). \tag{A.27}$$

Equating the right-hand side of Eqs. (A.25) and (A.26) yields

$$u_i^{\pm} = p\left(\bar{u}_1 + \frac{v}{2}F^{\pm}\right). \tag{A.28}$$

Therefore, when g, h are odd functions of ϕ, and f is an even function of ϕ, we obtain the expression of $\bar{u}_1$,

$$\bar{u}_1 = -\frac{I}{\lambda J}(\alpha v + \kappa) + \frac{K}{2J}v, \tag{A.29}$$

with

$$I = \int_{-\infty}^{+\infty} d\eta(\partial_\eta\phi_0)^2, \tag{A.30}$$

$$J = -\int_{-\infty}^{+\infty} d\eta\partial_\eta\phi_0 g_\phi^0, \tag{A.31}$$

$$K = \int_{-\infty}^{+\infty} d\eta\partial_\eta\phi_0 g_\phi^0 \int_0^{\eta} d\eta' h^0. \tag{A.32}$$

Substituting Eq. (A.29) in Eq. (A.28), we get

$$u_i = -\frac{a_1}{\lambda}p\kappa - \frac{a_1\alpha}{\lambda}\left[1 - a_2\frac{\lambda}{\alpha}\right]pv, \tag{A.33}$$

where

$$a_1 = \frac{I}{J}, \tag{A.34}$$

$$a_2 = \frac{K + JF}{2I}. \tag{A.35}$$

Here, Eq. (A.33) is equivalent to the Gibbs-Thomson condition,

$$u_i = -d_0\left(\frac{1}{R_1} + \frac{1}{R_2}\right) - \beta V. \tag{A.36}$$

Appendix B

Nondiagonal phase field model for binary alloys

B.1 Evolution equations

In this appendix, we present the non-diagonal phase field model developed for binary alloys during isothermal solidification in Ref. [108]. Firstly, we introduce the free energy functional in a standard dimensionless form

$$F(c,\phi) = \int \mathrm{d}V \left\{ H \left[\frac{(W\nabla\phi)^2}{2} + f(\phi) \right] + g(C,\phi) \right\}, \tag{B.1}$$

where W is the interface thickness, H determines the height of the potential. $f(\phi)$ and $g(\phi)$ are the double well potential and the chemical free energy density, respectively, which can be written as

$$f(\phi) = \phi^2(1-\phi)^2, \tag{B.2}$$

$$g(C,\phi) = \frac{1}{2}\left[C - C_L^{eq} - q(\phi)(C_S^{eq} - C_L^{eq})\right]^2, \tag{B.3}$$

with

$$q(\phi) = \phi^3(10 - 15\phi + 6\phi^2). \tag{B.4}$$

The chemical potential is

$$\mu = \frac{\partial g(C,\phi)}{\partial C} = C - C_L^{eq} - q(\phi)(C_S^{eq} - C_L^{eq}) \tag{B.5}$$

$\phi(x)$ and $C(x)$ at equilibrium state are

$$\phi_{eq}(x) = \frac{1}{2}\left[1 - \tanh(\frac{x}{\sqrt{2}W})\right]. \tag{B.6}$$

$$C_{eq}(x) = (C_S^{eq} + C_L^{eq})/2 + v(x)(C_S^{eq} - C_L^{eq})/2, \tag{B.7}$$

where $v(x) = 2q[\phi_{eq}(x)] - 1$.

$\dot{\phi}$ presents the amount of matter that undergoes the phase transformation per unit time, which is propotional to the normal velocity of the interface and vanishes in the bulk phases. The dimensionless concentration c is the conserved field and obeys

$$\dot{C} = -\nabla \cdot J, \tag{B.8}$$

with J is the diffusion flux. From the perspective of the Onsager relations, J and $\dot{\phi}$ are linearly related to the driving forces (-$\delta F/\delta\phi$ and $-\nabla\delta F/\delta C$), which are derivatives of the free energy functional with respect to the fields ϕ and C. The driving force conjugated to $\dot{\phi}$ is $-\delta F/\delta\phi$, while the driving force conjugated to J is $-\nabla\delta F/\delta C$. Thus, the non-diagonal phase field model can be written as

$$-\frac{\delta F}{\delta\phi} = \tau(\phi)\dot{\phi} + [M(\phi)W\nabla\phi]\cdot J, \tag{B.9}$$

$$-\nabla\frac{\delta F}{\delta C} = [M(\phi)W\nabla\phi]\dot{\phi} + \frac{J}{D(\phi)}, \tag{B.10}$$

where $\tau(\phi)$ is the relaxation time, $D(\phi)$ is the diffusivity equation and $M(\phi)$ is the parameter of cross-coupling term. The gradient $\nabla\phi$ in the cross-coupling term leads to the influence of the crossing-coupling term in the interface zone. Inserting Eqs. (B.1) and (B.8) into Eqs. (B.9) and (B.10) yields

$$\Delta\dot{\phi} = HW^2\nabla^2\phi - H\frac{\partial f(\phi)}{\partial\phi} - \frac{\partial g(C,\phi)}{\partial\phi} + D(\phi)\nabla\mu \tag{B.11}$$

$$\dot{\mu} = \nabla[D(\phi)\nabla\mu + D(\phi)M(\phi)W\nabla\phi\dot{\phi}] - \frac{\partial q(\phi)}{\partial\phi}(C_S^{eq} - C_L^{eq})\dot{\phi} \tag{B.12}$$

with $\Delta = \tau(\phi) - D(\phi)[M(\phi)W\nabla\phi]^2$. The interface dissipation is

$$\begin{aligned} R &= \frac{1}{2}\int_V \mathrm{d}V\left[-\dot{\phi}\frac{\delta F}{\delta\phi} - J\cdot\nabla\frac{\delta G}{\delta C}\right] \\ &= \frac{1}{2}\int_V \mathrm{d}V\left[\tau(\phi)(\dot{\phi})^2 + \frac{J^2}{D(\phi)} + 2M(\phi)W\dot{\phi}\nabla\phi\cdot J\right]. \end{aligned} \tag{B.13}$$

To ensure the thermodynamic stability of the non-diagonal phase field model, the positiveness of the diagonal term should be satisfied,

$$\tau(\phi), D(\phi) > 0, \Delta > 0. \tag{B.14}$$

Hence, the determinant Δ must be positive, which leads to the positive interface dissipation and the restriction on the cross-coupling term $M(\phi)$, which reads

$$M(\phi) < \frac{\tau(\phi)}{D(\phi)(W\nabla\phi_{eq})^2}. \tag{B.15}$$

B.2 Free boundary descriptions

In the macroscopic description of (slow) solidification, the boundary conditions at the sharp interface without interface kinetics correspond to a local equilibrium. Then the chemical potential difference between the two bulk phases at the interface is determined by the curvature (Gibbs-Thomson correction) alone.

In a binary A-B alloy, the conservation of atoms A and B at a moving interface between parent and growing phases implies the relations

$$-D_S\nabla c|_S\cdot n = VC_S - J_B, \tag{B.16}$$

$$- D_L \nabla c|_L \cdot n = VC_L - J_B, \tag{B.17}$$

where D_S and D_L are the diffusion coefficients in the solid phase and liquid phase. ∇c_S and ∇c_L are the gradients of concentration at the interface on the side of solid and liquid phase. J_B is the flux of atom B through the interface. V represents the total atom flux through the interface, i.e. $V = J_A + J_B$. Similar to J_B, J_A is the normal flux through the interface of atom type A. n is the unit normal vector to the interface.

Moreover, the kinetic boundary conditions linearly relate the grand potential jump ($\delta\Omega$) and chemical potential jump ($\delta\mu$, rigorously the diffusion potential) across the interface to the fluxes V and J_B. At equilibrium, the driving forces of the interface motion are zero, i.e. $\delta\Omega = 0$ and $\delta\mu = 0$. Near equilibrium, $\delta\Omega$ and $\delta\mu$ depend on the free energy density $g_L(C_L)$ and $g_S(C_S)$, the second derivative of free energy density $g''_L(C_L)$ and $g''_S(C_S)$ and the concentrations C_L and C_S in liquid and solid phases, which can be expanded as

$$\delta\Omega = C_S^{eq}(C_S - C_S^{eq})g''_S(C_S^{eq}) - C_L^{eq}(C_L - C_L^{eq})g''_L(C_L^{eq}), \tag{B.18}$$

$$\delta\mu = (C_L - C_L^{eq})g''_L(C_L^{eq}) - (C_S - C_S^{eq})g''_S(C_S^{eq}). \tag{B.19}$$

Consequently, the linear relations can be written as

$$\delta\Omega = \bar{\mathcal{A}}V + \bar{\mathcal{B}}J_B + d_0\kappa, \tag{B.20}$$

$$\delta\mu = \bar{\mathcal{B}}V + \bar{\mathcal{C}}J_B, \tag{B.21}$$

where $\bar{\mathcal{A}}$, $\bar{\mathcal{B}}$ and $\bar{\mathcal{C}}$ are three independent coefficient, which are the components of the 2×2 Onsager matrix. Notice that this matrix is symmetric according to the principles discussed in Section 2.1. In order to ensure the Onsager matrix to be positive, $\bar{\mathcal{A}} > 0$,$\bar{\mathcal{C}} > 0$ and the determinant $\bar{\mathcal{A}}\bar{\mathcal{C}} - \bar{\mathcal{B}}^2 > 0$ should be satisfied simultaneously. Then, the interface dissipation

$$R_{int} = \frac{1}{2}(\delta\Omega \cdot V + \delta\mu \cdot J_B) = \frac{\bar{\mathcal{A}}V^2}{2} + \frac{\bar{\mathcal{C}}J_B^2}{2} + \bar{\mathcal{B}}VJ_B \tag{B.22}$$

is positive for all value of V and J_B.

Subsequently, the procedure to determine the association between the parameters in the non-diagonal phase-field model with the kinetic coefficients $\bar{\mathcal{A}}$, $\bar{\mathcal{B}}$ and $\bar{\mathcal{C}}$ in Onsager matrix is presented. First of all, a one-dimensional infinite system with interface normal coordinate x is considered with the interface being located at $x = 0$. The interface separates the solid ($\phi(-\infty) = 1$) and liquid phase ($\phi(\infty) = 0$).

For a sharp interface, the total dissipation is

$$R_{SI} = \frac{1}{2}\int_{-\infty}^{0} \mathrm{d}x \frac{J^2(x)}{D_S} + \frac{1}{2}\int_{0}^{\infty} \mathrm{d}x \frac{J^2(x)}{D_L} + R_{SI}^{int}, \tag{B.23}$$

where R_{int} indicates the dissipation along the interface. To map the dissipation of the sharp interface method to the non-diagonal phase field method, we compare Eq. (B.23) to the dissipation in the phase field model, Eq. (B.13), which becomes

$$\begin{aligned} R_{NPF} =& \frac{1}{2}\int_{-\infty}^{-\delta} \mathrm{d}x \frac{J^2(x)}{D_S} + \frac{1}{2}\int_{\delta}^{\infty} \mathrm{d}x \frac{J^2(x)}{D_L} \\ &+ \frac{1}{2}\int_{-\delta}^{\delta} \mathrm{d}x \left[\tau(\phi)(\dot{\phi})^2 + \frac{J^2(x)}{D(\phi)} + 2M(\phi)W\dot{\phi}\phi'(x)J(x)\right], \end{aligned} \tag{B.24}$$

where δ indicates the interface thickness of the diffusion interface. When $x < -\delta$, $\phi(x) \approx 1$, while $\phi(x) \approx 0$ for $x > \delta$. The first and second terms in Eq. (B.24) are the dissipation in the bulk phases since $\dot{\phi}$ and $\phi'(x)$ equal to 0 when ϕ is constant. Thus, only the diffusion flux $J(x)$ contributes the dissipation in the bulk phases. Moreover, Eq. (B.24) can also be expressed as

$$\begin{aligned} R_{NPF} =& \frac{1}{2}\int_{-\infty}^{0} \mathrm{d}x \frac{J^2(x)}{D_S} + \frac{1}{2}\int_{0}^{\infty} \mathrm{d}x \frac{J^2(x)}{D_L} - \frac{1}{2}\int_{-\delta}^{0} \mathrm{d}x \frac{J^2(x)}{D_S} - \frac{1}{2}\int_{0}^{\delta} \mathrm{d}x \frac{J^2(x)}{D_L} \\ &+ \frac{1}{2}\int_{-\delta}^{\delta} \mathrm{d}x \left[\tau(\phi)(\dot{\phi})^2 + \frac{J^2(x)}{D(\phi)} + 2M(\phi)W\dot{\phi}\phi'(x)J(x)\right], \end{aligned} \tag{B.25}$$

Through comparing Eq. (B.23) with Eq. (B.25), the interfacial dissipation of the non-diagonal phase field method is

$$\begin{aligned} R_{NPF}^{int} =& \frac{1}{2}\int_{-\delta}^{\delta} \mathrm{d}x \left[\tau(\phi)(\dot{\phi})^2 + \frac{J^2(x)}{D(\phi)} + 2M(\phi)W\dot{\phi}\phi'(x)J(x)\right] \\ &- \frac{1}{2}\int_{-\delta}^{0} \mathrm{d}x \frac{J_S^2}{D_S} - \frac{1}{2}\int_{0}^{\delta} \mathrm{d}x \frac{J_L^2}{D_L}, \end{aligned} \tag{B.26}$$

where J_S and J_L are the fluxes in the bulk phases. In order to identify Eq. (B.26) with Eq. (B.22), $\dot{\phi}$ can be expressed in terms of V at steady state

$$\dot{\phi} = \frac{\partial \phi}{\partial x}\frac{\partial x}{\partial t} \approx -V\phi'(x). \tag{B.27}$$

Moreover, for the quasi-steady concentration field, we have

$$\dot{C} \approx -VC'(x), \tag{B.28}$$

and by the conservation law

$$\dot{C} = -J'(x). \tag{B.29}$$

Thus,

$$J'(x) \approx VC'(x). \tag{B.30}$$

Through integrating Eq. (B.30) with an integration constant $-J_B$, we can obtain

$$J(x) = VC(x) - J_B. \tag{B.31}$$

At the equilibrium state, $\phi(x)$ and $C(x)$ can be replaced by $\phi_{eq}(x)$ and $C_{eq}(x)$, which give the equilibrium distributions of ϕ and C. In addition, we have $J_S = VC_S^{eq} - J_B$

and $J_L = VC_L^{eq} - J_B$ in the bulk phases. Consequently, R_{NPF}^{int} in Eq. (B.26) becomes

$$\begin{aligned}
R_{NPF}^{int} =& \frac{1}{2}\int_{-\delta}^{\delta} \mathrm{d}x\tau(\phi_{eq})[\phi'_{eq}(x)]^2V^2 - \int_{-\delta}^{\delta} \mathrm{d}xM(\phi_{eq})W[\phi'_{eq}(x)]^2V[VC_{eq}(x) - J_B] \\
&+ \frac{1}{2}\int_{-\delta}^{\delta} \mathrm{d}x\left\{\frac{[VC_{eq}(x) - J_B]^2}{D(\phi_{eq})} - \frac{(VC_S^{eq} - J_B)^2}{2D_S} - \frac{(VC_L^{eq} - J_B)^2}{2D_L}\right\} \\
=& \frac{V^2}{2}\int_{-\delta}^{\delta} \mathrm{d}x\left\{\tau(\phi_{eq})[\phi'_{eq}(x)]^2 - 2M(\phi_{eq})W[\phi'_{eq}(x)]^2[C_{eq}(x)]\right. \\
&\left. + \frac{C_{eq}^2(x)}{D(\phi_{eq})} - \frac{(C_S^{eq})^2}{2D_S} - \frac{(C_L^{eq})^2}{2D_L}\right\} \\
&+ VJ_B\int_{-\delta}^{\delta} \mathrm{d}x\left\{M(\phi_{eq})W[\phi'_{eq}(x)]^2 - \left[\frac{C_{eq}(x)}{D(\phi_{eq})} - \frac{C_S^{eq}}{2D_S} - \frac{C_L^{eq}}{2D_L}\right]\right\} \\
&+ \frac{J_B^2}{2}\int_{-\delta}^{\delta} \mathrm{d}x\left[\frac{1}{D(\phi_{eq})} - \frac{1}{2D_S} - \frac{1}{2D_L}\right]
\end{aligned} \tag{B.32}$$

We should note that R_{NPF}^{int} is independent of δ can be extend to $(-\infty, \infty)$ without alteration. Comparing Eq. (B.32) with Eq. (B.22), we can obtain the expression of parameters of Onsager matrix, i.e. $\bar{\mathcal{A}}, \bar{\mathcal{B}}, \bar{\mathcal{C}}$

$$\begin{aligned}
\bar{\mathcal{A}} =& \int_{-\infty}^{\infty} \mathrm{d}x\left\{\tau(\phi_{eq})[\phi'_{eq}(x)]^2\right\} - 2\int_{-\infty}^{\infty} \mathrm{d}xM(\phi_{eq})W[\phi'_{eq}(x)]^2[C_{eq}(x)] \\
&+ \int_{-\infty}^{\infty} \mathrm{d}x\frac{C_{eq}^2(x)}{D(\phi_{eq})} - \frac{(C_S^{eq})^2}{2D_S} - \frac{(C_L^{eq})^2}{2D_L},
\end{aligned} \tag{B.33}$$

$$\bar{\mathcal{B}} = \int_{-\infty}^{\infty} \mathrm{d}x\left\{M(\phi_{eq})W[\phi'_{eq}(x)]^2 - \left[\frac{C_{eq}(x)}{D(\phi_{eq})} - \frac{C_S^{eq}}{2D_S} - \frac{C_L^{eq}}{2D_L}\right]\right\}, \tag{B.34}$$

$$\bar{\mathcal{C}} = \int_{-\infty}^{\infty} \mathrm{d}x\left[\frac{1}{D(\phi_{eq})} - \frac{1}{2D_S} - \frac{1}{2D_L}\right]. \tag{B.35}$$

An alternative way to derive the parameters $\bar{\mathcal{A}}$, $\bar{\mathcal{B}}$ and $\bar{\mathcal{C}}$ is presented in Ref. [107]. The phase field equations are integrated over the interface region to reproduce the equilibrium boundary conditions formed in Eqs. (B.16) and (B.17). On the one hand, through integrating Eq. (B.11) with the combination of Eqs. (B.27), (B.28) and (B.31), the jump of the diffusion chemical potential is

$$\begin{aligned}
\delta\mu =& V\left[MW\int_W \mathrm{d}x[\phi'_{eq}(x)]^2 - \int_W \mathrm{d}xC_{eq}(x)/D(\phi_{eq})\right] \\
&+ J_B\int_W \mathrm{d}x/D(\phi_{eq}).
\end{aligned} \tag{B.36}$$

On the other hand, through multiplying Eq. (B.9) by $\phi'(x)$ and integrating over the interface, we can obtain the grand potential jump

$$\begin{aligned}
\delta\Omega =& V\left\{\tau(\phi_{eq})\int_W \mathrm{d}x[\phi'_{eq}(x)]^2 + \int_W \mathrm{d}xC_{eq}^2(x)/D(\phi_{eq})\right. \\
&\left. -2MW\int_W \mathrm{d}x[\phi'_{eq}(x)]^2C_{eq}(x)\right\} \\
&+ J_B\left\{MW\int_W \mathrm{d}x[\phi'_{eq}(x)]^2 - \int_W C_{eq}(x)/D(\phi_{eq})\right\}.
\end{aligned} \tag{B.37}$$

After identifying Eqs. (B.36) and (B.37) with the Onsager linear relations presented in Eqs. (B.20) and (B.21), the parameters $\bar{\mathcal{A}}$, $\bar{\mathcal{B}}$ and $\bar{\mathcal{C}}$ have the same formulation. Eqs. (B.33) to (B.35) connect the parameters $\bar{\mathcal{A}}$, $\bar{\mathcal{B}}$ and $\bar{\mathcal{C}}$ with the phase field parameters $\tau(\phi)$, $M(\phi)$ and $D(\phi)$. By choosing appropriate phase field parameters, the desired boundary conditions can be reproduced. For instance, during solidification with low undercooling, the free boundary conditions are usually assumed at the solid/liquid interfaces. Thus, the jumps of diffusion chemical potential and grand potential disappear, i.e. $\delta\mu = \delta\Omega = 0$. Under this circumstances, $\bar{\mathcal{A}} = \bar{\mathcal{B}} = \bar{\mathcal{C}} = 0$ has to be satisfied, which leads to diffusion limited interface motion.

B.3 Determination of parameters

In the symmetric case, the diffusivity in the parent phase is equal to one in the growing phase, i.e. $D(\phi) = D_L = D_S = D$. Obviously, $1/D(\phi_{eq}) - 1/2D_S - 1/2D_L = 0$. Since $v(x)$ in Eq. (B.7) is an odd function, $C_{eq}(x)/D(\phi_{eq}) - C_S^{eq}/2D_S - C_L^{eq}/2D_L = 0$. Consequently, The parameters $\bar{\mathcal{A}}$, $\bar{\mathcal{B}}$ and $\bar{\mathcal{C}}$ become

$$\bar{\mathcal{A}} = \frac{\alpha\tau(\phi)}{W} - \frac{\beta W(C_S^{eq} - C_L^{eq})^2}{4D} - \alpha M(\phi)(C_S^{eq} + C_L^{eq}), \tag{B.38}$$

$$\bar{\mathcal{B}} = \alpha M(\phi), \tag{B.39}$$

$$\bar{\mathcal{C}} = 0, \tag{B.40}$$

where

$$\alpha = W\int_{-\infty}^{\infty} \mathrm{d}x[\phi'_{eq}(x)]^2 \approx 0.23570, \tag{B.41}$$

$$\beta = \int_{-\infty}^{\infty} \frac{\mathrm{d}x}{W}[1 - v^2(x)] \approx 1.40748. \tag{B.42}$$

Then, for local equilibrium boundary conditions, $\tau(\phi)$ and $M(\phi)$ are

$$M(\phi) = M = 0, \tag{B.43}$$

$$\tau(\phi) = \tau = \frac{\beta W^2(C_S^{eq} - C_L^{eq})^2}{4\alpha D}. \tag{B.44}$$

For two phase solidification, $\tau(\phi)$ and $M(\phi)$ are constants. In the symmetric case, the cross-coupling term between phase field and diffusion field vanishes, which recovers the results of thin-interface limit analysis.

In the one-sided case for binary alloy during solidification, the diffusivity in solid phase is negligible, i.e. $D_S \ll D_L$. According to Eq. (B.16), we have

$$J_B = VC_S^{eq}. \tag{B.45}$$

Then, the difference of diffusion chemical potential and grand potential in Eqs. (B.20) and (B.21) become

$$\delta\Omega = (\bar{\mathcal{A}} + \bar{\mathcal{B}}C_S^{eq})V + d_0\kappa, \tag{B.46}$$

$$\delta\mu = (\bar{\mathcal{B}} + \bar{\mathcal{C}}C_S^{eq})V. \tag{B.47}$$

Therefore, the elimination of the difference of diffusion chemical potential and grand potential yields

$$\bar{\mathcal{A}} + \bar{\mathcal{B}}C_S^{eq} = 0 \tag{B.48}$$

$$\bar{\mathcal{B}} + \bar{\mathcal{C}} C_S^{eq} = 0 \tag{B.49}$$

The ϕ dependent diffusivity equation in one-sided case is

$$D(\phi) = D_L(1-\phi). \tag{B.50}$$

Here, we should note that $D(\phi=1)=0$, $D(\phi=0)=D_L$ and the surface diffusion, i.e., $D_{surf} = \int_{-\infty}^{\infty}(D(\phi) - D_L/2)\mathrm{d}x$, is automatically eliminated. After substituting Eqs. (B.33) to (B.35) into Eqs. (B.48) and (B.49), we have

$$\bar{\mathcal{B}} + \bar{\mathcal{C}} C_S^{eq} = \alpha M(\phi) - \frac{(C_L^{eq} - C_S^{eq}) W \rho}{2 D_L}, \tag{B.51}$$

$$\bar{\mathcal{A}} + \bar{\mathcal{B}} C_S^{eq} = \frac{\alpha \tau(\phi)}{W} - \frac{(C_L^{eq} - C_S^{eq})^2 W \xi}{4 D_L} - C_L^{eq}(\bar{\mathcal{B}} + \bar{\mathcal{C}} C_S^{eq}), \tag{B.52}$$

where ρ and ξ are constants, which are given by

$$\rho = \int_{-\infty}^{\infty} \frac{\mathrm{d}x}{W} \frac{\phi_{eq}(x) - v(x)}{1-\phi_{eq}(x)} \approx 2.12132, \tag{B.53}$$

$$\xi = \int_{-\infty}^{\infty} \frac{\mathrm{d}x}{W} \frac{1-v^2(x)}{1-\phi_{eq}(x)} \approx 3.42778. \tag{B.54}$$

Consequently, $\tau(\phi)$ and $M(\phi)$ are

$$\tau(\phi) = \tau = \frac{(C_L^{eq} - C_S^{eq})^2 W \xi}{4 \alpha D_L}, \tag{B.55}$$

$$M(\phi) = M = \frac{(C_L^{eq} - C_S^{eq}) W \rho}{2 \alpha D_L}. \tag{B.56}$$

Looking back at Eq. (B.12), the anti-trapping current naturally appears in the flux equation based on the Onsager relations, and reads

$$\begin{aligned} J_{at} &= -D(\phi) M \dot{\phi} \nabla \phi \\ &= -\frac{(C_L^{eq} - C_S^{eq}) W \rho}{2\alpha} (1-\phi) W^2 \dot{\phi} \nabla \phi, \end{aligned} \tag{B.57}$$

which is identical with the anti-trapping current derivated by Karma[85]. Notice, however, that according to the Onsager symmetry, also a new term appears in the phase field equation, which has not been considered in Ref. [85].

Acknowledgments

In the beginning, I would like to thank my PHD supervisor Prof. Dr. Robert Spatschek for his consistent guidance and motivation through these years. He provided lots of supports during my thesis, taught me many things about phase field method, GPU acceleration and gave me many beneficial suggestions about this thesis.

I would like to thank Dr. Efim Brener from Forschungszentrum Jülich and Dr. Guillaume Boussinot from Access e.V., who taught me a lot of theoretical knowledge about Onsager's relations, sharp interface method and phase field models and helped me remarkably to solve the scientific obstacles. I always benefited a lot from the discussions.

I would like to thank Dr. Class Hüter for helping me to solve the Green's function.

I also thank Prof. Dr. Bob Svendsen for accepting to be the second referee of this thesis.

I would also like to thank my group colleagues at IEK-2 who played an important role in the scientific life. Particularly, I would like to thank Xiaoyan Yin, Shuo Fu, Na Ta, Marc Weikamp, Tuan Vo, Manuel Hucko.

Finally, I would like to thank my parents and family for their constant caring, support and encouragement.

Publications

The following publications were created during the doctorate or are in preparation:

- Na Ta, Kai Wang, Xiaoyan Yin, Michael Fleck, Claas Hüter, Elastically induced pattern formation in the initial and frustrated growth regime of bainitic subunits, *AIMS Materials Science* 6.1 (2019): 52-62.
- Kai Wang, Guillaume Boussinot, Claas Hüter, Efim A. Brener, Robert Spatschek, Modeling of dendritic growth using a quantitative nondiagonal phase field model, *Physical Review Materials* 4.3 (2020): 033802.
- Kai Wang, Marc Weikamp, Mingxuan Lin, Carina Zimmermann, Ruth Schwaiger, Ulrich Prahl, Martin Hunkel, Robert Spatschek, Influence of Interface Proximity on Precipitation Thermodynamics, *Metals* 10.10 (2020): 1292.
- Mingxuan Lin, Carina Zimmermann 2, Kai Wang, Martin Hunkel, Ulrich Prahl, Robert Spatschek, Modeling Bainitic Transformations during Press Hardening, *Materials* 14.3 (2021): 654.
- Kai Wang, Guillaume Boussinot, Efim A. Brener, Robert Spatschek, Quantitative nondiagonal phase field modeling of eutectic and eutectoid transformations, *Physical Review B* 103.18 (2021): 184111.
- Kai Wang, Lijun Zhang, Quantitative phase-field simulation of the entire solidification process in one hypereutectic Al–Si alloy considering the effect of latent heat, *Progress in Natural Science: Materials International* (2021).

Bibliography

[1] Lars Onsager. "Reciprocal relations in irreversible processes. I." In: *Physical review* 37.4 (1931), p. 405.

[2] Lars Onsager. "Reciprocal relations in irreversible processes. II." In: *Physical review* 38.12 (1931), p. 2265.

[3] Richard P Wendt. "Simplified transport theory for electrolyte solutions". In: *Journal of Chemical Education* 51.10 (1974), p. 646.

[4] Yasar Demirel. *Nonequilibrium thermodynamics: transport and rate processes in physical, chemical and biological systems*. Elsevier, 2007.

[5] Johannes Diederik van der Waals. "The thermodynamic theory of capillarity under the hypothesis of a continuous variation of density". In: *Journal of Statistical Physics* 20.2 (1979), pp. 200–244.

[6] Long-Qing Chen. "Phase-field models for microstructure evolution". In: *Annual review of materials research* 32.1 (2002), pp. 113–140.

[7] Ingo Steinbach. "Phase-field models in materials science". In: *Modelling and simulation in materials science and engineering* 17.7 (2009), p. 073001.

[8] William J Boettinger et al. "Phase-field simulation of solidification". In: *Annual review of materials research* 32.1 (2002), pp. 163–194.

[9] Nele Moelans, Bart Blanpain, and Patrick Wollants. "An introduction to phase-field modeling of microstructure evolution". In: *Calphad* 32.2 (2008), pp. 268–294.

[10] Nikolas Provatas and Ken Elder. *Phase-field methods in materials science and engineering*. John Wiley & Sons, 2011.

[11] Ingo Steinbach. "Phase-field model for microstructure evolution at the mesoscopic scale". In: *Annual Review of Materials Research* 43 (2013), pp. 89–107.

[12] Vitaly L Ginzburg and Lev D Landau. "On the theory of superconductivity". In: *On Superconductivity and Superfluidity*. Springer, 2009, pp. 113–137.

[13] John W Cahn and John E Hilliard. "Free energy of a nonuniform system. I. Interfacial free energy". In: *The Journal of chemical physics* 28.2 (1958), pp. 258–267.

[14] Pierre C Hohenberg and Bertrand I Halperin. "Theory of dynamic critical phenomena". In: *Reviews of Modern Physics* 49.3 (1977), p. 435.

[15] Long-Qing Chen and AG Khachaturyan. "Computer simulation of structural transformations during precipitation of an ordered intermetallic phase". In: *Acta metallurgica et materialia* 39.11 (1991), pp. 2533–2551.

[16] Y Wang, L-Q Chen, and AG Khachaturyan. "Kinetics of strain-induced morphological transformation in cubic alloys with a miscibility gap". In: *Acta Metallurgica et Materialia* 41.1 (1993), pp. 279–296.

[17] AG Khachaturyan. "Microscopic Theory of Diffusion in Crystalline Solid Solutions and Time Evolution of Diffuse Scattering of X-Rays and Thermal Neutrons". In: *Soviet Physics Solid State, USSR* 9.9 (1968), pp. 2040–+.

[18] Armen G Khachaturyan. *Theory of structural transformations in solids*. Courier Corporation, 2013.

[19] N Zhou et al. "Contributions from elastic inhomogeneity and from plasticity to γ' rafting in single-crystal Ni–Al". In: *Acta Materialia* 56.20 (2008), pp. 6156–6173.

[20] DY Li and LQ Chen. "Shape of a rhombohedral coherent Ti11Ni14 precipitate in a cubic matrix and its growth and dissolution during constrained aging". In: *Acta materialia* 45.6 (1997), pp. 2435–2442.

[21] DY Li and LQ Chen. "Shape evolution and splitting of coherent particles under applied stresses". In: *Acta materialia* 47.1 (1998), pp. 247–257.

[22] Y Wang et al. "Field kinetic model and computer simulation of precipitation of L12 ordered intermetallics from fcc solid solution". In: *Acta materialia* 46.9 (1998), pp. 2983–3001.

[23] JZ Zhu et al. "Three-dimensional phase-field simulations of coarsening kinetics of γ' particles in binary Ni–Al alloys". In: *Acta materialia* 52.9 (2004), pp. 2837–2845.

[24] Tao Wang et al. "Coarsening kinetics of γ' precipitates in the Ni–Al–Mo system". In: *Acta Materialia* 56.19 (2008), pp. 5544–5551.

[25] Bradley S Fromm et al. "Linking phase-field and finite-element modeling for process–structure–property relations of a Ni-base superalloy". In: *Acta materialia* 60.17 (2012), pp. 5984–5999.

[26] YH Wen et al. "A phase-field model for heat treatment applications in Ni-based alloys". In: *Acta materialia* 54.8 (2006), pp. 2087–2099.

[27] VA Vorontsov et al. "Shearing of γ' precipitates by a $< 112 >$ dislocation ribbons in Ni-base superalloys: A phase field approach". In: *Acta Materialia* 58.12 (2010), pp. 4110–4119.

[28] Ning Zhou et al. "Modeling displacive–diffusional coupled dislocation shearing of γ' precipitates in Ni-base superalloys". In: *Acta Materialia* 59.9 (2011), pp. 3484–3497.

[29] N Zhou et al. "Phase field modeling of channel dislocation activity and γ' rafting in single crystal Ni–Al". In: *Acta Materialia* 55.16 (2007), pp. 5369–5381.

[30] Ning Zhou et al. "Large-scale three-dimensional phase field simulation of γ'-rafting and creep deformation". In: *Philosophical Magazine* 90.1-4 (2010), pp. 405–436.

[31] M Cottura et al. "A phase field model incorporating strain gradient viscoplasticity: application to rafting in Ni-base superalloys". In: *Journal of the Mechanics and Physics of Solids* 60.7 (2012), pp. 1243–1256.

[32] M Cottura et al. "Coupling the Phase Field Method for diffusive transformations with dislocation density-based crystal plasticity: Application to Ni-based superalloys". In: *Journal of the Mechanics and Physics of Solids* 94 (2016), pp. 473–489.

[33] Matthieu Degeiter et al. "Instabilities in the periodic arrangement of elastically interacting precipitates in nickel-base superalloys". In: *Acta Materialia* 187 (2020), pp. 41–50.

[34] J Boisse et al. "Phase-field simulation of coarsening of γ precipitates in an ordered γ' matrix". In: *Acta Materialia* 55.18 (2007), pp. 6151–6158.

[35] J Kundin et al. "Phase-field modeling of the γ'-coarsening behavior in Ni-based superalloys". In: *Acta materialia* 60.9 (2012), pp. 3758–3772.

[36] Rongpei Shi and Yunzhi Wang. "Variant selection during α precipitation in Ti–6Al–4V under the influence of local stress–A simulation study". In: *Acta materialia* 61.16 (2013), pp. 6006–6024.

[37] Y Wang and AG Khachaturyan. "Three-dimensional field model and computer modeling of martensitic transformations". In: *Acta materialia* 45.2 (1997), pp. 759–773.

[38] Andrei Artemev, Y Jin, and AG Khachaturyan. "Three-dimensional phase field model of proper martensitic transformation". In: *Acta materialia* 49.7 (2001), pp. 1165–1177.

[39] Yu U Wang, Yongmei M Jin, and Armen G Khachaturyan. "The effects of free surfaces on martensite microstructures: 3D phase field microelasticity simulation study". In: *Acta Materialia* 52.4 (2004), pp. 1039–1050.

[40] Y Gao et al. "P-phase precipitation and its effect on martensitic transformation in (Ni, Pt) Ti shape memory alloys". In: *Acta Materialia* 60.4 (2012), pp. 1514–1527.

[41] YH Wen, Y Wang, and Long-Qing Chen. "Effect of elastic interaction on the formation of a complex multi-domain microstructural pattern during a coherent hexagonal to orthorhombic transformation". In: *Acta materialia* 47.17 (1999), pp. 4375–4386.

[42] Y Gao et al. "Pattern formation during cubic to orthorhombic martensitic transformations in shape memory alloys". In: *Acta materialia* 68 (2014), pp. 93–105.

[43] Yunzhi Wang and Armen G Khachaturyan. "Multi-scale phase field approach to martensitic transformations". In: *Materials Science and Engineering: A* 438 (2006), pp. 55–63.

[44] Pengyang Zhao et al. "Effect of nonlinear and noncollinear transformation strain pathways in phase-field modeling of nucleation and growth during martensite transformation". In: *npj Computational Materials* 3.1 (2017), pp. 1–10.

[45] Oleg Shchyglo, Umut Salman, and Alphonse Finel. "Martensitic phase transformations in Ni–Ti-based shape memory alloys: The Landau theory". In: *Acta Materialia* 60.19 (2012), pp. 6784–6792.

[46] Oleg Shchyglo et al. “Phase-field simulation of martensite microstructure in low-carbon steel”. In: *Acta Materialia* 175 (2019), pp. 415–425.

[47] Hemantha Kumar Yeddu et al. “Three-dimensional phase-field modeling of martensitic microstructure evolution in steels”. In: *Acta Materialia* 60.4 (2012), pp. 1538–1547.

[48] Dong Wang et al. “Phase field simulation of martensitic transformation in pre-strained nanocomposite shape memory alloys”. In: *Acta Materialia* 164 (2019), pp. 99–109.

[49] Mahmood Mamivand et al. “Phase field modeling of the tetragonal-to-monoclinic phase transformation in zirconia”. In: *Acta Materialia* 61.14 (2013), pp. 5223–5235.

[50] Mahmood Mamivand, Mohsen Asle Zaeem, and Haitham El Kadiri. “Phase field modeling of stress-induced tetragonal-to-monoclinic transformation in zirconia and its effect on transformation toughening”. In: *Acta materialia* 64 (2014), pp. 208–219.

[51] Cheikh Cissé and Mohsen Asle Zaeem. “A phase-field model for non-isothermal phase transformation and plasticity in polycrystalline yttria-stabilized tetragonal zirconia”. In: *Acta Materialia* 191 (2020), pp. 111–123.

[52] Long-Qing Chen and Wei Yang. “Computer simulation of the domain dynamics of a quenched system with a large number of nonconserved order parameters: The grain-growth kinetics”. In: *Physical Review B* 50.21 (1994), p. 15752.

[53] Danan Fan and L-Q Chen. “Computer simulation of grain growth using a continuum field model”. In: *Acta Materialia* 45.2 (1997), pp. 611–622.

[54] Danan Fan, Chengwei Geng, and Long-Qing Chen. “Computer simulation of topological evolution in 2-D grain growth using a continuum diffuse-interface field model”. In: *Acta materialia* 45.3 (1997), pp. 1115–1126.

[55] CE Krill Iii and L-Q Chen. “Computer simulation of 3-D grain growth using a phase-field model”. In: *Acta materialia* 50.12 (2002), pp. 3059–3075.

[56] Reza Darvishi Kamachali and Ingo Steinbach. “3-D phase-field simulation of grain growth: topological analysis versus mean-field approximations”. In: *Acta Materialia* 60.6-7 (2012), pp. 2719–2728.

[57] R Darvishi Kamachali et al. “Geometrical grounds of mean field solutions for normal grain growth”. In: *Acta Materialia* 90 (2015), pp. 252–258.

[58] Long-Qing Chen and Danan Fan. “Computer Simulation Model for Coupled Grain Growth and Ostwald Ripening—Application to Al2O3-ZrO2 Two-Phase Systems”. In: *Journal of the American Ceramic Society* 79.5 (1996), pp. 1163–1168.

[59] Danan Fan and Long-Qing Chen. “Diffusion-controlled grain growth in two-phase solids”. In: *Acta materialia* 45.8 (1997), pp. 3297–3310.

[60] Danan Fan et al. “Phase-field simulation of 2-D Ostwald ripening in the high volume fraction regime”. In: *Acta Materialia* 50.8 (2002), pp. 1895–1907.

[61] Stefan Othmar Poulsen, PW Voorhees, and Erik Mejdal Lauridsen. "Three-dimensional simulations of microstructural evolution in polycrystalline dual-phase materials with constant volume fractions". In: *Acta materialia* 61.4 (2013), pp. 1220–1228.

[62] A Kazaryan et al. "Grain growth in anisotropic systems: comparison of effects of energy and mobility". In: *Acta Materialia* 50.10 (2002), pp. 2491–2502.

[63] ShenYang Hu, Chuck H Henager Jr, and LongQing Chen. "Simulations of stress-induced twinning and de-twinning: a phase field model". In: *Acta Materialia* 58.19 (2010), pp. 6554–6564.

[64] Tae Wook Heo et al. "A phase-field model for deformation twinning". In: *Philosophical Magazine Letters* 91.2 (2011), pp. 110–121.

[65] Yijia Gu et al. "Phase field model of deformation twinning in tantalum: Parameterization via molecular dynamics". In: *Scripta Materialia* 68.7 (2013), pp. 451–454.

[66] John D Clayton and Jarek Knap. "A phase field model of deformation twinning: nonlinear theory and numerical simulations". In: *Physica D: Nonlinear Phenomena* 240.9-10 (2011), pp. 841–858.

[67] JD Clayton and J Knap. "Phase field modeling and simulation of coupled fracture and twinning in single crystals and polycrystals". In: *Computer Methods in Applied Mechanics and Engineering* 312 (2016), pp. 447–467.

[68] ZP Pi et al. "A phase field study focuses on the transverse propagation of deformation twinning for hexagonal-closed packed crystals". In: *International Journal of Plasticity* 76 (2016), pp. 130–146.

[69] Long-Qing Chen. "Phase-field method of phase transitions/domain structures in ferroelectric thin films: a review". In: *Journal of the American Ceramic Society* 91.6 (2008), pp. 1835–1844.

[70] YL Li et al. "Phase-field model of domain structures in ferroelectric thin films". In: *Applied Physics Letters* 78.24 (2001), pp. 3878–3880.

[71] D Schrade et al. "Domain evolution in ferroelectric materials: A continuum phase field model and finite element implementation". In: *Computer methods in applied mechanics and engineering* 196.41-44 (2007), pp. 4365–4374.

[72] Jian-Jun Wang, Bo Wang, and Long-Qing Chen. "Understanding, predicting, and designing ferroelectric domain structures and switching guided by the phase-field method". In: *Annual Review of Materials Research* 49 (2019), pp. 127–152.

[73] S Choudhury et al. "Phase-field simulation of polarization switching and domain evolution in ferroelectric polycrystals". In: *Acta materialia* 53.20 (2005), pp. 5313–5321.

[74] Jie Wang et al. "Phase-field simulations of ferroelectric/ferroelastic polarization switching". In: *Acta Materialia* 52.3 (2004), pp. 749–764.

[75] Kaushik Dayal and Kaushik Bhattacharya. "A real-space non-local phase-field model of ferroelectric domain patterns in complex geometries". In: *Acta materialia* 55.6 (2007), pp. 1907–1917.

[76] S Choudhury et al. “Effect of grain orientation and grain size on ferroelectric domain switching and evolution: Phase field simulations”. In: *Acta materialia* 55.4 (2007), pp. 1415–1426.

[77] Atanu K Saha et al. “Phase field modeling of domain dynamics and polarization accumulation in ferroelectric HZO”. In: *Applied Physics Letters* 114.20 (2019), p. 202903.

[78] JX Zhang et al. “Phase-field model for epitaxial ferroelectric and magnetic nanocomposite thin films”. In: *Applied physics letters* 90.5 (2007), p. 052909.

[79] JS Langer. “Models of pattern formation in first-order phase transitions”. In: *Directions in Condensed Matter Physics: Memorial Volume in Honor of Shang-Keng Ma*. World Scientific, 1986, pp. 165–186.

[80] Joseph B Collins and Herbert Levine. “Diffuse interface model of diffusion-limited crystal growth”. In: *Physical Review B* 31.9 (1985), p. 6119.

[81] Ryo Kobayashi. “Modeling and numerical simulations of dendritic crystal growth”. In: *Physica D: Nonlinear Phenomena* 63.3-4 (1993), pp. 410–423.

[82] Alain Karma and Wouter-Jan Rappel. “Phase-field method for computationally efficient modeling of solidification with arbitrary interface kinetics”. In: *Physical review E* 53.4 (1996), R3017.

[83] Alain Karma and Wouter-Jan Rappel. “Numerical simulation of three-dimensional dendritic growth”. In: *Physical Review Letters* 77.19 (1996), p. 4050.

[84] Alain Karma and Wouter-Jan Rappel. “Quantitative phase-field modeling of dendritic growth in two and three dimensions”. In: *Physical review E* 57.4 (1998), p. 4323.

[85] Alain Karma. “Phase-field formulation for quantitative modeling of alloy solidification”. In: *Physical review letters* 87.11 (2001), p. 115701.

[86] R Folch and M Plapp. “Quantitative phase-field modeling of two-phase growth”. In: *Physical Review E* 72.1 (2005), p. 011602.

[87] Munekazu Ohno and Kiyotaka Matsuura. “Quantitative phase-field modeling for dilute alloy solidification involving diffusion in the solid”. In: *Physical Review E* 79.3 (2009), p. 031603.

[88] Munekazu Ohno and Kiyotaka Matsuura. “Quantitative phase-field modeling for two-phase solidification process involving diffusion in the solid”. In: *Acta Materialia* 58.17 (2010), pp. 5749–5758.

[89] Munekazu Ohno and Kiyotaka Matsuura. “Diffusion-controlled peritectic reaction process in carbon steel analyzed by quantitative phase-field simulation”. In: *Acta materialia* 58.18 (2010), pp. 6134–6141.

[90] Ingo Steinbach et al. “A phase field concept for multiphase systems”. In: *Physica D: Nonlinear Phenomena* 94.3 (1996), pp. 135–147.

[91] Janin Tiaden et al. “The multiphase-field model with an integrated concept for modelling solute diffusion”. In: *Physica D: Nonlinear Phenomena* 115.1-2 (1998), pp. 73–86.

[92] Ingo Steinbach and F Pezzolla. “A generalized field method for multiphase transformations using interface fields”. In: *Physica D: Nonlinear Phenomena* 134.4 (1999), pp. 385–393.

[93] Ingo Steinbach et al. "Three-dimensional modeling of equiaxed dendritic growth on a mesoscopic scale". In: *Acta materialia* 47.3 (1999), pp. 971–982.

[94] Ingo Steinbach and Markus Apel. "Multi phase field model for solid state transformation with elastic strain". In: *Physica D: Nonlinear Phenomena* 217.2 (2006), pp. 153–160.

[95] Christoph Beckermann et al. "Modeling melt convection in phase-field simulations of solidification". In: *Journal of Computational Physics* 154.2 (1999), pp. 468–496.

[96] Daniel M Anderson, Geoffrey B McFadden, and Adam A Wheeler. "A phase-field model of solidification with convection". In: *Physica D: Nonlinear Phenomena* 135.1-2 (2000), pp. 175–194.

[97] Vitaliy Pavlyk and Ulrich Dilthey. "Simulation of weld solidification microstructure and its coupling to the macroscopic heat and fluid flow modelling". In: *Modelling and Simulation in Materials Science and Engineering* 12.1 (2003), S33.

[98] G Tegze, T Pusztai, and L Gránásy. "Phase field simulation of liquid phase separation with fluid flow". In: *Materials Science and Engineering: A* 413 (2005), pp. 418–422.

[99] Robert F Almgren. "Second-order phase field asymptotics for unequal conductivities". In: *SIAM Journal on Applied Mathematics* 59.6 (1999), pp. 2086–2107.

[100] Blas Echebarria et al. "Quantitative phase-field model of alloy solidification". In: *Physical review E* 70.6 (2004), p. 061604.

[101] Gerald L Pollack. "Kapitza resistance". In: *Reviews of Modern Physics* 41.1 (1969), p. 48.

[102] Jean-Louis Barrat and François Chiaruttini. "Kapitza resistance at the liquid—solid interface". In: *Molecular Physics* 101.11 (2003), pp. 1605–1610.

[103] Robert Chandler Johnson and WA Little. "Experiments on the Kapitza resistance". In: *Physical review* 130.2 (1963), p. 596.

[104] Mathis Plapp. "Remarks on some open problems in phase-field modelling of solidification". In: *Philosophical Magazine* 91.1 (2011), pp. 25–44.

[105] Mathis Plapp. "Unified derivation of phase-field models for alloy solidification from a grand-potential functional". In: *Physical Review E* 84.3 (2011), p. 031601.

[106] Efim A Brener and DE Temkin. "Onsager approach to the one-dimensional solidification problem and its relation to the phase-field description". In: *Physical Review E* 85.3 (2012), p. 031601.

[107] Efim A Brener and Guillaume Boussinot. "Kinetic cross coupling between nonconserved and conserved fields in phase field models". In: *Physical Review E* 86.6 (2012), p. 060601.

[108] Guillaume Boussinot and Efim A Brener. "Interface kinetics in phase-field models: Isothermal transformations in binary alloys and step dynamics in molecular-beam epitaxy". In: *Physical Review E* 88.2 (2013), p. 022406.

[109] Guillaume Boussinot and Efim A Brener. "Achieving realistic interface kinetics in phase-field models with a diffusional contrast". In: *Physical Review E* 89.6 (2014), p. 060402.

[110] Guillaume Boussinot et al. "Elimination of surface diffusion in the non-diagonal phase field model". In: *Continuum mechanics and thermodynamics* 29.4 (2017), pp. 969–976.

[111] JA Dantzig et al. "Dendritic growth morphologies in Al-Zn alloys—Part II: phase-field computations". In: *Metallurgical and Materials Transactions A* 44.12 (2013), pp. 5532–5543.

[112] William W Mullins and RF Sekerka. "Stability of a planar interface during solidification of a dilute binary alloy". In: *Journal of applied physics* 35.2 (1964), pp. 444–451.

[113] M Ben Amar and Y Pomeau. "Theory of dendritic growth in a weakly undercooled melt". In: *EPL (Europhysics Letters)* 2.4 (1986), p. 307.

[114] MD Kruskal and H Segur. *Asymptotics beyond all orders in a model of dendritic crystals, preprint (1985)*. Tech. rep. ARAP Tech. Memo, 85-25.

[115] Angelo Barbieri, Daniel C Hong, and JS Langer. "Velocity selection in the symmetric model of dendritic crystal growth". In: *Physical Review A* 35.4 (1987), p. 1802.

[116] Boris I Shraiman. "Velocity selection and the Saffman-Taylor problem". In: *Physical review letters* 56.19 (1986), p. 2028.

[117] B Caroli et al. "On velocity selection for needle-crystals in a fully non-local model of solidification". In: *Journal de Physique* 48.4 (1987), pp. 547–552.

[118] Michael N Barber, Angelo Barbieri, and JS Langer. "Dynamics of dendritic sidebranching in the two-dimensional symmetric model of solidification". In: *Physical Review A* 36.7 (1987), p. 3340.

[119] EA Brener and VI Mel'Nikov. "Pattern selection in two-dimensional dendritic growth". In: *Advances in Physics* 40.1 (1991), pp. 53–97.

[120] Y Saito, G Goldbeck-Wood, and H Müller-Krumbhaar. "Dendritic crystallization: Numerical study of the one-sided model". In: *Physical review letters* 58.15 (1987), p. 1541.

[121] Y Saito, G Goldbeck-Wood, and H Müller-Krumbhaar. "Numerical simulation of dendritic growth". In: *Physical Review A* 38.4 (1988), p. 2148.

[122] C Misbah. "Velocity selection for needle crystals in the 2-D one-sided model". In: *Journal de Physique* 48.8 (1987), pp. 1265–1272.

[123] B Caroli et al. "Solvability condition for needle crystals at large undercooling in a nonlocal model of solidification". In: *Physical Review A* 33.1 (1986), p. 442.

[124] A Barbieri and JS Langer. "Predictions of dendritic growth rates in the linearized solvability theory". In: *Physical Review A* 39.10 (1989), p. 5314.

[125] Wilfried Kurz. "Fundamentals of solidification". In: *Trans. Tech. Pub.* 194 (1989).

[126] Clarence Zener. "Kinetics of the decomposition of austenite". In: *Trans. Aime* 167 (1946), pp. 550–595.

[127] WH Brandt. "Solution of the diffusion equation applicable to the edgewise growth of pearlite". In: *Journal of Applied Physics* 16.3 (1945), pp. 139–146.

[128] M Hillert and H Steinhauser. "The structure of white cast iron". In: *Jemont Ann* 144 (1960), pp. 520–559.

[129] KA Jackson and JD Hunt. "Lamellar and rod eutectic growth". In: *Dynamics of Curved Fronts*. Elsevier, 1988, pp. 363–376.

[130] Alain Karma. "Phase-field model of eutectic growth". In: *Physical Review E* 49.3 (1994), p. 2245.

[131] A. A. Wheeler, G. B. McFadden, and W. J. Boettinger. "Phase-field model for solidification of a eutectic alloy". In: *Proceedings of the Royal Society of London. Series A: Mathematical, Physical and Engineering Sciences* 452.1946 (1996), pp. 495–525.

[132] François Drolet et al. "Phase-field modeling of eutectic growth". In: *Physical Review E* 61.6 (2000), p. 6705.

[133] Seong Gyoon Kim et al. "Phase-field modeling of eutectic solidification". In: *Journal of crystal growth* 261.1 (2004), pp. 135–158.

[134] M Apel et al. "2D and 3D phase-field simulations of lamella and fibrous eutectic growth". In: *Journal of crystal growth* 237 (2002), pp. 154–158.

[135] B Nestler and AA Wheeler. "A multi-phase-field model of eutectic and peritectic alloys: numerical simulation of growth structures". In: *Physica D: Nonlinear Phenomena* 138.1-2 (2000), pp. 114–133.

[136] Mathis Plapp and Alain Karma. "Eutectic colony formation: A phase-field study". In: *Physical Review E* 66.6 (2002), p. 061608.

[137] Andrea Parisi and Mathis Plapp. "Stability of lamellar eutectic growth". In: *Acta Materialia* 56.6 (2008), pp. 1348–1357.

[138] Arka Lahiri et al. "Eutectic colony formation in systems with interfacial energy anisotropy: A phase field study". In: *Computational Materials Science* 130 (2017), pp. 109–120.

[139] Johannes Hötzer et al. "Phase-field simulations of spiral growth during directional ternary eutectic solidification". In: *Acta Materialia* 106 (2016), pp. 249–259.

[140] Abhik Choudhury, Mathis Plapp, and Britta Nestler. "Theoretical and numerical study of lamellar eutectic three-phase growth in ternary alloys". In: *Physical Review E* 83.5 (2011), p. 051608.

[141] Math Hillert. "The role of interfacial energy during solid-state phase transformations". In: *Jernkontorets Annaler* 141 (1957), pp. 757–789.

[142] MP Puls and JS Kirkaldy. "The pearlite reaction". In: *Metallurgical and Materials Transactions B* 3.11 (1972), pp. 2777–2796.

[143] D Cheetham and N Ridley. "The kinetics of isothermal and isovelocity pearlite growth in Cu-Al eutectoid alloy". In: *Metallurgical Transactions* 4.11 (1973), pp. 2549–2556.

[144] David Turnbull. "Theory of cellular precipitation". In: *Acta Metallurgica* 3.1 (1955), pp. 55–63.

[145] BE Sundquist. "The edgewise growth of pearlite". In: *Acta metallurgica* 16.12 (1968), pp. 1413–1427.

[146] Mats Hillert. "On theories of growth during discontinuous precipitation". In: *Metallurgical and Materials Transactions B* 3.11 (1972), pp. 2729–2741.

[147] AS Pandit and HKDH Bhadeshia. "Mixed diffusion-controlled growth of pearlite in binary steel". In: *Proceedings of the Royal Society A: Mathematical, Physical and Engineering Sciences* 467.2126 (2011), pp. 508–521.

[148] Akinori Yamanaka et al. "Multi-phase-field study for pearlite transformation with grain boundary diffusion". In: *Proc. 4th Int. Conf. Multiscale Mater. Model.(MMM2008), Florida, USA*. Citeseer. 2008.

[149] Jia-Yi Yan, John Ågren, and Johan Jeppsson. "Pearlite in multicomponent steels: phenomenological steady-state modeling". In: *Metallurgical and Materials Transactions A* 51.5 (2020), pp. 1978–2001.

[150] Katsumi Nakajima, Markus Apel, and Ingo Steinbach. "The role of carbon diffusion in ferrite on the kinetics of cooperative growth of pearlite: A multiphase field study". In: *Acta Materialia* 54.14 (2006), pp. 3665–3672.

[151] I Steinbach and M Apel. "The influence of lattice strain on pearlite formation in Fe–C". In: *Acta Materialia* 55.14 (2007), pp. 4817–4822.

[152] Kumar Ankit et al. "Theoretical and numerical study of lamellar eutectoid growth influenced by volume diffusion". In: *Acta materialia* 61.11 (2013), pp. 4245–4253.

[153] Jason Sanders and Edward Kandrot. *CUDA by example: an introduction to general-purpose GPU programming*. Addison-Wesley Professional, 2010.

[154] Rob Farber. *CUDA application design and development*. Elsevier, 2011.

[155] John Cheng, Max Grossman, and Ty McKercher. *Professional CUDA c programming*. John Wiley & Sons, 2014.

[156] Akinori Yamanaka et al. "GPU-accelerated phase-field simulation of dendritic solidification in a binary alloy". In: *Journal of Crystal Growth* 318.1 (2011), pp. 40–45.

[157] Takayuki Aoki, Satoi Ogawa, and Akinori Yamanaka. "Multiple-GPU scalability of phase-field simulation for dendritic solidification". In: *Progress in Nuclear Science and Technology* 2 (2011), pp. 639–642.

[158] Akinori Yamanaka et al. "Multiphase field simulation of austenite-to-ferrite transformation accelerated by GPU computing". In: *Journal of Computational Science and Technology* 6.3 (2012), pp. 182–197.

[159] Tomohiro Takaki et al. "Unexpected selection of growing dendrites by very-large-scale phase-field simulation". In: *Journal of Crystal Growth* 382 (2013), pp. 21–25.

[160] Alexander Schlüter, Adrian Willenbücher, and Charlotte Kuhn. "GPU-accelerated crack path computation based on a phase field approach for brittle fracture". In: *Proceedings of the 2nd young researcher symposium (YRS)*. 2013, pp. 60–65.

[161] Tomohiro Takaki et al. "Two-dimensional phase-field simulations of dendrite competitive growth during the directional solidification of a binary alloy bicrystal". In: *Acta Materialia* 81 (2014), pp. 272–283.

[162] T Takaki et al. "GPU phase-field lattice Boltzmann simulations of growth and motion of a binary alloy dendrite". In: *IOP Conference Series: Materials Science and Engineering*. Vol. 84. 1. IOP Publishing. 2015, p. 012066.

[163] S Sakane et al. "GPU-accelerated 3D phase-field simulations of dendrite competitive growth during directional solidification of binary alloy". In: *IOP Conference Series: Materials Science and Engineering*. Vol. 84. 1. IOP Publishing. 2015, p. 012063.

[164] Damien Tourret and Alain Karma. "Growth competition of columnar dendritic grains: A phase-field study". In: *Acta Materialia* 82 (2015), pp. 64–83.

[165] Roberto Rojas, Tomohiro Takaki, and Munekazu Ohno. "A phase-field-lattice Boltzmann method for modeling motion and growth of a dendrite for binary alloy solidification in the presence of melt convection". In: *Journal of Computational Physics* 298 (2015), pp. 29–40.

[166] Yasushi Shibuta, Munekazu Ohno, and Tomohiro Takaki. "Solidification in a supercomputer: from crystal nuclei to dendrite assemblages". In: *Jom* 67.8 (2015), pp. 1793–1804.

[167] Kai Wang et al. "Modeling of dendritic growth using a quantitative nondiagonal phase field model". In: *Physical Review Materials* 4.3 (2020), p. 033802.

[168] EA Brener et al. "Velocity selection problem in the presence of the triple junction". In: *Physical review letters* 99.10 (2007), p. 105701.

[169] GP Ivantsov. "Temperature field around a spherical, cylindrical, and needle-shaped crystal, growing in a pre-cooled melt". In: *Temperature field around a spherical* 58 (1985), pp. 567–569.

[170] Munekazu Ohno, Tomohiro Takaki, and Yasushi Shibuta. "Variational formulation and numerical accuracy of a quantitative phase-field model for binary alloy solidification with two-sided diffusion". In: *Physical Review E* 93.1 (2016), p. 012802.

[171] Tatu Pinomaa and Nikolas Provatas. "Quantitative phase field modeling of solute trapping and continuous growth kinetics in quasi-rapid solidification". In: *Acta Materialia* 168 (2019), pp. 167–177.

[172] Hideyuki Yasuda et al. "Dendrite fragmentation induced by massive-like δ–γ transformation in Fe–C alloys". In: *Nature communications* 10.1 (2019), pp. 1–8.

[173] Kai Wang et al. "Quantitative nondiagonal phase field modeling of eutectic and eutectoid transformations". In: *Physical Review B* 103.18 (2021), p. 184111.

[174] Matteo Nicoli, Mathis Plapp, and Hervé Henry. "Tensorial mobilities for accurate solution of transport problems in models with diffuse interfaces". In: *Physical Review E* 84.4 (2011), p. 046707.

[175] Munekazu Ohno, Tomohiro Takaki, and Yasushi Shibuta. "Variational formulation of a quantitative phase-field model for nonisothermal solidification in a multicomponent alloy". In: *Physical Review E* 96.3 (2017), p. 033311.

[176] K Kassner and C Misbah. "Growth of lamellar eutectic structures: the axisymmetric state". In: *Physical Review A* 44.10 (1991), p. 6513.

[177] JD Verhoeven and ED Gibson. "The divorced eutectoid transformation in steel". In: *Metallurgical and Materials Transactions A* 29.4 (1998), pp. 1181–1189.

[178] Kumar Ankit et al. "Deviations from cooperative growth mode during eutectoid transformation: Insights from a phase-field approach". In: *Acta materialia* 81 (2014), pp. 204–210.

[179] Carlos Capdevila, F García Caballero, and C García de Andrés. "Kinetics model of isothermal pearlite formation in a 0.4 C–1.6 Mn steel". In: *Acta materialia* 50.18 (2002), pp. 4629–4641.

[180] LS Darken. "Some observations on the growth of pearlite". In: *Decomposition of austenite by diffusional processes* (1962).

[181] D Brown and N Ridley. "Kinetics of the pearlite reaction in high-purity nickel eutectoid steels". In: *J Iron Steel Inst* 207.9 (1969), pp. 1232–1240.

[182] D Cheetham and N Ridley. "Isovelocity and isothermal pearlite growth in a eutectoid steel". In: *J. Iron Steel Inst.* 211.9 (1973), pp. 648–652.

[183] DD Pearson and JD Verhoeven. "Forced velocity pearlite in high purity Fe-C alloys: Part 1. experimental". In: *Metallurgical and Materials Transactions A* 15.6 (1984), pp. 1037–1045.

[184] FC Hull, RA Colton, and RF Mehl. "Rate of nucleation and rate of growth of pearlite". In: *Trans. AIME* 150.185-207 (1942), pp. 66–68.

[185] JH Frye Jr, EE Stansbury, and DL McElroy. "Absolute rate theory applied to rate of growth of pearlite". In: *Trans. AIME* 197.219-224 (1953), pp. 3–47.

[186] F Togashi and T Nishizawa. "Diffusion and Interface Migration in the Growth of Pearlite". In: *Journal of the Japan Institute of Metals* 40.7 (1976), pp. 691–700.

[187] H Yamaguchi and M Ichimura. "Role of Mn in the Isothermal Pearlite Transformation". In: *J. Japan Inst. Metals* 37.3 (1973), pp. 263–271.